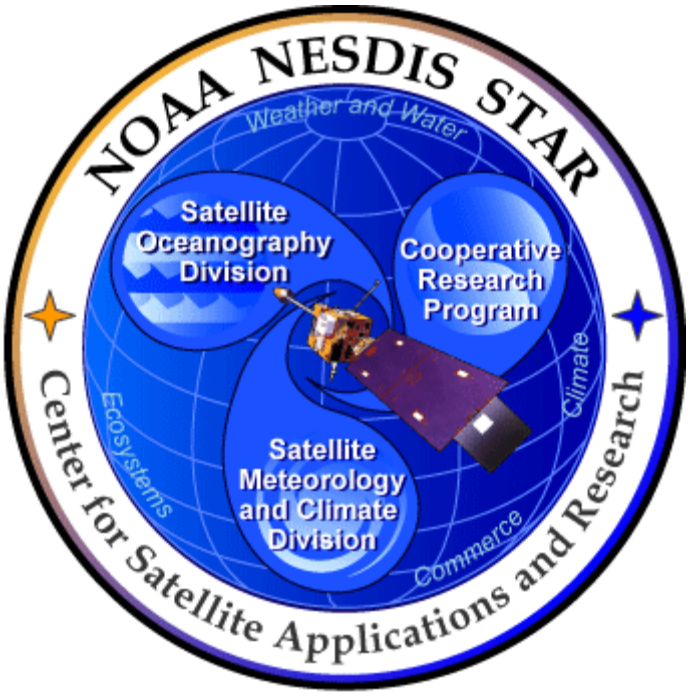

NOAA NESDIS
CENTER for SATELLITE APPLICATIONS and RESEARCH

GOES-R Advanced Baseline Imager (ABI) Algorithm Theoretical Basis Document For Downward Shortwave Radiation (Surface), and Reflected Shortwave Radiation (TOA)

AWG Radiation Budget Application Team

Version 2.0
September 27, 2010

TABLE OF CONTENTS

LIST OF FIGURES

LIST OF TABLES

LIST OF ACRONYMS

ABI	Advanced Baseline Imager
ADM	Angular Distribution Model
ARM	Atmospheric Radiation Measurement project
ASTER	Advanced Space Thermal Emission and Reflection Radiometer
ATBD	Algorithm Theoretical Basis Document
AVHRR	Advanced Very High Resolution Radiometer
AWG	Algorithms Working Group
CAVE	CERES/ARM Validation Experiment
CERES	Clouds and the Earth's Radiant Energy System
CMDL	Climate Monitoring and Diagnostics Laboratory
CONUS	Continental US
DOE	Department of Energy
DSR	Downward Shortwave Radiation at Surface
ESRL/GMD	Earth System Research Laboratory/Global Monitoring Division
EUMETSAT	European Organisation for the Exploitation of Meteorological Satellites
F&PS	Functional and Performance Specification
GSIP	GOES Surface and Insolation Project
GOES	Geostationary Operational Environmental Satellite
GVI	Global Vegetation Index
IGBP	International Geosphere-Biosphere Programme
ISCCP	International Satellite Cloud Climatology Project
JPSS	Joint Polar Satellite System
LaRC	Langley Research Center
LUT	Lookup Table
MODIS	Moderate Resolution Imaging Spectroradiometer
MODTRAN	Moderate Resolution Radiative Transfer Models
MRD	Mission Requirements Document
NASA	National Aeronautics and Space Administration
NCEP	National Centers for Environmental Prediction
NESDIS	National Environmental Satellite, Data, and Information Service
NIR	Near Infrared
NOAA	National Oceanic and Atmospheric Administration
NPOESS	National Polar-orbiting Operational Environmental Satellite System
NTB	Narrow-to-Broadband
OAR	Office of Oceanic and Atmospheric Research
PAR	Photosynthetically Active Radiation
RAZ	Relative Azimuth Angle
PSGS	Perot Systems Government Services
RSR	Reflected Shortwave Radiation at TOA
RTM	Radiative Transfer Model
SARB	Surface and Atmospheric Radiation Budget
SEBN	Surface Energy Balance Network

SEVIRI	Spinning Enhanced Visible and Infra-red Imager
SRB	Shortwave Radiation Budget
STAR	Center for Satellite Applications and Research
SURFRAD	Surface Radiation Budget Network
SW	Shortwave
SZA	Solar Zenith Angle
TIGR	TIROS Initial Guess Retrieval
TOA	Top of Atmosphere
TOMS	Total Ozone Mapping Spectrometer
TPW	Total Pecipitable Water
UMD	University of Maryland
USGS	United States Geological Survey
VZA	Local Zenith Angle
WCRP	World Climate Research Program

ABSTRACT

This document describes the physical and mathematical basis of the algorithm developed for retrieving downward shortwave radiation at the surface and reflected shortwave radiation at the top of the atmosphere from the reflectance measurements of, and atmosphere and surface products derived from the Advanced Baseline Imager onboard the geostationary satellite GOES-R. When data needed to describe the composition of the atmosphere and the reflective properties of the surface are available from preceding ABI retrievals and/or ancillary sources the algorithm retrieves the radiative fluxes in a forward scheme using a look-up-table representation of the radiative transfer. When the needed ABI products are not available the algorithm estimates the fluxes from the broadband top-of-atmosphere albedo derived from narrowband ABI reflectances by appropriate spectral and angular transformations.

The algorithm is tested with proxy data from MODIS and SEVIRI. Performance is evaluated by comparison with ground measurements of downward shortwave radiation at the surface from the SURFRAD and BSRN networks, and with observations of the reflected shortwave radiation at the top of the atmosphere from CERES and GERB. The accuracy and precision is found to be a function of the measured quantity. Overall, the fluxes are estimated by an accuracy of better than about 2% for the downward shortwave radiation at surface (DSR) and 7% for the reflected shortwave radiation at TOA (RSR). Precision of retrieved shortwave fluxes is better than 25%. Quality of the retrieval is indicated by flags that are set according to the quality of input, retrieval conditions, and expected range of output.

Validations in the pre-launch and post-launch phases use similar methods and tools with MODIS, and SEVIRI as proxy data and CERES, GERB, SURFRAD, BSRN and the future SEBN as sources of reference data.

1. INTRODUCTION

Solar radiation provides the energy that drives the Earth's weather and climate. Approximately two thirds of the solar radiant energy incident on the Earth is absorbed, heating the Earth's surface until it radiates nearly as much energy back to space as it absorbs from the sun. The remaining one third of the incident solar energy is reflected back into space. Both the absorbed and reflected solar radiation are in the shortwave part of the electromagnetic spectrum, while the Earth's radiation emitted back to space is longwave or thermal infrared radiation. The balance between the solar input and the thermal output is known as the Earth's Radiation Budget. This radiation budget is affected by the nature of the Earth's surface and its atmosphere, particularly clouds.

The Earth's radiation budget has been estimated from satellite measurements since the beginning of satellite observations. At the top of atmosphere (TOA) it has usually been derived using measurements collected from operational satellites by applying spectral and angular transformations needed to go from narrowband reflectances measured by these satellites to the broadband fluxes needed in weather and climate applications. These transformations are, in most cases, valid only in a statistical sense; hence, the broadband fluxes derived by them usually do not meet the accuracy requirements needed for climate. More accurate measurements of the Earth's radiation budget are obtained from the broadband sensors flown on specific Earth's radiation budget missions, such as the Earth Radiation Budget Experiment (ERBE; Barkstrom, 1984), the Scanner for Radiation Budget (ScaRaB; Morel et al., 1993; Kandel et al., 1993), the Clouds and the Earth's Radiant Energy System (CERES; Wielicki et al., 1996), and the Geostationary Earth Radiation Budget (GERB; Harries et al., 2005).

In addition to measuring the TOA radiation budget, there is also a need to estimate radiative fluxes at the surface. In the last three decades, a number of algorithms were proposed for this (e.g., Tarpley, 1979; Gautier et al., 1980; Dedieu et al., 1987; Darnell et al., 1988; Pinker and Laszlo, 1992; Frouin and Chertock, 1992; Rossow and Zhang, 1995, Zhang et al., 2004). It has been demonstrated that using some of these algorithms surface fluxes could be derived from satellite observations with reasonable accuracy (e.g., Pinker et al., 1995; Whitlock et al., 1995). Some of the algorithms have been applied to satellite data to generate long-term climatology of radiation. For example, the Surface Radiation Budget (SRB) project at NASA (Whitlock et al., 1995; Stackhouse et al., 2004, Cox et al., 2006, Gupta et al., 2006; Hinkelman et al., 2009) estimates surface radiative fluxes from the International Satellite Cloud Climatology Project (ISCCP) (Rossow and Schiffer, 1999) DX radiance and cloud parameters using an updated version of the University of Maryland flux algorithm (Pinker and Laszlo, 1992).

Observations of geostationary satellites are also used for characterizing the solar (shortwave) energy balance of our planet and the solar irradiance reaching the surface. Many approaches were developed for using data from instruments onboard the US Geostationary Operational Environmental Satellite (GOES) series. By empirically relating satellite-measured brightness and cloud amount to hourly pyranometer insolation measurements, Tarpley (1979) demonstrated that insolation can be determined from the

Visible and Infrared Spin Scan Radiometer (VISSR) on GOES. Gautier et al. (1980) and Diak and Gautier (1983) developed a physical model that accounted for molecular scattering and cloud extinction, and applied it to estimate insolation from GOES radiances. Gu and Smith (1997) modified the Gauthier et al. (1980) algorithm for the Boreal Ecosystem. Pinker and Laszlo (1992) designed another physical method that in addition to gas absorption accounted for both aerosol and cloud extinction. Regional and global applicability of their model was demonstrated with GOES-5 VISSR data and with geostationary radiances from the International Satellite Cloud Climatology Project (ISCCP, Schiffer and Rossow, 1983) B3 data. The same algorithm was adopted by NOAA/NESDIS in the GOES Surface and Insolation Product (GSIP, Pinker et al., 2002). Dubayah et al. (1997) constructed an algorithm that combines solar radiation fields derived from GOES observations with digital elevation data to produce topographically varying insolation fields. Ceballos et al. (2004) developed a simple method for retrieving surface insolation over Brazil from GOES 8 data. Methods for estimating surface solar radiation from European and Japanese geostationary satellites were also developed. For example, Nunez et al. (1993) and Weymouth and Le Marshall (1999) designed models to estimate global solar radiation from visible Geostationary Meteorological Satellite (GMS) data. Moser and Raschke (1984) developed the IGKM model to be used with METOSAT data. This model was later improved by Stuhlmann et al. (1990). Reviews of various techniques and their performances are provided by Schmetz (1989) and Pinker et al., (1995). They report daily insolation estimates that are generally within 10%–15% of pyranometer data, and hourly estimates that have errors ranging from 5%–10% for clear-sky conditions to 15%–30% for all-sky conditions.

1.1 Purpose of This Document

This Algorithm Theoretical Basis Document (ATBD) provides a description of the physical basis and the algorithm for the retrieval of downward shortwave (SW: 0.2-4.0 μm) radiation at the surface (DSR) and the reflected SW radiation (RSR) at the top of atmosphere (TOA) from reflectances measured by the Advanced Baseline Imager (ABI) flown on the GOES-R series of NOAA geostationary meteorological satellites. Essentially, it describes a hybrid algorithm which combines the NASA forward algorithm (direct path) and the STAR/UMD inversion algorithm (indirect path). Also described is the conversion of narrowband reflectances into broadband albedos (NTB) needed by the indirect path. The document also provides details on the evaluation of algorithm performance during the development phase.

1.2 Who Should Use This Document

The intended users of this document are those interested in understanding the physical basis of the SW radiation budget algorithm and how to use the output of this algorithm in applications requiring estimates of SW fluxes. This document also provides information useful to anyone maintaining or modifying the original algorithm.

1.3 Inside Each Section

This document is broken down into the following main sections.

- **System Overview**: Provides relevant details of the ABI and provides a brief description of the products generated by the algorithm.

- **Algorithm Description**: Provides all the detailed description of the algorithm including its physical basis, its input and its output.

- **Test Data Sets and Output**: Provides a description of the test data set used to characterize the performance of the algorithm and quality of the data products. It also describes the results from algorithm processing using simulated input data.

- **Practical Considerations**: Provides an overview of the issues involving numerical computation, programming and procedures, quality assessment and diagnostics and exception handling.

- **Assumptions and Limitations**: Provides an overview of the current limitations of the approach and gives the plan for overcoming these limitations with further algorithm development.

1.4 Related Documents

This document relates to the references given throughout and to the following documents:

GOES-R Mission Requirements Document (MRD)
GOES-R Ground Segment Functional and Performance Specification Document (F&PS)
GOSE-R ABI *Downward Shortwave Radiation: Surface and Reflected Shortwave Radiation: TOA* Algorithm and Test Implementation Plan (ATIP) Document
GOSE-R ABI *Downward Shortwave Radiation: Surface and Reflected Shortwave Radiation: TOA* Product Validation Plan Document

1.5 Revision History

This is Version 2.0 of this document. The revision evaluates the algorithm to meet the 100% requirements and follows the comments on Version 1.0 from the ADEB and IV&V reviewers. It was written primarily by Dr. Istvan Laszlo (NOAA/STAR) and Dr. Hongqing Liu (PSGS/QSS) with significant inputs from Prof. Rachel T. Pinker, Ms. Xiaolei Niu, and Dr. Margaret Wonsick (all UMD/AOSC), who revised the section on the narrow-to-broadband and angular conversions.

Version 1.0 of this document was written for 80% maturity delivery. That revision evaluated the algorithm to meet the 80% requirements and followed the comments on the draft version (Version 0.1) from the project office. It was a revised and updated version of the Version 0.0 document. It was written primarily by members of the GOES-R AWG Radiation Budget Application Team (AT). Specifically, the description of the NASA algorithm was provided by Mr. Fred G. Rose of SSAI/NASA Langley Research Center (LaRC), and Drs. Thomas Charlock and Patrick Minnis of NASA LaRC. The description of the narrow-to-broadband transformation and angular distribution models were written by Dr. Rachel T. Pinker and Ms. Xiaolei Niu of the University of Maryland (UMD), Department of Atmospheric and Oceanic Science. The description on the STAR/UMD algorithm was provided by Dr. Istvan Laszlo of NESDIS/STAR and Dr. Hongqing Liu of PSGS/QSS. Description of the ground data used in the evaluation of the algorithm was provided by Dr. Ellsworth G. Dutton of NOAA/OAR. Version 0.0 was delivered on August 17, 2008 to accompany the delivery of version 1 of the algorithm to the GOES-R AWG Algorithm Integration Team (AIT).

2 OBSERVING SYSTEM OVERVIEW

This section provides an overview of the retrieval strategy, the algorithm, the input needed. It also describes the products generated by the ABI SW radiation budget (SRB) algorithm and the requirements it places on the sensor.

2.1 Products Generated

The ABI SRB algorithm generates the Downward Shortwave Radiation at Surface (DSR) and Reflected Shortwave Radiation at TOA (RSR) products.

DSR is the total shortwave irradiance (flux) received by a horizontal unit area at the surface of the Earth. It includes both direct and diffuse radiation. The direct component results from the transmission of the direct solar beam radiation incident at the top of the atmosphere to the surface. During its path from TOA to the surface the direct beam is attenuated by scattering and absorption processes as it interacts with the atmosphere. The diffuse component is made up of the radiation that is scattered out of the direct beam and after multiple scattering events and absorption reaches the surface. It also includes radiation that is reflected upward at the surface and subsequently reflected back to the surface by the atmosphere.

DSR has many applications both in the general and applied sciences. Being one of the components of the surface energy budget it is needed in climate studies. Used together with cloud and aerosol properties it provides estimates of cloud and aerosol effects (forcing). It is also used in surface energy budget models (land surface assimilation models such as those used at NOAA NCEP, NASA LDAS, and ocean assimilation

models) either as an input (providing observationally-based forcing term), or as an independent source of evaluation. DSR data are also employed in estimating heat flux components over the coastal ocean to drive ocean circulation models. The GOES-R based DSR due to its resolution of the diurnal cycle can be complementary to other DSR algorithms that estimate DSR at low temporal resolution (for example, CERES; Wielicki et al., 1996). In agriculture DSR is used as input in crop modeling. In hydrology, it is used in watershed and run-off analysis, which is important for determining flood risks, dam monitoring. Solar energy industry also needs estimates of DSR, both real-time and short-term forecasts for building energy usage modeling and optimization. Since high irradiance values result in surface drying DSR is also used in monitoring fire risk.

RSR is the shortwave flux exiting from a unit area at the top of the atmosphere. It is a result of scattering and absorption of the solar beam and of the radiation reflected upward by the surface. RSR (together with the upward longwave radiation at TOA) is used in studies of the planetary energy budget. It can also be a source of independent data for the evaluation of NWP models. The GOES-R based diurnally-resolved RSR will also be complementary to other estimates of RSR made from polar platforms.

Both DSR and RSR are given in the units of W/m^2.

Tables 2-1, 2-2, 2-3, and 2-4 show the current requirements and product qualifiers for these two products.

Table 2-1. Requirements for Downward Shortwave Radiation at surface (DSR). C=CONUS, FD=full disk, M=mesoscale.

Name	User & Priority	Geographic Coverage	Vertical Resolution	Horizontal Resolution	Mapping Accuracy	Measurement Range	Measurement Accuracy	Refresh Rate/Coverage	Refresh Rate Option (Mode 4)	Vendor Allocated	Product Measurement Precision
Downward Solar Insolation: surface	GOES-R	C	N/A	25 km	2 km	0 – 1500 W/m2	85 W/m^2 in high end of range (>500 W/m^2); 65 W/m^2 in typical value range (200-500 W/m^2); 110 W/m^2 at low end of range (<200 W/m^2)	60 min	60 min	3236 sec	100 W/m^2 for low and high range (<200 and >500 W/m^2) and 130 W/m^2 for mid range (200-500 W/m^2)
Downward Solar Insolation: surface	GOES-R	FD	N/A	50 km	4 km	0 – 1500 W/m2	85 W/m^2 in high end of range (>500 W/m^2); 65 W/m^2 in typical value range (200-500 W/m^2); 110 W/m^2 at low end of range (<200 W/m^2)	60 min	60 min	3236 sec	100 W/m^2 for low and high range (<200 and >500 W/m^2) and 130 W/m^2 for mid range (200-500 W/m^2)

Downward Solar Insolation: surface	GOES-R	M	N/A	5 km	1 km	0 – 1500 W/m2	85 W/m^2 in high end of range (>500 W/m^2); 65 W/m^2 in typical value range (200-500 W/m^2); 110 W/m^2 at low end of range (<200 W/m^2)	60 min	60 min	3236 sec	100 W/m^2 for low and high range (<200 and >500 W/m^2) and 130 W/m^2 for mid range (200-500 W/m^2)

Table 2-2. Product qualifiers for Downward Shortwave Radiation at surface (DSR). SZA= solar zenith angle, LZA=local zenith angle.

Name	User & Priority	Geographic Coverage (G, H, C, M)	Temporal Coverage Qualifiers	Product Extent Qualifier	Cloud Cover Conditions Qualifier	Product Statistics Qualifier
Downward Solar Insolation: surface	GOES-R	C	Day for SZA values greater than 25 degrees	Quantitative out to at least 70 degrees LZA and qualitative at larger LZA	N/A	Over specified geographic area
Downward Solar Insolation: surface	GOES-R	FD	Day for SZA values greater than 25 degrees	Quantitative out to at least 70 degrees LZA and qualitative at larger LZA	N/A	Over specified geographic area
Downward Solar Insolation: surface	GOES-R	M	Day for SZA values greater than 25 degrees	Quantitative out to at least 70 degrees LZA and qualitative at larger LZA	N/A	Over specified geographic area

Table 2-3. Requirements for Reflected Shortwave Radiation at top of atmosphere (RSR). C=CONUS, FD=full disk, M=mesoscale.

Name	User & Priority	Geographic Coverage	Vertical Resolution	Horizontal Resolution	Mapping Accuracy	Measurement Range	Measurement Accuracy	Refresh Rate/Coverage	Refresh Rate Option (Mode 4)	Vendor Allocated Ground Latency	Product Measurement Precision
Reflected Solar Insolation: TOA	GOES-R	C, FD	N/A	25 km	2 km	0 – 1300 W/m2	85 W/m^2 in high end of range (>500 W/m^2); 65 W/m^2 in typical value range (200-500 W/m^2); 110 W/m^2 at low end of range (<200 W/m^2)	60 min	5 min	3236 sec	100 W/m^2 for low and high range (<200 and >500 W/m^2) and 130 W/m^2 for mid range (200-500 W/m^2)

Table 2-4. Product qualifiers for Reflected Shortwave Radiation at top of atmosphere (RSR). SZA= solar zenith angle, LZA=local zenith angle.

Name	User & Priority	Geographic Coverage (G, H, C, M)	Temporal Coverage Qualifiers	Product Extent Qualifier	Cloud Cover Conditions Qualifier	Product Statistics Qualifier
Reflected Solar Insolation: TOA	GOES-R	C	Day	Quantitative out to at least 70 degrees LZA and qualitative at larger LZA	Clear conditions associated with threshold accuracy	Over specified geographic area
Reflected Solar Insolation: TOA	GOES-R	FD	Day	Quantitative out to at least 70 degrees LZA and qualitative at larger LZA	Clear conditions associated with threshold accuracy	Over specified geographic area

Due to the wide range of applications the accuracy requirements for DSR differ. Unfortunately, much of the information on current requirements is not readily available, and in some cases the requirements are not specified quantitatively, e.g., coral reef watch asks "do the best you can". Moreover, requirements for a given application can change with time as the method used by that application evolves. The requirements listed in the tables above (likely) represent the need of the NOAA Weather Service.

2.2 Instrument Characteristics

The Advanced Baseline Imager (ABI) on GOES-R will have a total of 16 spectral bands in the visible, near-infrared and infrared spectral regions. The ABI spatial resolution will be 2.0 km for the 1.38-μm, 2.25-μm and ten infrared (IR) spectral bands, and 0.5 km for the 0.64-μm visible band. Spatial resolution of the other bands will be 1.0 km. Table 2-5 lists these and the spectral characteristics of the instrument. ABI will have an on-board calibration of the reflected solar channels and expected to provide an absolute radiometric calibration accuracy of 5.0%, relative (one-sigma) calibration deviations (short-term repeatability) of 0.2%, calibrated radiances that correct for instrument degradation drift in radiance to 0.5% of the radiance. (Additional observations of lunar or stellar sources may be employed by NOAA operationally to attempt to improve long-term radiometric stability of the on-board calibration methodology over the ABI lifetime.) Details on the instrument design, calibration, and additional information on its characteristics are provided elsewhere, and not included in this ATBD. Table 2-5 also indicates which channels are currently used by the algorithm.

The SRB algorithm will use observations in selected channels (see Table 2-5). The selected channel observations are used to estimate RSR, but only when the ABI products needed (aerosol, cloud, surface albedo, etc.) are not available. The performance of the algorithm is therefore sensitive to any imagery artifacts or instrument noise.

Table 2-5 Channel numbers and wavelengths of ABI

Channel ID	***Wavelength Microns***	***Hor. Res.***	***Upper and lower 50% response points (in microns)***	***Noise @ Ref.***	***Max. Level***	***Used in SRB***
1	0.47	1km	0.45±0.01 - 0.49±0.01	300/1	100 %	✓
2	0.64	0.5km	0.59±0.01 - 0.69±0.01	300/1	100 %	✓
3	0.865	1km	0.8455±0.01 - 0.8845±0.01	300/1	100 %	✓
4	1.378	2km	1.3705±0.005 - 1.3855±0.005	300/1	100 %	✓
5	1.61	1km	1.58±0.01 - 1.64±0.01	300/1	100 %	✓
6	2.25	2km	2.225±0.01 - 2.275±0.01	300/1	100 %	✓
7	3.90	2km	3.80±0.05 - 4.00±0.05	0.1 K	400 K	
8	6.185	2km	5.77±0.03 - 6.6±0.03	0.1 K	300 K	
9	6.95	2km	6.75±0.03 - 7.15±0.03	0.1 K	300 K	
10	7.34	2km	7.24±0.02 - 7.44±0.02	0.1 K	320 K	
11	8.5	2km	8.3±0.03 - 8.7±0.03	0.1 K	330 K	
12	9.61	2km	9.42±0.02 - 9.8±0.03	0.1 K	300 K	
13	10.35	2km	10.1±0.1 - 10.6±0.1	0.1 K	330 K	
14	11.2	2km	10.8±0.1 - 11.6±0.1	0.1 K	330 K	
15	12.3	2km	11.8±0.1 - 12.8±0.1	0.1 K	330 K	
16	13.3	2km	13.0±0.06 - 13.6±0.06	0.3 K	305 K	

3 ALGORITHM DESCRIPTION

This section describes the ABI SRB algorithm at the current level of maturity.

3.1 Algorithm Overview

The ABI SRB algorithm is developed as a hybrid algorithm based on the NASA Clouds and the Earth's Radiant Energy System (CERES)/Surface and Atmospheric Radiation Budget (SARB) algorithm (Charlock and Alberta, 1996) and on the UMD SRB algorithm (Pinker and Laszlo, 1992). The primary algorithm is the NASA algorithm, which mostly uses ABI products (e.g., surface albedo; cloud optical depth, particle size, and top height; and aerosol optical depth and single scattering albedo) to estimate the SW fluxes in a forward calculation, hence dubbed as the "direct path". When these ABI products used as inputs are not available the algorithm switches to an appropriately modified version of the UMD algorithm developed at NOAA/NESDIS/STAR to perform the SW flux retrieval. The latter algorithm, being an inversion scheme in nature, termed as the "indirect path". This path requires the ABI observed channel reflectance as major inputs with minimum reliance on the derived Level 2 ABI products. It uses SW broadband TOA albedo estimated from the spectral NTB transformation and angular correction to estimate atmospheric transmittance. Even though they estimate the fluxes in different schemes, both paths use the same lookup table to accomplish the flux retrieval.

3.2 Processing Outline

The overall processing outline of the SRB algorithm is summarized in Figure 3-1. The current SRB algorithm is implemented at a grid level consistent with the product horizontal resolution specified in the F&PS. Within each grid, there are up to four scene types including two clear (clear-sky snow/ice-free and clear-sky over snow/ice) and two cloudy scenes (water cloud and ice cloud), and the retrieval is carried out on a scene basis. The retrieved fluxes corresponding to each scene are then weighted according to the scene fractions to yield the all-sky flux. Algorithm inputs are prepared by collecting and averaging ancillary and ABI data within the spatial grids predefined for outputs. Scene types are determined based on the ABI cloud mask, snow/ice mask and cloud phase within each grid, and corresponding ABI channel reflectances and atmosphere and surface parameters are averaged separately. If the ABI total precipitable water (TPW) and ozone retrievals are not available, model or climatological values are used.

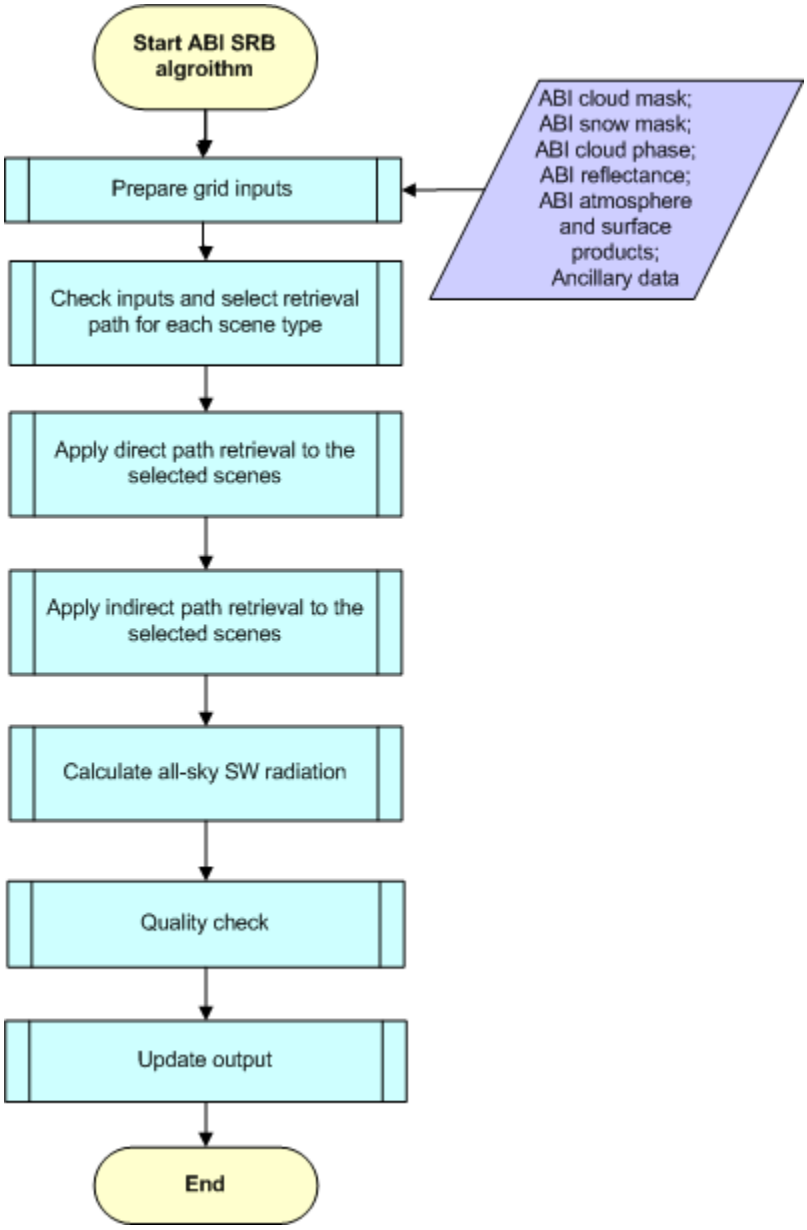

Figure 3-1. High level flowchart of the SWG algorithm illustrating the main processing sections.

The retrieval process follows two independent paths. The selection of the path used is based on the availability of ABI Level 2 retrieval products on a scene basis.

- The *direct path* is applied to a scene type when the required preceding ABI atmosphere and surface products are available (e.g., surface albedo, cloud optical depth, particle size, and top height for cloudy scenes; and aerosol optical depth and single scattering albedo for clear scenes). In this path, SW fluxes (DSR and RSR) are calculated directly from the inputs of surface albedo and atmospheric composition. Atmospheric transmittances and reflectances (optical functions) needed for this are pre-calculated for discrete values of these inputs, and are stored in lookup tables.

Instantaneous atmospheric optical functions for the actual ABI product inputs are calculated by interpolating the lookup tables. Figure 3-2 presents a schematic illustration of the direct retrieval path for a single scene type.

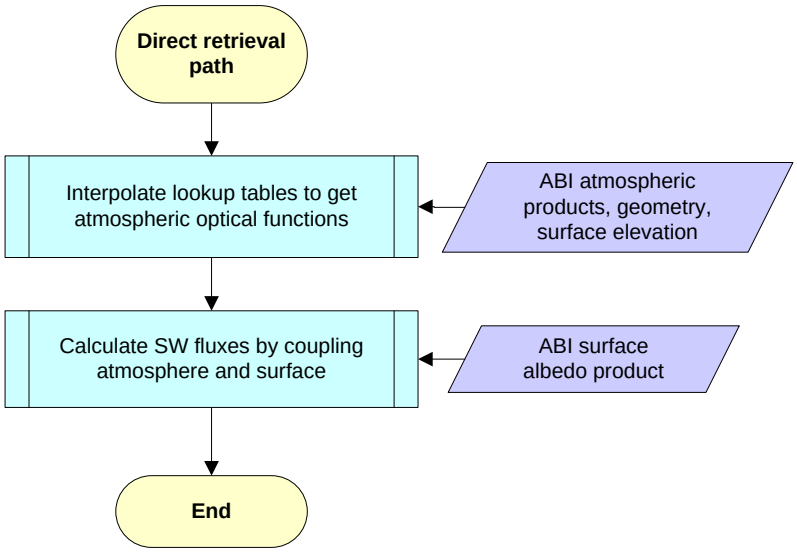

Figure 3-2. Flowchart of the direct path of SRB algorithm.

- The *indirect path* is applied when the absence of required ABI products (e.g., surface albedo, cloud optical depth, particle size, and top height for cloudy scenes; and aerosol optical depth and single scattering albedo for clear scenes) prohibits the direct path retrieval. Being an inversion scheme, the indirect path relies on the ABI channel reflectances to derive SW radiation budget in a self-consistent, energy-conserving manner.

  The approach requires establishing a clear-sky snow/ice-free composite TOA albedo for each grid. This composite albedo is assumed to represent average clear-sky conditions (climatological aerosol optical depth) and derived from cloud-free TOA albedos of a number of days over which the surface albedo is assumed to be constant. In the current version of the ABI algorithm, the composite is calculated as the median value of the clear-sky albedos from the current day and the previous 28 days (altogether 29 days) at the same observation time. The instantaneous clear-sky snow/ice-free TOA albedos are derived from the narrowband reflectances through the spectral and angular transformations.

  The indirect-path retrieval starts with the preparation of ancillary data, which includes: 1) acquiring climatological aerosol optical depth and single scattering albedo for the retrieval location and date; 2) deriving the atmosphere optical functions at discrete tabulated values of aerosol and/or cloud optical depths through the interpolation of lookup tables. The linear interpolation is performed to the actual solar zenith angle, surface elevation, total precipitable water and ozone amounts, as well as the aerosol single scattering albedo for the clear-sky case, and cloud radius

and top height for the cloudy scene; 3) obtaining the International Geosphere-Biosphere Programme (IGBP) surface type and corresponding reference spectral surface albedo based on the longitude and latitude coordinates. Then retrieval begins with estimating the surface albedo from the clear-sky composite albedo and climatological aerosol optical depth. Instantaneous atmosphere optical functions are then retrieved from the instantaneous TOA albedo; and surface and TOA SW fluxes are calculated by coupling the surface reflection and atmospheric reflection and transmission similar to that applied in the direct path. When snow/ice is detected under clear condition, a special scheme is adopted to avoid the large error associated with estimating the clear transmittance (essentially the aerosol optical depth) over bright surface. In this case, if exists, the instantaneous clear-sky atmospheric transmission retrieved over the snow/ice-free portion of the grid is assigned to the snow/ice covered portion as well. If no snow/ice free scene is present in the grid the clear-sky atmospheric transmittance corresponding to the climatological value of the aerosol optical depth is used. Snow/ice surface albedo is then derived from the instantaneous clear-sky TOA albedo, and SW fluxes are calculated with the prescribed atmospheric condition and retrieved surface albedo. For cloudy scenes within the grid, the surface type is assumed snow covered if the clear scene in the grid is dominated by snow/ice, and the surface albedo is calculated as the scene fraction weighted average of snow/ice-free and snow albedos. A schematic illustration of the indirect retrieval path is shown in Figure 3.3.

It should be emphasized that selection of the retrieval path is on a scene basis, thus it is possible that within a grid different retrieval paths are applied for the different scenes according to the availability of ABI products. All-sky DSR and RSR are calculated as a sum of the contributions from each scene weighted by its scene fraction.

At the output stage, retrieval results are evaluated based on the quality flags set in the retrieval process. Overall quality is determined and combined with the DSR and RSR values for output.

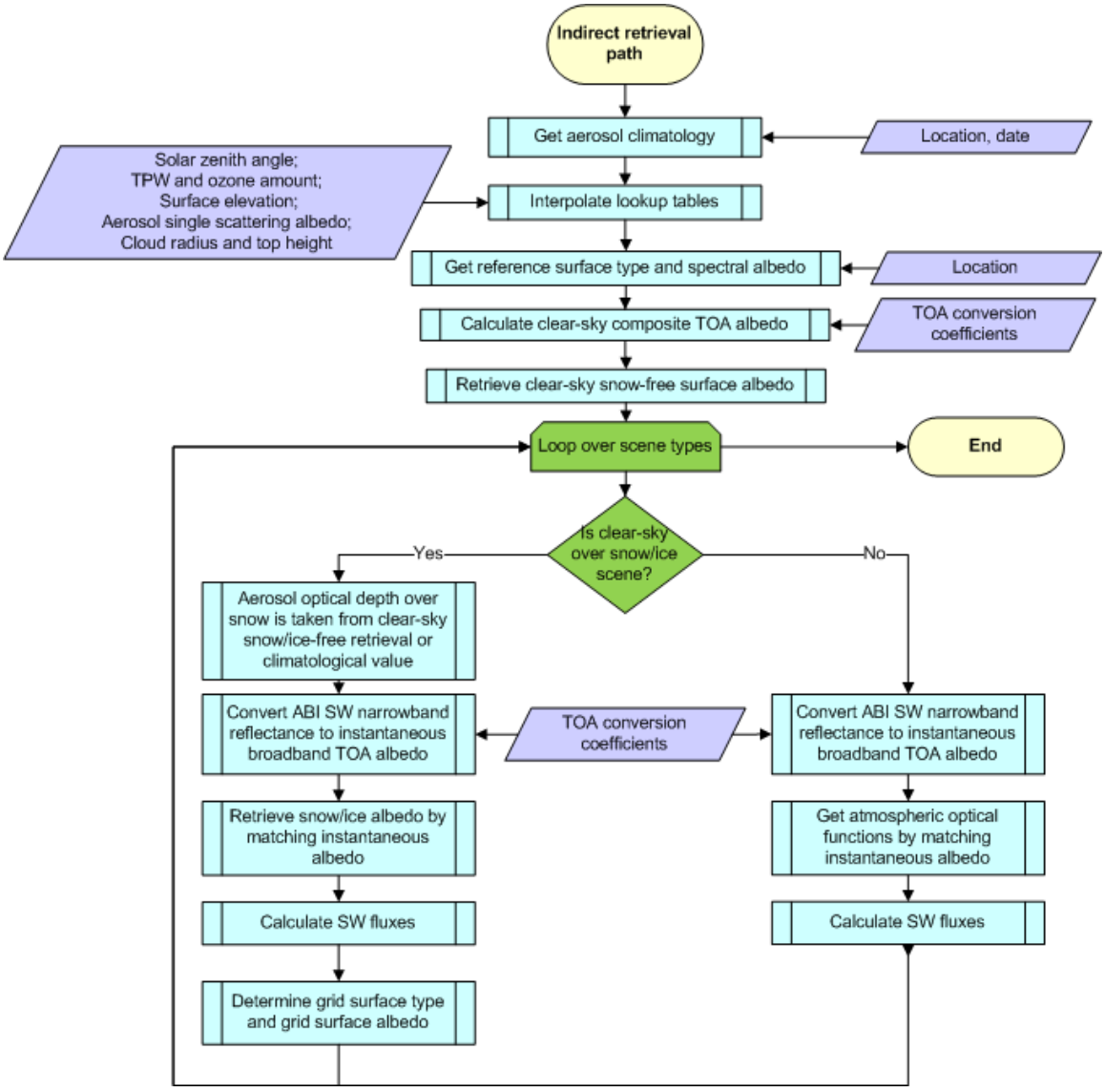

Figure 3-3. Flowchart of the indirect path of SRB algorithm.

3.3 Algorithm Input

This section describes the attributes of all input data used by the algorithm, including primary sensor data and ancillary data.

3.3.1 Primary Sensor Data

Table 3-1 lists the primary sensor data (data directly available from ABI) used by the algorithm, including calibrated ABI Level 1B reflectances, geolocation information, and

ABI sensor quality flags. All inputs are pixel level data with (xsize, ysize) denoting the two-dimensional (longitude-latitude) input size.

Table 3-1. ABI primary sensor data at pixel level.

Name	Type	Description	Dimension
Ch1 reflectance [i]	Input	Calibrated ABI reflectance at channel 1 - 0.47μm	pixel (xsize, ysize)
Ch2 reflectance [i]	Input	Calibrated ABI reflectance at channel 2 - 0.64μm	pixel (xsize, ysize)
Ch3 reflectance [i]	Input	Calibrated ABI reflectance at channel 3 - 0.86μm	pixel (xsize, ysize)
Ch4 reflectance [i]	Input	Calibrated ABI reflectance at channel 4 - 1.38μm	pixel (xsize, ysize)
Ch5 reflectance [i]	Input	Calibrated ABI reflectance at channel 5 - 1.61μm	pixel (xsize, ysize)
Ch6 reflectance [i]	Input	Calibrated ABI reflectance at channel 6 - 2.26μm	pixel (xsize, ysize)
Latitude [i]	Input	Center latitude	pixel (xsize, ysize)
Longitude [i]	Input	Center longitude	pixel (xsize, ysize)
Solar geometry [b]	Input	ABI solar zenith and azimuth angles	pixel (xsize, ysize)
View geometry [i]	Input	ABI local zenith and azimuth angles	pixel (xsize, ysize)
QC flags [i]	Input	ABI quality control flags with level 1b data	pixel (xsize, ysize)

* [i] : used by indirect path only; [b]: used by both paths

The actual sensor inputs are different for the two retrieval paths. The indirect path needs the reflectance data to establish the connection between reflection at TOA and transmission at surface; while the direct path only needs solar geometry for the forward radiative transfer computation. To be consistent with the horizontal resolution of the radiation products, pixel level sensor data are averaged within the required spatial grids (latitude and longitude retangular grid). The spatial resolution of these grids is such that they accommodate the horizontal spatial resolution requirements listed in Tables 2-1 and 2-2 with the assumption that one degree in latitude and longitude space equals 100 km. Arithmetic averaging of reflectance is done separately for the four scene types based on the ABI cloud mask, snow/ice mask, and retrieved cloud phase. Since all these reflectances are at TOA, grid-scale reflectance is conserved in the averaging. (To gage variability of reflectances within a grid min/max, mean, median, and standard deviation could be calculated. However, this is not done in the current version of the algorithm.) The grid level sensor inputs are summarized in Table 3-2.

Table 3-2. ABI primary sensor input data at grid level

Name		Type	Description	Dimension
Clear-sky	Ch1	Input	Mean calibrated ABI level 1b reflectance	grid (xsize, ysize)

snow/ice-free reflectance [i]			at channel 1 for clear-sky snow/ice-free pixels	
	Ch2	Input	Mean calibrated ABI level 1b reflectance at channel 2 for clear-sky snow/ice -free pixels	grid (xsize, ysize)
	Ch3	Input	Mean calibrated ABI level 1b reflectance at channel 3 for clear-sky snow/ice -free pixels	grid (xsize, ysize)
	Ch4	Input	Mean calibrated ABI level 1b reflectance at channel 4 for clear-sky snow/ice -free pixels	grid (xsize, ysize)
	Ch5	Input	Mean calibrated ABI level 1b reflectance at channel 5 for clear-sky snow/ice -free pixels	grid (xsize, ysize)
	Ch6	Input	Mean calibrated ABI level 1b reflectance at channel 6 for clear-sky snow/ice -free pixels	grid (xsize, ysize)
Clear-sky over snow/ice reflectance [i]	Ch1	Input	Mean calibrated ABI level 1b reflectance at channel 1 for clear-sky snow/ice pixels	grid (xsize, ysize)
	Ch2	Input	Mean calibrated ABI level 1b reflectance at channel 2 for clear-sky snow/ice pixels	grid (xsize, ysize)
	Ch3	Input	Mean calibrated ABI level 1b reflectance at channel 3 for clear-sky snow/ice pixels	grid (xsize, ysize)
	Ch4	Input	Mean calibrated ABI level 1b reflectance at channel 4 for clear-sky snow/ice pixels	grid (xsize, ysize)
	Ch5	Input	Mean calibrated ABI level 1b reflectance at channel 5 for clear-sky snow/ice pixels	grid (xsize, ysize)
	Ch6	Input	Mean calibrated ABI level 1b reflectance at channel 6 for clear-sky snow/ice pixels	grid (xsize, ysize)
Water-cloud reflectance [i]	Ch1	Input	Mean calibrated ABI level 1b reflectance at channel 1 for water-cloud pixels	grid (xsize, ysize)
	Ch2	Input	Mean calibrated ABI level 1b reflectance at channel 2 for water-cloud pixels	grid (xsize, ysize)
	Ch3	Input	Mean calibrated ABI level 1b reflectance at channel 3 for water-cloud pixels	grid (xsize, ysize)
	Ch4	Input	Mean calibrated ABI level 1b reflectance at channel 4 for water-cloud pixels	grid (xsize, ysize)
	Ch5	Input	Mean calibrated ABI level 1b reflectance at channel 5 for water-cloud pixels	grid (xsize, ysize)
	Ch6	Input	Mean calibrated ABI level 1b reflectance at channel 6 for water-cloud pixels	grid (xsize, ysize)
Ice-cloud reflectance [i]	Ch1	Input	Mean calibrated ABI level 1b reflectance at channel 1 for ice-cloud pixels	grid (xsize, ysize)
	Ch2	Input	Mean calibrated ABI level 1b reflectance at channel 2 for ice-cloud pixels	grid (xsize, ysize)
	Ch3	Input	Mean calibrated ABI level 1b reflectance at channel 3 for ice-cloud pixels	grid (xsize, ysize)

	Ch4	Input	Mean calibrated ABI level 1b reflectance at channel 4 for ice-cloud pixels	grid (xsize, ysize)
	Ch5	Input	Mean calibrated ABI level 1b reflectance at channel 5 for ice-cloud pixels	grid (xsize, ysize)
	Ch6	Input	Mean calibrated ABI level 1b reflectance at channel 6 for ice-cloud pixels	grid (xsize, ysize)
Latitude [i]		Input	Center latitude	grid (xsize, ysize)
Longitude [i]		Input	Center longitude	grid (xsize, ysize)
Solar geometry [b]		Input	ABI solar zenith and azimuth angles	grid (xsize, ysize)
View geometry [i]		Input	ABI local zenith and azimuth angles	grid (xsize, ysize)
QC flags [i]		Input	ABI quality control flags with level 1b data	grid (xsize, ysize)

* [d]: used by direct path only; [i]: used by indirect path only; [b]: used by both paths

3.3.2 Ancillary Data

The algorithm requires four types of ancillary data:

- ABI dynamic data (Table 3-3),
- Non-ABI dynamic (Table 3-4);
- ABI static data (Table 3-5)
- Non-ABI static data (Table 3-6).

3.3.2.1 ABI Dynamic Data

Table 3-3 lists the input data expected to come from ABI retrievals.

Table 3-3. ABI-derived dynamic data

Name	Type	Description	Dimension
Cloud mask [b]	Input	ABI level 2 clear sky mask data	grid (xsize, ysize)
Cloud phase [b]	Input	ABI level 2 cloud top phase data	grid (xsize, ysize)
Snow/ice mask [b]	Input	ABI level 2 Snow/ice cover data	grid (xsize, ysize)
Cloud optical depth [b]	Input	ABI level 2 cloud optical depth data	grid (xsize, ysize)
Cloud particle radius [b]	Input	ABI level 2 cloud particle size distribution data	grid (xsize, ysize)
Cloud top height [b]	Input	ABI level 2 cloud top height	grid (xsize, ysize)
Aerosol optical depth [d]	Input	ABI level 2 aerosol optical depth data	grid (xsize, ysize)
Aerosol single scattering albedo [d]	Input	ABI level 2 aerosol type data	grid (xsize, ysize)
Broadband surface	Input	ABI level 2 surface albedo data	grid (xsize, ysize)

albedo [d]			
Total precipitable water [b]	Input	ABI level 2 total precipitable water data	grid (xsize, ysize)
Ozone [b]	Input	ABI level 2 ozone total data	grid (xsize, ysize)

* [d]: used by direct path only; [b]: used by both paths

ABI cloud mask, cloud phase and snow/ice mask data are used for scene identification. Water cloud will be assumed if cloud phase is not available for identified cloudy pixels. Within each grid, arithmetic averaging is applied to the pixel-level ABI dynamic data. Cloud parameters, including optical depth, top height, and particle radius, are averaged separately for water and ice clouds. For the cloud and aerosol optical depth (τ), averaging is carried out in the log scale to preserve the TOA albedo ($\ln \bar{\tau} = \frac{\sum_{i=1}^{n} \ln \tau_i}{n}$). Mean aerosol single scattering albedo (ω_0) is an average weighted by optical depth ($\overline{\omega_0} = \frac{\sum \omega_{0,i} \tau_i}{\sum \tau_i}$). Since instantaneous surface albedo cannot be retrieved for cloudy scenes, clear-sky surface albedo is adopted for the cloudy portion of the grid, which is calculated as an average of clear-sky snow-free surface albedo and snow albedo weighted by the corresponding scene fractions. For the overcast grids, surface albedo derived from the clear-sky composite is used. There is no scene dependence of TPW and ozone, a single averaged value will be calculated for each grid.

It needs to be emphasized that although cloud optical depth, cloud particle size, and cloud top height are used also by the indirect path, they are not mandatory in the sense that in the absence of retrieved values these are taken from climatology (see Section 3.3.2.4).

3.3.2.2 Non-ABI Dynamic Data

When the ABI snow/ice mask (Snow/Ice Cover) is not available, data from the Interactive Multisensor Snow and Ice Mapping System (IMS) are used. In case the ABI total precipitable water (TPW) and ozone data are missing or not valid, Global Forecast System (GFS) data are used instead. The model data constitute the non-ABI dynamic data set (Table 3-4).

Table 3-4. Non-ABI dynamic data**.**

Name	Type	Description	Dimension
Model snow/ice mask [b]	input	Ice Mapping System (IMS) data	grid (xsize, ysize)
Model total precipitable water [b]	input	Global Forecast System (GFS) data	grid (xsize, ysize)
Model total ozone [b]	input	Global Forecast System (GFS) data	grid (xsize, ysize)

* [b]: used by both paths

3.3.2.3 ABI Static Data

ABI static data include the conversion factors used to estimate SW broadband reflectance from the ABI narrow-band measurements in the six SW channels 1, 2, 3, 4, 5, and 6 (see Section 3.4.1.3). (Conversion factors used for subsets of the six selected channels are currently under development.) To capture the spectral variation of TOA radiation under various conditions, clear-sky conversion coefficients are developed for different solar/local zenith angles and surface types. Ten solar zenith angle bins (centers: 12.9º, 30.8º, 41.2º, 48.3º, 56.5º, 63.2º, 69.5º, 75.5º, 81.4º and 87.2º), six local zenith angle bins (centers: 11.4º, 26.1º, 40.3º, 53.7º, 65.9º and 76.3º) and eight relative azimuth angle bins (centers: 1.91º, 9.97º, 24.18º, 44.02º, 68.78º, 97.55º, 129.31º and 162.89º) are adopted to prescribe the angular dependence. (The "unusual" selection of the angles is explained in Section 3.4.1.3) Twelve International Geosphere-Biosphere Programme (IGBP) surface types (water; needleleaf forest; broadleaf forest; mixed forest; woody savannas; savannas; closed shrubs; open shrubs; grasslands; croplands; desert and snow/ice) are incorporated in the clear-sky conversion to represent various boundary conditions. For the cloudy cases, conversion coefficients are developed for the same sets of angular bins; they are also a function of cloud phase, surface type and cloud optical depth. Two cloud phases (water and ice cloud), six cloud optical depth (0, 2.5, 6, 10, 18 and 40) and four surface types (water, land, desert and snow/ice) are included. The number of coefficients needed (Ncoef in Table 3-5) is a function of the instrument; for ABI the currently expected value is 7. (Note: The current algorithm uses MODIS reflectances as proxy. Currently, the conversions implemented for this sensor depend only on the solar zenith angle, see Section 3.4.1.3 for more information on why this is so.)

Table 3-5. Expected ABI-specific static ancillary input data.

Name	Type	Description	Dimension
Narrow-to-Broadband Conversion Factor [i]	Input	Coefficients for converting **clear-sky** satellite narrowband reflectance to broadband TOA albedo	(7, 8, 6, 10, 12) (Ncoef, NrelAzi, NsatZen, NsolZen, NsfcType)
		Coefficients for converting **water-cloud** satellite narrowband reflectance to broadband TOA albedo	(7,8,6,10,6,4) (Ncoef,NrelAzi, NsatZen,NsolZen, NcldTau,NsfcType)
		Coefficients for converting **ice-cloud** satellite narrowband reflectance to broadband TOA albedo	(7,8,6,10,6,4) (Ncoef,Nrelazi, NsatZen,NsolZen, NcldTau,NsfcType)

* [i]: used by indirect path only. Dimension variables: Ncoef: number of coefficients; NrelAzi: number of relative azimuth angle; NsatZen: number of local zenith angle; NsolZen: number of solar zenith angle; NsfcType: number of surface type; NcldTau: number of cloud optical depth.

3.3.2.4 Non-ABI Static Data

One of the major non-ABI Static data is the spectral lookup tables (LUT) of atmospheric reflection, direct/diffuse transmission and spherical reflection/transmission used by both direct and indirect paths. Detailed information of the LUT is presented in section 3.4.2.1 of this document. Surface elevation data is also needed by both the direct and the indirect paths, and is currently taken from the Global 30 Arc-Second Elevation Data Set (GTOPO30) of US Geological Survey (USGS) global topographic data digital elevation model. High resolution data is averaged to the spatial grids predefined for the ABI radiation products. Relevant details of GTOPO30 data are available from http://eros.usgs.gov/products/elevation/gtopo30.php. Climatology monthly mean data of total precipitable water and column ozone amount are derived from NCEP/DOE reanalysis and TOMS data at spatial resolution of 2.5º x 2.5º and 1.25º x 1º, respectively.

There are multiple ancillary data specific to the indirect path:

- International Geosphere-Biosphere Programme (IGBP) surface types are used to provide background information for the spectral surface albedo and TOA albedo conversion. Binary surface-type map at 1/6-degree resolution is taken from CERES/SARB surface properties website (http://www-surf.larc.nasa.gov/surf/pages/data-page.html). It is anticipated that a low spatial resolution map of surface type will be prepared to be compatible with product resolution.
- Reference spectral surface albedos between 0.2 and 4.0μm corresponding to the IGBP surface types are taken from CERES/SARB surface properties website (http://www-surf.larc.nasa.gov/surf/pages/data-page.html).
- Land/Sea mask is used to identify the coastal region where indirect retrievals might be of degraded quality.
- Aerosol climatology includes global aerosol monthly mean optical depth at 0.55μm (Liu et al., 2005) and single scattering albedo (Chin et al., 2002) at a spatial resolution of 2.5º x 2.0º. Figures 3-4 and 3-5 display the aerosol climatology currently used by the SRB algorithm.
- Climatology of water/ice cloud optical depth, radius and top height are derived from ISCCP products at a spatial resolution of 2.5º x 2.5º for each month. (It is implicitly assumed that the ISCCP based properties similar to the ABI derived cloud properties. In reality this may not be case, however, due to the differences in the ISCCP and ABI calibration/algorithms. It is expected, that eventually, an ABI based cloud climatology will replace the ISCCP climatology.)
- TOA reflectance-to-albedo conversion adopts CERES TRMM Angular Distribution Model (ADM) for clear and cloudy sky over land and ocean (Loeb et al., 2003), and CERES Terra ADMs over snow/ice (Kato and Loeb, 2005). For the clear-sky over water, CERES ADM at wind speed of 6 m/s is used.

It should be noted that with further algorithm development the ancillary data might be subject to modification.

Table 3-6. Non-ABI static ancillary input data.

Name	Type	Description	Dimension
Surface Height [b]	Input	US Geological Survey (USGS) global topographic data digital elevation model	(43200,21600) (Nlon, Nlat)
Total Precipitable Water Climatology [b]	Input	NCEP/DOE Reanalysis TPW monthly mean data	(144,73,12) (Nlon,Nlat, Nmonth)
Ozone Climatology [b]	Input	TOMS monthly mean ozone data	(288,180,12) (Nlon,Nlat, Nmonth)
Surface Type [i]	Input	International Geosphere-Biosphere Programme (IGBP) surface types	(2160,1080) (Nlon, Nlat)
Reference Spectral Surface Albedo [i]	Input	SW spectral surface albedo for IGBP surface type	(18,18) (Nband, NsfcType)
Land/Sea Mask [b]	Input	Global land/water/coast mask	1km
Aerosol Climatology [i]	Input	Optical depth at 0.55µm	(144,90,12) (Nlon, Nlat, Nmonth)
		Single scattering albedo at 0.55µm	
Cloud Climatology [i]	Input	Cloud optical depth	(144,72,12,2) (Nlon, Nlat, Nmonth,NcldPhase)
		Cloud radius	
		Cloud top height	
TOA Angular Distribution Model [i]	Input	CERES ADM for clear land	(10, 9, 9, 11) (NrelAzi, NsatZen, NsolZen, NsfcType)
		CERES ADM for clear ocean	(10, 9, 9) (NrelAzi, NsatZen, NsolZen)
		CERES ADM for cloudy land	(10, 9, 9, 6, 4, 2) (NrelAzi, NsatZen, NsolZen, NcldTau, NsfcType, NcldPhase)
		CERES ADM for cloudy ocean	(10, 9, 9, 14, 2) (NrelAzi, NsatZen, NsolZen, NcldTau, NcldPhase)
		CERES ADM for permanent snow	(10, 9, 45, 3, 2) (NrelAzi, NsatZen, NsolZen, NcldTau, NsfcType)
		CERES ADM for fresh snow	(10, 9, 18, 3, 2) (NrelAzi, NsatZen, NsolZen, NcldTau, NsfcType)
Lookup Table [b]	Input	Atmosphere reflection	(18,15,7,3,5,7,4) for clear sky (Nband, NsolZen, Ntpw,
		Atmosphere direct transmission	
		Atmosphere diffuse transmision	

		Atmosphere spherical albedo	No3, NsfcElv, Naod, Nssa)
		Atmosphere spherical transmission	(18,15,7,3,5,12,4,5,2) for water/ice cloud (Nband, NsolZen, Ntpw, No3, NsfcElv, Ncod, NcldRad, NcldHgt, NcldPhase)

* [d]: used by direct path only; [i]: used by indirect path only; [b]: used by both paths.
Dimension variables: Nlon: number of longitude; Nlat: number latitude; Nmonth: number of month; Nband: number of spectral band; NsfcType: number of surface type; NrelAzi: number of relative azimuth angle; NsatZen: number of local zenith angle; NsolZen: number of solar zenith angle; NcldTau: number of cloud optical depth; NcldPhase: number of cloud phase; NcldRad: number of cloud radius; Ntpw: number of total precipitable water value; No3: number of ozone value; NsfcElv: number of surface elevation; Naod: number of aerosol optical depth; Nssa: number of aerosol single scattering albedo.

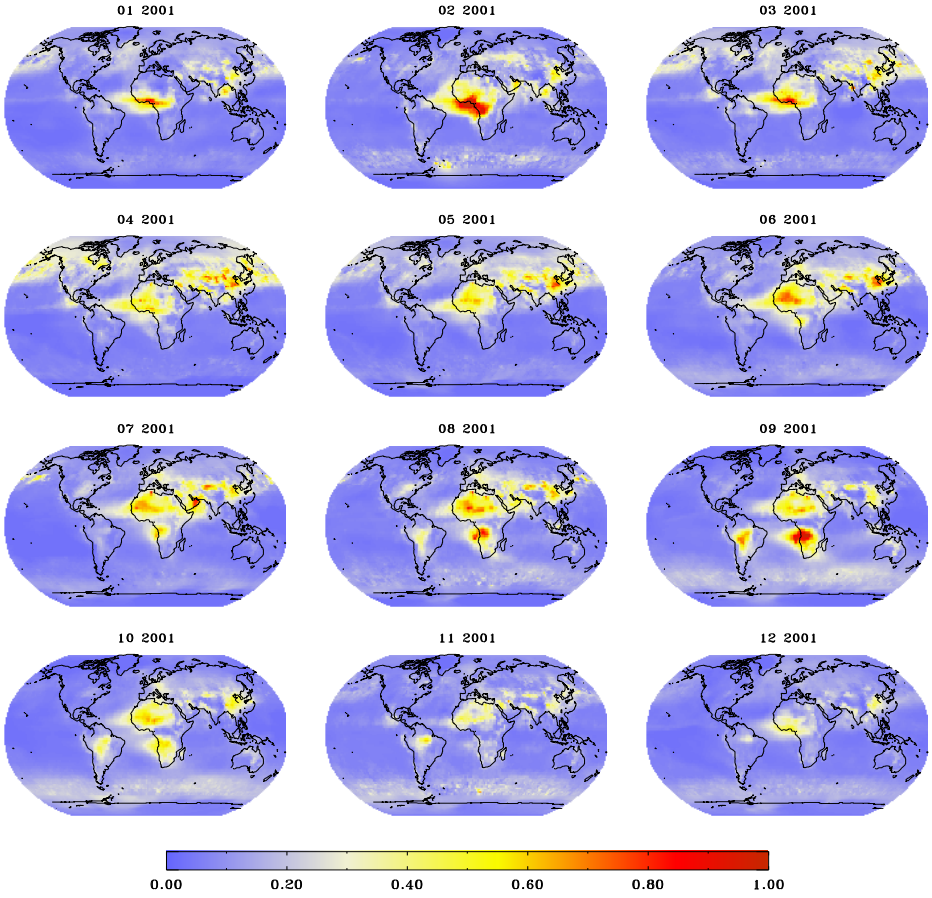

Figure 3-4. Global monthly mean aerosol optical depth at 0.55μm.

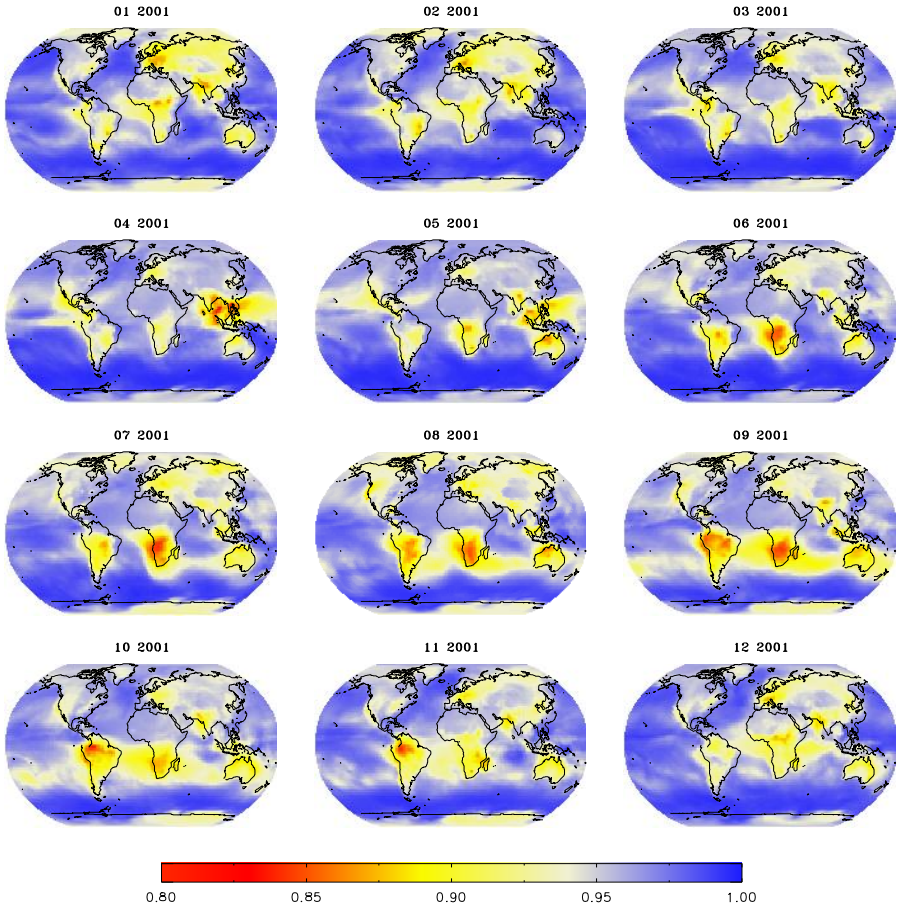

Figure 3-5. Global monthly mean aerosol single scattering albedo at 0.55µm.

3.3.2.5 Derived Data

N/A

3.4 Theoretical Description

This section describes the physics, radiative transfer, and associated phenomenology key to the retrieval. Description of the mathematics used by the retrieval, including all simplifications, approximations, and numerical methods are also presented, as well as description of the output of the algorithm as encoded in the data product.

3.4.1 Physics of the Problem

The SW radiation budget of the earth can be characterized if the downward and upward fluxes (hemispherically integrated radiances) are known. When the composition of the atmosphere (gases, cloud, and aerosol) and the reflectance of the surface are known these fluxes can be calculated from a radiative transfer model (RTM) for any position of the

sun. The direct path is based on this concept, and uses a modified version of the Fu-Liou RTM (Fu and Liou, 1993) with surface albedo, column amounts of water vapor and ozone, aerosol and cloud properties as primary inputs, to calculate the reflected SW fluxes at the top of atmosphere (RSR) and the fluxes transmitted to the surface (DSR).

The SW fluxes can also be retrieved from satellite measurements using the fact that there is a well-defined approximate relationship between the TOA reflectance and the total downward flux transmittance in the shortwave part of the spectrum. This is because both quantities are determined by the same set of parameters: aerosol and cloud properties, water vapor and ozone absorption, surface albedo and illumination geometry. The STAR/UMD algorithm (indirect path) uses a reflectance-transmittance method to estimate the SW fluxes at the top of atmosphere and at the surface. The relationship between reflectance and transmittance is calculated from the Fu-Liou radiative transfer model (Fu and Liou, 1993) for discrete values of the defining parameters.

In calculating the reflectances and transmittances the SW broadband is divided into 18 sub-bands (0.175-0.224; 0.224-0.243; 0.243-0.285; 0.285-0.298; 0.298-0.322; 0.322-0.357; 0.357-0.437; 0.437-0.497; 0.497-0.595; 0.595-0.689; 0.689-0.794; 0.794-0.889; 0.889-1.042; 1.042-1.410; 1.410-1.905; 1.905-2.500; 2.500-3.509; 3.509-4.000 μm). Such spectral partitioning is dictated by the fact that SW surface albedo and atmospheric scattering and absorption exhibit great wavelength dependence (Rutan et al., 2009). Figure 3-6 shows the spectral albedo for typical surface types. The surface spectral albedos are taken from the CERES/SARB web site at http://www-surf.larc.nasa.gov/surf/pages/explan.html.

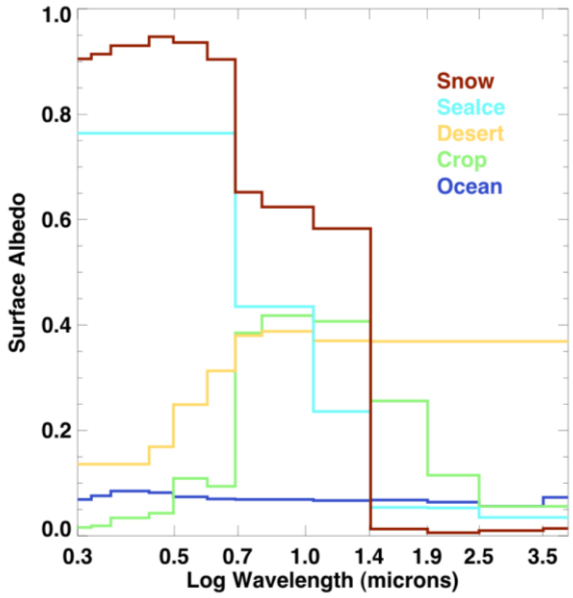

Figure 3-6. Spectral albedos of typical surface types.

3.4.1.1 The direct path

The direct path is an adaptation of the NASA CERES algorithm. It calculates the DSR and RSR using a lookup table generated from a modified version of the Fu-Liou RTM (Fu and Liou, 1993) with surface albedo, column amounts of water vapor and ozone, aerosol and cloud properties as primary inputs. Because the direct path uses ABI derived parameters as inputs the fluxes derived are consistent with these parameters.

The modified Fu-Liou code here referred to as FLCKKR (an acronym using the first letter of the last names of persons contributing to its development) was developed by the Clouds and the Earth's Radiant Energy System (CERES) group at NASA Langley.

With 18 bands in the SW, the code has enough spectral resolution for the sufficient treatment of Rayleigh scattering and ozone absorption. Band absorption of gases is calculated using the correlated-k distribution method. The *k*-coefficients were determined from the HITRAN 2000 data base. To reduce the number of *k*s and increase computational speed, gas concentrations of the minor absorbers (CO_2, O_3, CH_4, O_2) in the near infrared (NIR) bands were fixed at year 2000 levels. Continuum absorption is included as well. (The concentration data and the k-coefficients from later releases of HITRAN could be updated as needed before the launch of GOES-R.)

A gamma weighted two-stream solver option is used to model effects of cloud optical depth inhomogeneity (Kato et al., 2001). The original 2-stream and 4-stream solvers from the original Fu-Liou model remain options for a homogeneous cloud assumption as well. Figure 3-7 shows the calculated TOA albedo from FLCKKR under various conditions.

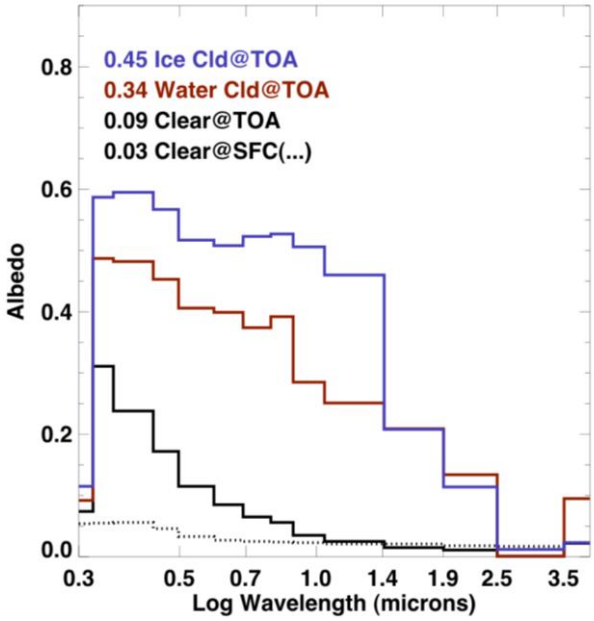

Figure 3-7. Top-of-atmosphere spectral albedo calculated from FLCKKR for clear sky ocean with the sun overhead (Clear@TOA), water cloud with visible optical depth 10 and effective radius 10 microns (Water

Cld@TOA), ice cloud with visible optical depth of 10 and effective diameter of 60 microns (Ice Cld@TOA). The ice cloud is more reflective in the visible due to a smaller asymmetry parameter than that of water cloud. It is less reflective in the near infrared (past wavelength of 1.4 μm) due to larger absorption by ice. For comparison, the dotted line shows the spectral albedo of clear-sky ocean surface (Clear@SFC). The numbers in the legend are the integrated, broadband albedos.

Water cloud optical properties are from Mie calculations of cloud optical properties from Hu and Stamnes (1993). Ice cloud properties for shortwave are those of Fu (1996) of randomly oriented hexagonal crystals, requiring the input of a generalized effective diameter (D_{ge}). In order to be compatible with an input particle size of *effective diameter* (D_e) as generated in the MODIS based CERES cloud working group retrieval of cloud properties (Minnis et al., 1998), a parameterization was developed to insure the particle size based extinction at 0.6 μm in the FLCKKR code using *generalized effective diameter* (D_{ge}) was equivalent to that assumed in the MODIS/Minnis cloud property retrieval of D_e.

Clear-sky aerosols include one oceanic (Dubovik et al., 2002) and four land aerosol models (dust, urban, generic and absorbing aerosols). These land aerosol models are the same as those used in the ABI aerosol retrieval (Users are referred to the ABI aerosol optical depth ATBD for details on the aerosol models). Vertical distribution of aerosol is assumed to be exponential with a scale height of 3 km. Presently, aerosol variability is only in the clear condition. Simultaneous retrieval of cloud and aerosol properties is dubious, so for cloudy sky aerosol effect is fixed to be a constant amount of continental aerosol ($\tau_{0.55\mu m}$=0.2). One might be tempted to use the clear-sky value of aerosol even in cloudy cases, however, climatology of aerosol under cloudy conditions is likely to be different from that under cloud-free conditions, and to our knowledge such climatology does not yet exist. Also, to keep the size of the cloud lookup table at a manageable level a single fixed aerosol optical depth is used, for now both over land and ocean. Surface albedo input is assumed to be Lambertian and expected to be available from the ABI Level 2 product.

To increase computational efficiency, the direct path uses lookup tables instead of calling the modified Fu-Liu code. The lookup table (LUT) is based on the FLCKKR shortwave model for a suite of computations under various environmental conditions. The lookup table complexity increases exponentially with the number of lookup input variables. To make the LUT manageable and be as accurate as possible, tables of atmospheric reflectivity, direct and diffuse transmissivity, and spherical reflectivity and transmissivity at 18 spectral bands were generated corresponding to the scenes of clear-sky, water cloud and ice cloud. Sensitivity of broadband transmission and TOA albedo is highly dependent on cloud coverage and optical properties. Any uncertainty in the retrieval of cloud and aerosol properties, as well as the surface albedo will overwhelm the errors raised from radiative transfer calculation.

For clear sky, as well as cloudy sky, the variability of water vapor and ozone and their absorption is included using column integrated values. Their vertical profiles are predefined for a standard atmosphere. The LUT input of surface elevation does not affect the water vapor or ozone amounts but does change the total column thickness for other minor absorbers such as CO_2, CH_4, and O_2. Surface elevation also affects the degree of Rayleigh scattering that occurs.

For clear sky LUT, aerosol optical depth at 550 nm and single scattering albedo are used as aerosol inputs. In the LUT, aerosol single scattering albedo serves as a surrogate for aerosol type with different spectral absorptions and scattering characteristics. The aerosol types used have unique single scattering albedos and thus the single scattering albedo required for the LUT can be uniquely identified from the input aerosol type. Since the land aerosol types incorporated in the LUT are the same as those used in the ABI aerosol retrievals, using ABI retrieved aerosol type as input should reduce the uncertainty due to potential mismatch of aerosol models.

The cloudy LUT includes inputs of cloud optical depth, cloud particle size, and cloud top height. Cloud geometric thickness varies dependent on cloud optical depth and cloud top height. This relationship is taken from the First ISCCP Regional Experiment (FIRE) field study (Minnis et al., 1992) of primarily stratocumulus clouds. This parameterization has been recently updated using CALIPSO and CloudSat data (P. Minnis, private communication), and will be used in the next version.

3.4.1.2 The indirect path

The indirect path is based on the STAR/UMD algorithm that estimates the DSR and RSR from satellite-derived TOA albedos using pre-calculated relationships between SW reflectance and transmittance. Details on the model and its implementation with various data sets are provided, for example, in Pinker and Laszlo (1992), Pinker et al. (2002, 2003), and Laszlo and Pinker (2002).

The transmittance-reflectance relationship and the principle of the radiation budget retrieval are illustrated in Figure 3-8 for a clear and a cloudy scene with given values of water vapor and ozone and illumination geometry (solar zenith angle). Figure 3-8 plots the shortwave (broadband) flux transmittance as a function of the TOA broadband reflectance for increasing values of the aerosol and cloud optical depths (optical depth increases from left to right). The transmittance-reflectance relationships have different slopes. Because aerosol is more absorbing than cloud in the shortwave the slope of the relationship for aerosol is steeper. In the flux retrieval the clear and cloudy relationships are used to "read-off" the clear and cloudy transmittances corresponding to the satellite-derived TOA reflectances (albedos). In the example shown in Figure 3-8, the clear-sky TOA albedo is 0.1 corresponding to a transmittance value of 0.69. The cloudy-sky values are 0.5 (TOA reflectance) and 0.28 (transmittance).

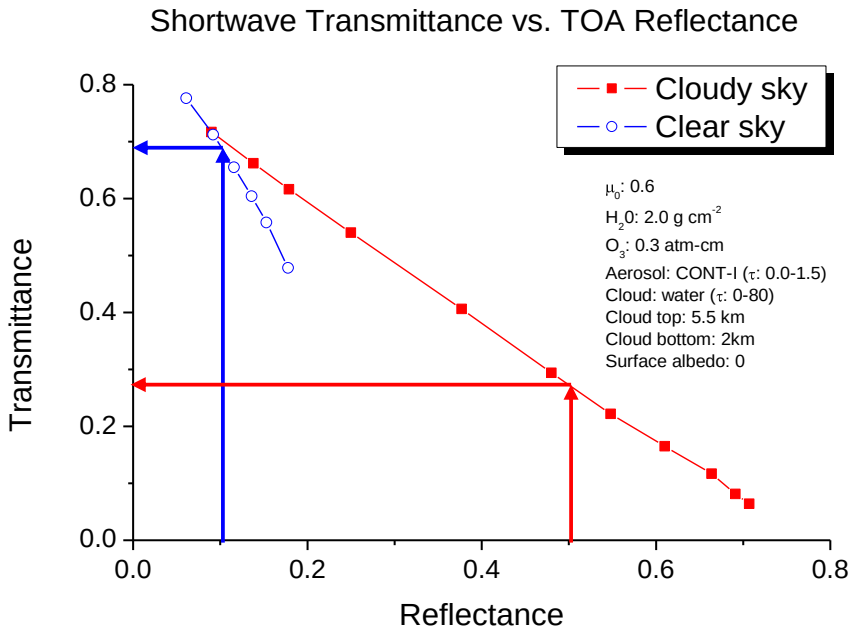

Figure 3-8. Illustration of the transmittance-reflectance relationship and its use in the estimation of downward surface SW radiation.

The indirect path adopts the same atmospheric optical function LUTs as used by the direct path to ensure a consistent radiative transfer calculation executed in the ABI SRB algorithm. In order to estimate the fluxes for any specific scene type (clear-sky snow/ice-free, clear-sky over snow/ice, water cloud, and ice cloud), the indirect path proceeds with the following steps:

1. Ancillary data, including aerosol climatology (optical depth and single scattering albedo at 0.55 μm), IGBP surface type and associated spectral surface albedo for the processing grid is extracted. LUTs are interpolated to the input solar zenith angle, surface elevation, water vapor, and ozone amount. Clear-sky LUTs are further interpolated to the climatological aerosol single scattering albedo, and cloudy LUTs are interpolated to the input effective cloud radius and cloud top height. As a result, atmospheric optical functions with varying values of aerosol or cloud optical depths are obtained for establishing the transmittance-reflectance relationship in the following steps.
2. Instantaneous snow-free surface albedo is estimated from the clear-sky composite albedo through atmospheric correction. The underlying assumption is that surface albedo varies slowly in time and can be derived from recent measurements in a statistical manner. In this step, clear-sky composite albedo is derived as the median value of previous 29 days (including current day) clear-sky snow-free TOA albedo converted from reflectance measurements; atmospheric reflectance and transmittance is determined by interpolating the clear-sky LUTs to the

climatological aerosol optical depth. The retrieved surface albedo will have the spectral shape of the reference albedo with the magnitude being adjusted.

3. For the clear-sky snow/ice-free and cloudy scene types, clear and cloudy transmittance and reflectance are retrieved by adjusting aerosol or cloud optical depths toward agreement with the instantaneous clear and cloudy TOA albedos respectively. For this, the instantaneous observed TOA albedo is derived from the instantaneous ABI reflectance through spectral (NTB) conversion and angular correction. Combined with the derived surface albedo derived, TOA albedos are calculated for various values of the aerosol or cloud optical depth. Atmospheric transmittance and reflectance is then retrieved by searching for the appropriate (aerosol and cloud) optical depth to match the observed albedo. SW flux corresponding to the specified scene type is calculated from surface albedo and the determined atmospheric reflectance and transmittance.
4. If snow/ice is detected under clear-sky condition, the snow/ice surface albedo is derived from the instantaneous TOA albedo converted from the instantaneous reflectance of the clear-sky over snow/ice scene type. Instantaneous atmospheric optical functions are prescribed based on the retrieved aerosol optical depth from the clear-sky snow/ice-free scene type (if it is available) or climatological value, and SW fluxes are calculated based on this prescribed atmospheric condition and derived snow/ice albedo. For the following retrievals over cloudy scene types, grid surface type is assigned to the snow/ice cover if clear fraction is dominated by snow/ice, and grid surface albedo is computed as the weighted average of snow/ice-free and snow surface albedo based on their scene fractions.
5. Finally, grid SW fluxes are calculated by averaging the fluxes corresponding to the individual scene types weighted by their scene fractions.

There is a possibility that the retrieved surface albedo may fall beyond the physically possible range (0 and 1) in certain spectral bands. Under such circumstance, the reference surface albedo is used instead and a quality flag is set to indicate the possible degradation of the retrieval. Similarly, TOA albedo calculated from tabulated aerosol/cloud optical depths might not converge to the measurement, for such cases, the extreme optical depth value in the LUT will be taken as the retrieved value and a corresponding quality flag is set.

The process described above requires an estimate of the TOA broadband albedo for clear and cloudy scenes. The method used for getting this albedo is discussed in the next section.

3.4.1.3 NTB and ADM conversions

The indirect path requires the knowledge of SW (broadband) TOA albedo for estimating SW fluxes. This is accomplished by a module developed at the University of Maryland (UMD) to obtain the SW TOA albedo from the narrowband ABI reflectances. The critical elements of this module are:

1. Transformation of narrowband quantities into broadband ones, narrow-to-broadband conversion (NTB);

2. Transformation of bidirectional reflectance into albedo by applying Angular Distribution Models (ADMs).

In principle, the order in which these transformations are executed is arbitrary. However, since well established, observation based *broadband* ADMs derived from the Earth Radiation Budget Experiment (ERBE) and the Clouds and the Earth's Radiant Energy System (CERES) project already exist, the logical procedure is to do the NTB on the reflectances first, and then apply the ADM. This is the sequence that has been followed. For developing the transformation between narrowband and broadband reflectances, such reflectances are simulated for a variety of realistic scene types (atmospheric and surface conditions), and for varying geometries. In order to be consistent with the existing ADMs the scene types used in the simulations should match those used in ADMs.

The derivation of NTB conversion coefficients is based on establishing a relationship between broadband and narrowband reflectances, which generally depend on solar and local zenith and azimuth angles, surface type, atmospheric conditions, clouds and spectral response of the satellite sensors. For clear sky conditions, aerosols are also important. The availability of sophisticated radiative transfer models for simulating the observations of both narrowband and broadband reflectances allows one to study relationships in a controlled manner, because atmospheric, surface, and viewing geometry conditions can be varied systematically, which is difficult to accomplish in an empirical study (Laszlo et al., 1988). For the theoretical simulation the MODTRAN 3.7 (Berk et al., 1983) radiative transfer model was used. After simulating both narrowband and broadband reflectance values for a variety of atmospheric, surface, and viewing conditions and converting to reflectance, the NTB relationships are derived through linear regression.

The processing outline of the NTB algorithm used to derive the needed coefficients is summarized in the Figure 3-9.

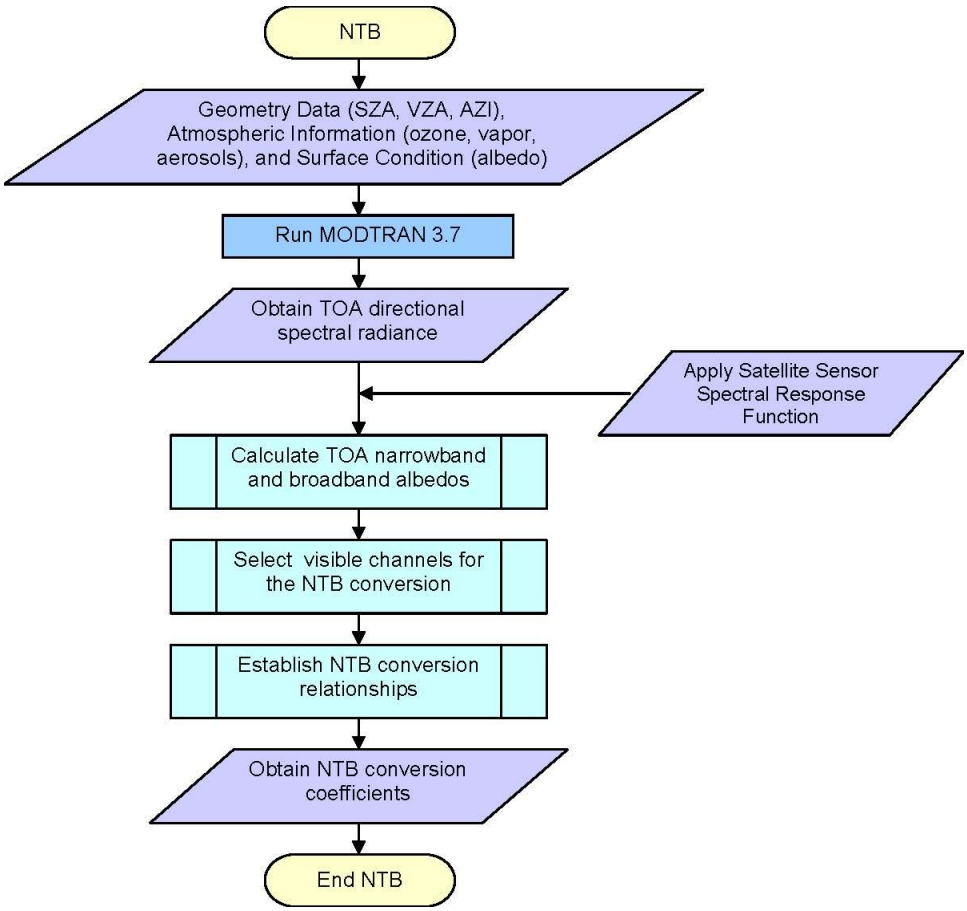

Figure 3-9. Flowchart of the NTB, illustrating the main processing sections

Two possible approaches are commonly used to derive ADMs: theoretical and empirical. Both have their advantages and disadvantages. Our approach is to synthesize both options into a hybrid approach. The empirical models are based on the newly developed CERES reference ADMs, which are stratified according to scene types and have a relatively high angular resolution. The higher local zenith angles are under-sampled by the CERES instrument (Loeb et al. 2003). To compensate for this, we combined the CERES ADMs with those derived theoretically through simulations with MODTRAN 3.7. The combined ADMs are developed for each angular bin by weighting the modeled and CERES ADMs based on the number of samples used to derive the ADMs of each type.

The process that synthesizes the model simulated and observed ADMs is described in the flow chart in Figure 3-10. The algorithm is based on IGBP surface classifications and CERES and simulated ADMs.

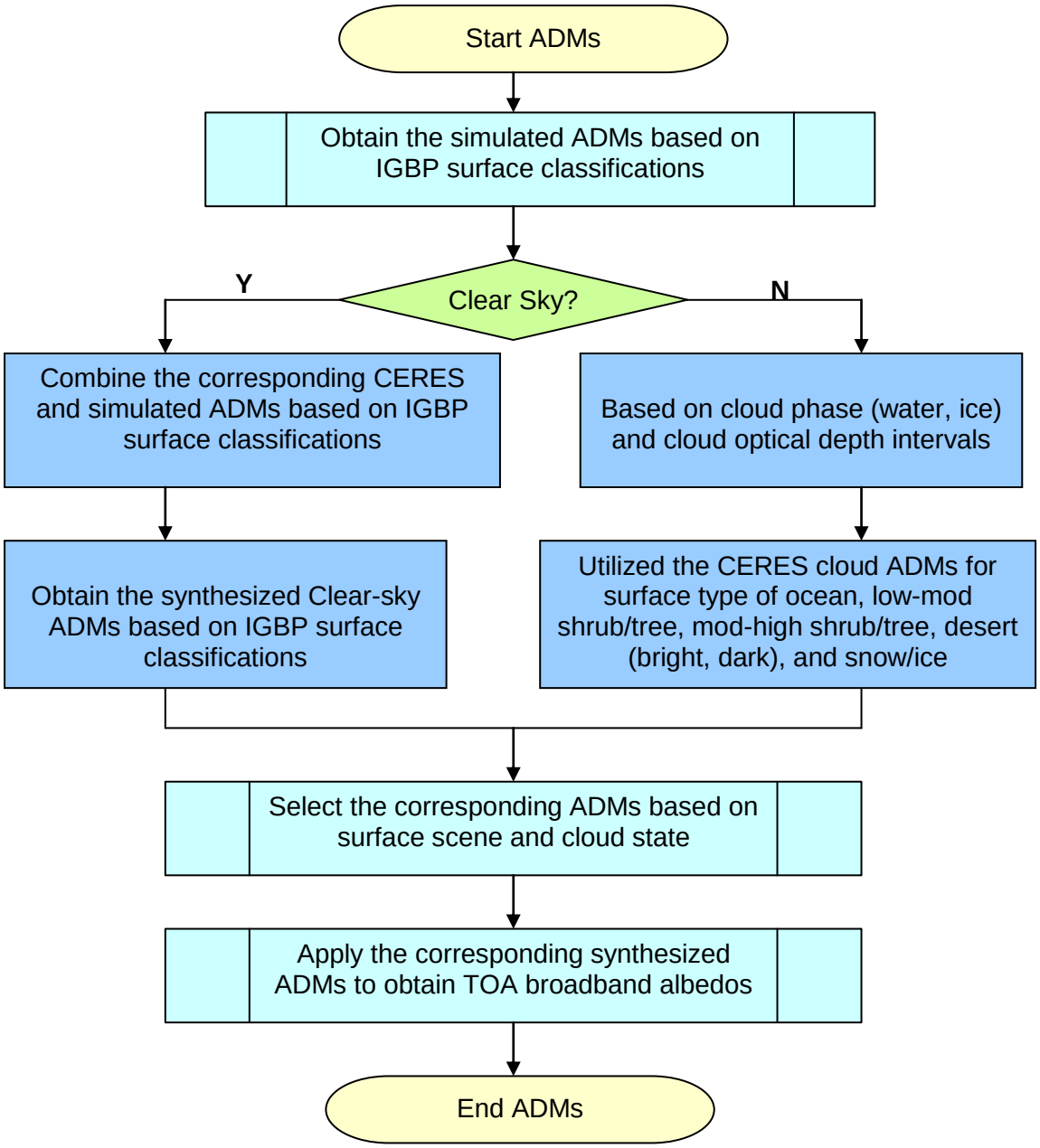

Figure 3-10. Schematic illustration of the logic employed to synthesize modeled and observed ADMs.

The primary inputs used in the MODTRAN 3.7 simulations are as follows:

- Geometry parameters (solar zenith angle, local zenith and azimuth angle): In order to represent the variability in solar geometry the calculations are performed for 10 solar zenith angles. In order to obtain angular dependent relationships the simulations are performed in 6 local zenith angles and 8 azimuth angles.

- Atmospheric conditions (profiles of ozone, water vapor, and aerosols): Climatological profiles of temperature, ozone, water vapor grouped by season (20 profiles for each season) are used, which are derived from the TIROS Initial Guess Retrieval (TIGR) profiles (Chedin et al., 1985) profiles modified with the four years of Forest System Laboratory (FSL) rawinsond information. For each season, variability of atmospheric aerosols is represented by three visibilities (18, 23, and 28 km). For cloud simulations, six types of default clouds provided in MODTRAN 3.7 are used. They are: cumulus, altostratus, stratus, stratocumulus, nimbostratus, and cirrus.
- Surface conditions: Surface types are grouped based on IGBP surface scenes, which include: Water, Needleleaf Forest, Broadleaf Forest, Mixed Forest, Wooded Savannas, Savannas, Closed Shrublands, Open Shrublands, Grasslands, Croplands, Bare Ground, and Snow and Ice. Spectral reference albedos of the surface are based on AVHRR channel 1 (0.58 to 0.68) and channel 2 (0.725 to 1.10) global monthly mean reflectance at the TOA from GVI dataset (Gutman and Ignatov, 1998). This allows for the introduction of seasonality which is not commonly included in simulations. Four band surface reflectance models were derived based on the Briegleb et al. (1986) albedo models, the GVI and the Advanced Space Thermal Emission and Reflection Radiometer (ASTER) library (Gillespie et al., 1998). The ASTER spectral library is a compilation of almost 2000 spectra of natural and man-made materials from three different spectral libraries: the Johns Hopkins University (JHU) Spectral Library, the Jet Propulsion Laboratory (JPL) Spectral Library, and the United States Geological Survey (USGS-Reston) Spectral Library. The spectral coverage is from 0.3 to 25 μm.

The above inputs are summarized in Table 3-7.

Table 3-7. Inputs to MODTRAN 3.7 simulations

Parameter	Values
Surface spectral reflectance model	12 IGBP surface types ; 4 seasons; 5 spectral intervals (μm): 0.2-0.5; 0.5-0.7; 0.7-1.3; 1.3-2.0; 2.0-4.0
Atmospheric Profile (40-level temperature, ozone, water vapor)	4 seasons (5 profiles each season); 40 levels for each profile(Height [km]): 0.01, 0.53, 1.04, 1.53, 2.05, 2.88, 3.76, 4.65, 5.35, 6.25, 7.15, 7.85, 8.55, 9.30, 10.10, 10.65, 11.15, 12.11, 13.25, 14.85, 16.11, 17.50, 19.00, 20.00, 21.50, 22.50, 26.00, 28.50, 31.00, 34.00, 37.50, 40.00, 42.50, 45.00, 48.00, 55.00, 60.00, 65.00, 70.00, 75.00
Visibility [km]	18, 23, 28
Solar Zenith Angle [°]	12.9, 30.8, 41.2, 48.3, 56.5, 63.2, 69.5, 75.5, 81.4, 87.2
local Zenith Angle[°]	11.4, 26.1, 40.3, 53.8, 65.9, 76.3

Azimuth Angle[°]	1.9, 10.0, 24.2, 44.0, 68.8, 97.6, 129.3, 162.9	
Cloud Phase	Water Cloud (Stratocumulus); Ice Cloud (Cirrus, Altostratus)	
Cloud Optical Depth Intervals	Stratocumulus	0-0.8; 0.8-1.2; 1.2-1.8; 1.8-3.2; 3.2-5.8; 5.8-8.2; 8.2-15.8; 15.8-32.2; 32.2-51.8; 51.8-124.2; > 124.2
	Cirrus	0-0.8; 0.8-1.2; 1.2-1.8; 1.8-3.2; >3.2
	Altostratus	0-15.0; 15.0-30.0; 30.0-50.0; 50.0-80.0; > 80.0

3.4.2 Mathematical Description

The downward SW radiation at the surface (DSR) and reflected SW radiation at TOA (RSR) are calculated in the SRB algorithm as the product of the retrieved transmittance *T* and reflectance *R* and the extraterrestrial solar irradiance. The latter is obtained from the solar constant S_0 by correcting it for the actual sun-earth distance *d* (in astronomical units) and solar zenith angle θ_0, that is:

$$DSR = T\cos\theta_0 \frac{S_0}{d^2} \quad (1)$$

$$RSR = R\cos\theta_0 \frac{S_0}{d^2} \quad (2)$$

The direct and indirect paths adopt different schemes to retrieve *R* and *T*. Their mathematical details are introduced in the following sections.

The scene-weighting process can be expresses as: $F = \sum_{i=1}^{4} f_i F_i$ where F_i is the flux (DSR or RSR) corresponding to the scene type i, f_i is the scene fraction and $\sum_{i=1}^{4} f_i = 1$. F is the all-sky flux for the grid.

3.4.2.1 The direct path

The direct path derives the atmospheric optical functions (reflectivity R^0; direct and diffuse transmissivity T_{dir}^0, T_{dif}^0; spherical reflectivity $\tilde{R}$ and transmisivity $\tilde{T}$) directly by interpolating LUT from the input solar zenith angle θ_0 and atmosphere parameters. Combined with the input SW surface albedo α, total reflectance *R* and transmittance *T* are calculated based on the adding equation of radiative transfer (Chandrasekhar, 1960):

$$R(\theta_0) = R^0(\theta_0) + r\tilde{T} \quad (3)$$

$$T(\theta_0) = T^0(\theta_0) + r\tilde{R} \quad (4)$$

where

$$r = \frac{\alpha T^0(\theta_0)}{1 - \alpha \tilde{R}} \tag{5}$$

$$T^0(\theta_0) = T^0_{dir}(\theta_0) + T^0_{dif}(\theta_0) \tag{6}$$

The SW broadband atmospheric optical functions are derived from the spectral values weighted by the extraterrestrial solar irradiances in each spectral interval.

Three LUTs are generated; they are for clear, water cloud and ice cloud scene types. As shown in Tables 3-8 and 3-9, the clear-sky LUT of atmospheric optical functions are functions of spectral bands, solar zenith angle, total precipitable water, ozone, surface elevation, aerosol optical depth at 0.55μm, and aerosol single scattering albedo (surrogate for aerosol type). Similarly, the LUT of cloudy sky optical functions depend on the spectral bands, solar zenith angle, total precipitable water, ozone, surface elevation, visible cloud optical depth, cloud radius and cloud top height.

Table 3-8. Extent of Clear-Sky Lookup Table

Parameter	Values	N
SW spectral Bands (μm)	0.175-0.224; 0.224-0.243; 0.243-0.285; 0.285-0.298; 0.298-0.322; 0.322-0.357; 0.357-0.437; 0.437-0.497; 0.497-0.595; 0.595-0.689; 0.689-0.794; 0.794-0.889; 0.889-1.042; 1.042-1.410; 1.410-1.905; 1.905-2.500; 2.500-3.509; 3.509-4.000	18
Cosine Solar Zenith Angle	.01, .025, .05, .08, .1, .15, .2, .3, .4, .5, .6, .7,.8, .9, 1.0	15
Natural log (Precipitable Water) [cm]	-4, -3, -2, -1, 0, 1, 2	7
Total Ozone [DU]	200, 350, 500	3
Surface Elevation [m]	-200, 0, 500, 1250, 4200.	5
Natural log(Aerosol Optical Depth)	-5, -4, -3, -2, -1, 0, 1	7
Aerosol Single Scattering Albedo at 0.55 μm (aerosol types)	0.9718, 0.955, 0.9429, 0.925, 0.8674 Oceanic, dust, urban, generic, absorbing	5

Table 3-9. Extent of Cloudy-Sky Lookup Table

Parameter	Values	N
SW spectral Bands (μm)	0.175-0.224; 0.224-0.243; 0.243-0.285; 0.285-	18

		0.298; 0.298-0.322; 0.322-0.357; 0.357-0.437; 0.437-0.497; 0.497-0.595; 0.595-0.689; 0.689-0.794; 0.794-0.889; 0.889-1.042; 1.042-1.410; 1.410-1.905; 1.905-2.500; 2.500-3.509; 3.509-4.000	
Cosine Solar Zenith Angle		.01, .025, .05, .08, .1, .15, .2, .3, .4, .5, .6, .7, .8, .9, 1.0	15
Natural log (Precipitable Water) [cm]		-4, -3, -2, -1, 0, 1, 2	7
Total Ozone [DU]		200, 350, 500	3
Surface Elevation [m]		-200, 0, 500, 1250, 4200.	5
Natural log (Cloud Optical Depth)		2, -1, -0.5, 0, 0.5, 1.0, 1.5, 2.0, 2.5, 3, 4, 5	12
Cloud Effective Radius [μm]	Water Cloud	8, 12, 20, 30	4
	Ice Cloud	15, 30, 60, 90	
Cloud Top Height [m]		0, 3000, 5000, 8000, 14000	5

Calculation of the spherical quantities would require calculation of bidirectional reflectances and transmittances followed up with an integration of these quantities over the angles. It is not possible to calculate the bidirectional quantities from the modified Fu-Liou code since that code computes fluxes directly. Therefore, Equations (3) and (4) are used to calculate $\tilde{R}$ and $\tilde{T}$. For this the RTM is first run with a zero surface albedo that yields R^0 and T^0 directly, since r is zero in this case. Next, the RTM is run for the same atmosphere with a non-zero surface albedo (e.g., $\alpha = 0.3$). Then the spherical reflectivity ($\tilde{R}$) and transmissivity ($\tilde{T}$) are calculated as:

$$\tilde{R} = \frac{T - T^0}{\alpha T} \qquad (7)$$

$$\tilde{T} = \frac{R - R^0}{\alpha T}. \qquad (8)$$

3.4.2.2 The indirect path

The method for retrieving the SW radiation budget applied in the indirect path is based on relating the shortwave (0.2 - 4.0 μm) transmittance, T (ratio of the irradiance at the surface to that at TOA), to the broadband TOA albedo, R (ratio of the reflected flux at TOA to the TOA irradiance). From the relationship $T = f(R)$, T can be computed by using R as determined from the satellite measured narrowband reflectance. Relationships of the type $T_i = f(R_i)$, $i = 1, \ldots, N$, representing N realistic atmospheric conditions are

established through radiative transfer computations of transmitted and reflected radiation, and stored in lookup tables (LUT) as described above. The retrieval process involves two inversion steps: (1) retrieving surface albedo, and (2) retrieving atmospheric transmittance and reflectance.

In the first step, clear sky atmospheric optical functions corresponding to the input gas amount and aerosol climatology are selected from the LUT. TOA albedo can thus be calculated when the surface albedo is known based on (Chandrasekhar, 1960):

$$R(\theta_0) = R^0(\theta_0) + r\tilde{T}$$

where

$$r = \left[1 - \alpha_{dif}(\theta_0)\tilde{R}\right]^{-1}\left[\alpha_{dir}(\theta_0)T^0_{dir}(\theta_0) + \alpha_{dif}(\theta_0)T^0_{dif}(\theta_0)\right] \quad (9)$$

$$\alpha_{dir}(\theta_0) = s * \alpha^{ref}_{dir}(\theta_0)$$

$$\alpha_{dif}(\theta_0) = s * \alpha^{ref}_{dif}(\theta_0)$$

Here, α_{dir} and α_{dif} are surface albedos to be retrieved for direct and diffuse irradiances, respectively. $\alpha^{ref}_{dir}(\theta_0)$ and $\alpha^{ref}_{dif}(\theta_0)$ are reference surface albedos corresponding to the identified IGBP surface type, and *s* is a scaling factor used to adjust the magnitude without changing the spectral shape. In this step, the clear sky atmospheric optical functions ($R^0(\theta_0), T^0(\theta_0), \tilde{T}, \tilde{R}$) correspond to the input gas amount and aerosol climatology, and are selected from the LUT. The retrieval of surface albedo is equivalent to finding the scaling factor *s* by using the clear-sky composite albedo as the TOA albedo in Eq. 9 (i.e., $R(\theta_0) = R_{comp}$), and it can be solved by (Pinker and Laszlo, 1992):

$$s = \frac{R_{comp} - R^0(\theta_0)}{\left[R_{comp} - R^0(\theta_0)\right]\alpha^{ref}_{dif}(\theta_0)\tilde{R} + \left[\alpha^{ref}_{dir}(\theta_0)T^0_{dir}(\theta_0) + \alpha^{ref}_{dif}(\theta_0)T^0_{dif}(\theta_0)\right]\tilde{T}} \quad (10)$$

When a non-physical surface albedo, i.e., less than zero or larger than unity in any spectral interval, is retrieved in this process, the algorithm uses the reference surface albedo instead, and the appropriate quality flag is set to indicate possible degradation of retrieval quality. Eq. 10 is also applied to the retrieval of snow/ice surface albedo with R_{comp} replaced by R^{snow}_{inst}, i.e. instantaneous TOA albedo for the clear-sky over snow/ice scene, and the snow/ice reference surface albedo is used correspondingly.

For determining the clear-sky composite albedo, the algorithm needs to keep track of the clear-sky snow/ice-free TOA albedo from the previous 28 days. For this, files are allocated to save the instantaneous clear-sky snow/ice-free TOA albedo converted from ABI reflectances. For each grid and time, the time series of albedos is stored as a queue with the oldest data removed as the most recent albedo is added. For cases when clear-sky snow/ice-free scene is not available, a missing value is used to update the queue. In the instantaneous indirect path retrieval, the previous 28 days clear-sky albedo

corresponding to the current processing grid and time is read into memory, the clear-sky composite albedo is then determined as the median value of this time series along with current clear-sky snow/ice-free TOA albedo. A standard procedure is implemented to determine the median value: First, the time series of valid (non-missing) clear-sky albedos is sorted in ascending order. If there are an odd number of elements, the middle one is taken. If the number of elements is an even number, the median value is calculated as the average of the middle pair. For the case where there is no valid clear-sky albedo available in the time series, the algorithm bypasses the surface albedo retrieval and uses the reference surface albedo in further processing. The appropriate quality flag is set for this case indicating the possible degradation of quality.

In the second retrieval step, atmospheric optical functions as a function of optical depth are selected from the LUT for the specified scene type. With the surface albedo retrieved in the previous step, the relationship, $T_i = f(R_i)$ can be established for various optical depth τ_i. Given the instantaneous TOA albedo R derived from the satellite measurement, optical depth τ, and corresponding atmospheric transmittance and reflectance, are determined. The details are provided in Pinker and Laszlo (1992). Essentially, in this process, the LUT is searched so that $R_i \le R < R_{i+1}$, and the values of the optical functions corresponding to R are obtained from the discrete values in the LUT by linear interpolation in $\log(\tau_i)$. Retrieval of the optical depth (aerosol or cloud) is determined within the limits of values given in the LUT (see Tables 3-7 and 3-8). When R is larger/smaller than the value calculated from the LUT with the minimum/maximum optical depth the minimum/maximum value is used as the retrieved value.

With the retrieved atmospheric optical functions and surface albedo the total reflectance and transmittance are calculated, similar to that used in the direct path, following Eqs. (3) and (4) with the parameter r from Eq. (9).

3.4.2.3 NTB and ADM conversions

The algorithm uses narrowband reflectances as inputs. These reflectances are expected to be calculated outside of the radiation budget algorithm using the expression:

$$\rho_{n,i} = \frac{\pi L_i(\vartheta_0, \varphi_0; \vartheta_S, \varphi_S)}{S_{0,i} \cos\vartheta_0 \frac{d_0^2}{d^2}}, i = \text{channels } 1,2,3,\ldots \qquad (11)$$

Here $\rho_{n,i}$ is the narrowband reflectance, the subscript i designates the ABI channels and subscript n indicates a "narrowband" quantity. L_i is the narrowband radiance, ϑ and φ are zenith and azimuth angles of the sun (subscript zero) and satellite (subscript S), respectively. $S_{0,\text{i}}$ is the extraterrestrial solar irradiance in the appropriate band at mean sun-earth distance, and d_0 and d are the mean and actual sun-earth distances.

The steps taken to convert the narrowband reflectances to a broadband albedo are as follows:

1. Convert $\rho_{n,i}$ into a broadband reflectance, ρ_b using narrow-to-broadband (NTB) conversion given in a polynomial form with coefficients, c_0 and $c_{i,j}$, where the index i representing the ABI channel runs from 1 to the maximum number of terms (currently 6):

$$\rho_b = c_0 + \sum_{i=1}^{m} c_i \rho_{n,i} \quad (12)$$

2. Apply the angular distribution model (ADM) to the broadband reflectance, ρ_b to get the broadband albedo, R:

$$R = \frac{\rho_b(\theta_0, \vartheta_S, \varphi)}{ADM(\theta_0, \vartheta_S, \varphi)} \quad (13)$$

where $\varphi = \varphi_0 - \varphi_S$ is the relative azimuth angle. The ADM is a set of anisotropic factors for determining the albedo from the observed bidirectional reflectance. It is defined in Eq. 14, where L is the broadband radiance:

$$ADM(\theta_0, \vartheta_S, \varphi) = \frac{\pi L(\theta_0, \vartheta_S, \varphi)}{M(\theta_0)} \quad (14)$$

and

$$M(\theta_0) = \int_0^{2\pi} \int_0^{\pi/2} L(\theta_0, \vartheta, \varphi) \cos\vartheta \sin\vartheta \, d\vartheta d\varphi . \quad (15)$$

The NTB equation implemented in the algorithm is quite general, as it can account for the dependence on solar and local zenith angle and relative azimuth angle. Separate coefficients can be provided for water and ice clouds, and as a function of surface type (water, land, desert, and snow/ice). Note, however, that the coefficients supplied for the MODIS proxy data do not currently have full angular dependence.

The coefficients c in Eq. 12 were derived by analyzing narrowband and broadband reflectances calculated from simulated narrowband and broadband radiances.

For the simulation of the narrowband and the broadband radiances the MODTRAN 3.7 radiative transfer model was used. The calculations had 33 layers in the vertical, with a spectral range from 0 to 50000 cm^{-1} and a maximum resolution of 50 cm^{-1}. MODTRAN

3.7 can calculate direct solar irradiance, single-scattered and multiple-scattered solar irradiance. Multiple scattering in MODTRAN 3.7 is calculated by calling the discrete ordinate code DISORT (Stamnes et al., 1988). In the simulations, 10 solar bins and 48 viewing bins (6 local zenith angles and 8 azimuth angles) are applied. The distributions of the Solar Zenith Angle (SZA), Local Zenith Angle (VZA), and Azimuth Angle (AZ), and all relevant inputs used in the MODTRAN 3.7 simulations are shown in Table 3-7.

The output from these simulations is the spectral radiance at the top of the atmosphere. The TOA narrowband and broadband reflectances are calculated from the spectral radiance (*L*) simulated from MODTRAN 3.7 within the wavelength range of λ_1 and λ_2, and the response function of the satellite sensor (*G*) :

$$\rho_n(\theta_0,\theta,\phi) = \frac{\pi \int_{\lambda_1}^{\lambda_2} L(\lambda,\theta_0,\theta,\phi)G(\lambda)d\lambda}{\int_{\lambda_1}^{\lambda_2} \cos(\theta_0)S_0(\lambda)G(\lambda)d\lambda} \tag{16}$$

$$\rho_b(\theta_0,\theta,\phi) = \frac{\pi \int_{0.2\mu m}^{4\mu m} L(\lambda,\theta_0,\theta,\phi)d\lambda}{\int_{0.2\mu m}^{4\mu m} \cos(\theta_0)S_0(\lambda)d\lambda} \tag{17}$$

.
The process for establishing NTB conversion entails the derivation of equations for estimating the broadband reflectance from linear or quadratic narrowband reflectance(s). The first step in this process relates to the selection of the appropriate channels to derive the multiple regression equations for different satellite sensors. For this the Residual Standard Deviation for different combinations of channels is used. The Residual Standard Deviation is defined as:

$$Error = \sqrt{\frac{\sum(\rho_b - \rho_b^{reg})^2}{N-2}} \tag{18}$$

where ρ_b is the "true" broadband reflectance obtained from integration of the radiances; ρ_b^{reg} is the broadband reflectance obtained from the regression equation; and *N* is the sample size. The technique has been used to select the "best" channel combinations. (Details are in Appendix A.)

The current version 5 of the algorithm implements the NTB coefficients developed for MODIS, and uses five channels as:

$$\rho_b = c_0 + c_1\rho_{0.47\mu m} + c_2\rho_{0.64\mu m} + c_3\rho_{0.85\mu m} + c_4\rho_{1.64\mu m} + c_5\rho_{2.13\mu m}$$

The solar zenith angle and surface type dependence is incorporated in the clear-sky coefficients. There are ten solar zenith angle bins and twelve surface types as list in Table 3-7. For cloudy-sky, five sets of coefficients are developed: 1) water cloud 2) ice cloud over ocean 3) ice cloud over desert 4) ice cloud over shrub 5) ice cloud over snow/ice. These currently do not depend on angles. The complete set of NTB/ADM coefficients for ABI must be developed later when all needed information on the instrument (spectral response function) becomes available.

Theoretically, better results would be expected if the NTB conversion formulas are derived for every solar, view, and azimuth angular bin separately. In practice, fluxes computed with MODIS proxy data are in closer agreement with the observations when all local zenith and azimuth angles are combined and the regression coefficients are stratified by solar zenith alone. Therefore, for now, the NTB coefficients are only functions of the solar zenith angle.

A table of the full set of NTB coefficients would be too large to be included here; they are available in a separate file.

3.4.3 Algorithm Output

3.4.3.1 Products

All-sky downward SW radiation at surface (DSR), reflected SW radiation at TOA (RSR), and quality flag are the primary outputs from the algorithm. Overall quality flag indicates the retrieval is successful (0) or failed (1). The overall quality flag is set to 1 when the local zenith angle is larger than 70°; the retrieved DSR and RSR is beyond the required valid range (0-1500 W/m^2 for DSR, 0-1300 W/m^2 for RSR); or the failure of retrieval of certain scene type is identified. Table 3-10 lists the primary output data.

Table 3-10. Primary output data.

Parameters	Explanation
DSR	Downward Surface SW Radiation
RSR	Reflected TOA SW Radiation
Quality Flag	Good(0) or bad (1) retrieval

To meet the 60 minute refresh requirement, the DSR and RSR products only need to be run once every hour.

3.4.3.2 Diagnostic/Intermediate Information

Other than the primary outputs, there are certain internal retrieval results and detailed quality flags prepared for diagnosis. The internal retrieval products include clear-sky composite albedo, retrieved aerosol/cloud optical depths, SW fluxes for each individual

scene types and spectral bands, and detailed quality flags that specify the source and quality of inputs, success/failure of the retrieval and algorithm for each scene type, and possible degradation in the retrieval quality due to various reasons. Table 3-11Tables 3-11 to 3-14 list these outputs from the ABI SRB algorithm.

Table 3-11. Internal retrieval output data.

Parameters	Explanation
ClrCompAlb	Clear-sky composite albedo
RetOD	Retrieved aerosol and cloud optical depths
ScnFlux	SW fluxes (TOA downward, TOA upward, Surface Downward, Surface Upward, Surface Downward Diffuse) for each scene and spectral band
AllSkyFlux	All-sky SW broadband fluxes (TOA downward, TOA upward, Surface Downward, Surface Upward, Surface Downward Diffuse)

Table 3-12. Detailed quality flags - input.

Bit*	Quality Flag Name	Meaning	
		zero (default)	one
0	QC_INPUT_LON	Valid longitude	Invalid longitude
1	QC_INPUT_LAT	Valid latitude	Invalid latitude
2	QC_INPUT_ELEV	Valid surface elevation	Invalid surface elevation
3	QC_INPUT_DATE	Valid date	Invalid date
4	QC_INPUT_GMT	Valid time	Invalid time
5	QC_INPUT_SOLZEN	Valid solar zenith angle	Invalid solar zenith angle
6	QC_INPUT_SATZEN	Valid local zenith angle	Invalid local zenith angle
7	QC_INPUT_RELAZI	Valid relative azimuth angle	Invalid relative azimuth angle
8	QC_INPUT_TPW	Valid TPW	Invalid TPW
9		All from ABI	Not all from ABI
10		All from model	Not all from model
11	QC_INPUT_OZONE	Valid ozone input	Invalid ozone
12		All from ABI	Not all from ABI
13		All from model	Not all from model
14	QC_INPUT_SNOW	Valid snow mask	Invalid snow mask

* Start from the least significant bit

15		All from ABI	Not all from ABI
16		All from IMS	Not all from IMS
17	QC_INPUT_SFCALB	Valid (or not applicable) surface albedo for scene-type 1[$]	Invalid or missing surface albedo for scene-type 1
18		Valid (or not applicable) surface albedo for scene-type 2	Invalid or missing surface albedo for scene-type 2
19		Valid (or not applicable) surface albedo for scene-type 3	Invalid or missing surface albedo for scene-type 3
20		Valid (or not applicable) surface albedo for scene-type 4	Invalid or missing surface albedo for scene-type 4
21	QC_INPUT_SCNFRAC	Valid scene fraction	Invalid scene fraction
22	QC_INPUT_AOD	Valid (or not applicable) ABI aerosol optical depth at 550nm	Invalid or missing ABI aerosol optical depth at 550nm
23	QC_INPUT_SSA	Valid (or not applicable) ABI aerosol single scattering albedo	Invalid or missing ABI aerosol single scattering albedo
24	QC_INPUT_WCDOD	Valid (or not applicable) ABI visible water cloud optical depth	From climatology
25	QC_INPUT_WCDRDS	Valid (or not applicable) ABI water cloud particle radius	From climatology
26	QC_INPUT_WCDHGT	Valid (or not applicable) ABI water cloud top height	From climatology
27	QC_INPUT_ICDOD	Valid (or not applicable) ABI visible ice cloud optical depth	From climatology
28	QC_INPUT_ICDRDS	Valid (or not applicable) ABI ice cloud particle radius	From climatology
29	QC_INPUT_ICDHGT	Valid (or not applicable) ABI ice cloud top height	From climatology

$ There are four scene types for each 'block' retrieval: 1. clear-sky snow-free; 2. clear-sky over snow/ice; 3. water cloud; 4. ice cloud.

30	QC_INPUT_REFL	Valid ABI reflectance	Invalid ABI reflectance

* start from the least significant bit

$ scene type 1-4 correspond to clear-sky snow/ice-free; clear-sky over snow/ice; water cloud; ice cloud.

Table 3-13. Detailed quality flags – algorithm selection and performance.

Bit	Quality Flag Name	Meaning	
		zero (default)	one
0	QC_RET_OVERALL	Overall success of retrieval	Overall failure of retrieval
1	QC_RET_INPUT	No fatal error(s) in inputs	Retrieval failed due to invalid input
2	QC_RET_SCENE1	scene type 1 is available	no scene type 1 in block
3		Direct path is invoked for scene type 1	Indirect path is invoked for scene type 1
4		Direct path retrieval succeeded for scene type 1 (if it is invoked)	Direct path failed for scene type 1 because denominator is close to zero in flux calculation
5		TOA conversion succeeded in indirect path retrieval for scene type 1 (if it is invoked)	Indirect path failed for scene type 1 due to unsuccessful TOA conversion
6		Indirect path retrieval succeeded for scene type 1 (if it is invoked)	Indirect path failed for scene type 1 because denominator is close to zero in flux calculation
7	QC_RET_SCENE2	scene type 2 is available	no scene type 2 in block
8		Direct path is invoked for scene type 2	Indirect path is invoked for scene type 2
9		Direct path retrieval succeeded for scene type 2 (if it is invoked)	Direct path failed for scene type 2 because denominator is close to zero in flux calculation
10		TOA conversion succeeded in indirect path retrieval for scene type 2 (if it is invoked)	Indirect path failed for scene type 2 due to unsuccessful TOA conversion
11		Indirect path retrieval succeeded for scene type 2	Indirect path failed for scene type 2 because denominator

		(if it is invoked)	is close to zero in flux calculation
12	QC_RET_SCENE3	scene type 3 is available	no scene type 3 in block
13		Direct path is invoked for scene type 3	Indirect path is invoked for scene type 3
14		Direct path retrieval succeeded for scene type 3 (if it is invoked)	Direct path failed for scene type 3 because denominator is close to zero in flux calculation
15		TOA conversion succeeded in indirect path retrieval for scene type 3 (if it is invoked)	Indirect path failed for scene type 3 due to unsuccessful TOA conversion
16		Indirect path retrieval succeeded for scene type 3 (if it is invoked)	Indirect path failed for scene type 3 because denominator is close to zero in flux calculation
17	QC_RET_SCENE4	scene type 4 is available	no scene type 4 in block
18		Direct path is invoked for scene type 4	Indirect path is invoked for scene type 4
19		Direct path retrieval succeeded for scene type 4 (if it is invoked)	Direct path failed for scene type 4 because denominator is close to zero in flux calculation
20		TOA conversion succeeded in indirect path retrieval for scene type 4 (if it is invoked)	Indirect path failed for scene type 4 due to unsuccessful TOA conversion
21		Indirect path retrieval succeeded for scene type 4 (if it is invoked)	Indirect path failed for scene type 4 because denominator is close to zero in flux calculation

Table 3-14. Detailed quality flags – factors degrading the retrieval quality.

Bit	**Quality Flag Name**	**Meaning**	
		zero (default)	**one**
0	QC_LOWSUN	Solar zenith angle is not larger than 70 degrees	Solar zenith angle is larger than 70 degrees
1	QC_LOWSAT	Local zenith angle is not	Local zenith angle is larger

		larger than 70 degrees	than 70 degree
2	QC_SNOWICE	No snow/ice is in the block	snow/ice present
3	QC_COAST	Not in coastal region	Coastal region
4	QC_POLAR_NIGHT	Not polar night	Polar night
5	QC_CLR_CMPT	Estimation of clear-sky composite reflectance succeeded	Estimation of clear-sky composite reflectance failed
6		TOA conversion of narrowband composite reflectance to broadband albedo succeeded	TOA conversion of narrowband composite reflectance to broadband albedo failed
7	QC_SFCALB	Scaling reference surface albedo succeeded in indirect path (if it is invoked)	Scaling reference surface albedo failed in indirect path
8		Scaling snow/ice surface albedo succeeded in indirect path (if it is invoked)	Scaling snow/ice surface albedo failed in indirect path
9	QC_TOA_MATCH	Matching with TOA albedo succeeded for scene type 1 in indirect path (if it is invoked)	Matching with TOA albedo failed for scene type 1 in indirect path
10		Matching with TOA albedo succeeded for scene type 2 in indirect path (if it is invoked)	Matching with TOA albedo failed for scene type 2 in indirect path
11		Matching with TOA albedo succeeded for scene type 3 in indirect path (if it is invoked)	Matching with TOA albedo failed for scene type 3 in indirect path
12		Matching with TOA albedo succeeded for scene type 4 in indirect path (if it is invoked)	Matching with TOA albedo failed for scene type 4 in indirect path

3.4.3.3 Metadata

In addition the following metadata information is included in the output:

- Min, Max, Mean, Std Deviation of surface downward flux

- Min, Max, Mean, Std Deviation of atmosphere top upward flux
- Min, Max, Mean, Std Deviation of solar zenith angle
- Mean total cloud fraction
- Number of QA flag values
- For each QA flag value
  - Percent of retrievals with the QA flag value
  - Definition of QA flag
- Total number of pixels where retrieval was attempted
- Number of pixels with local zenith angle less than 70 degrees

4 Test Data Sets and Outputs

4.1 Simulated/Proxy Input Data Sets

This section describes the test data sets used to characterize the performance of the algorithm and quality of the data product(s), including the breadth of the domain (typical versus stressing states) used in the analysis and assessment.

As described below, the data used to test the ABI SRB algorithm included SEVIRI and MODIS observations. Four months worth of data are chosen from SEVIRI observations during January, April, July and October of year 2006. MODIS data (from both Terra and Aqua) used for testing the SRB algorithm are from March 2000 to December 2009 collocated with 12 ground stations from the Surface Radiation Budget Network (SURFRAD) and the Climate Monitoring and Diagnostics Laboratory (CMDL) surface radiation monitoring project.

4.1.1 SEVIRI Data

SEVIRI observations from two SW channels (0.63 and 0.86 μm) with a spatial resolution of 3 km and a temporal resolution of 1 hour are used for testing the SRB algorithm. SEVIRI provides the best source of data currently for testing the ABI SRB algorithm over the whole diurnal cycle. Image-based SEVIRI cloud mask in full pixel resolution products are taken from the European Organisation for the Exploitation of Meteorological Satellites (EUMETSAT) (http://archive.eumetsat.org/umarf). Snow detection follows the threshold tests of the ABI Snow Cover and Snow Depth algorithm. To approximate the horizontal spatial resolution of the ABI radiation products, pixel-level SEVIRI data were averaged into ½ degree equal-angle grids. A simple arithmetic averaging was used. Grouping and averaging of SW reflectance was carried out separately for clear and cloudy scenes; averaging followed grouping. No information on cloud type and height was available, so there was no stratification based on cloud type, height or thickness. Figure 4-1 shows a full-disk SEVIRI image from 12 Z on April 15, 2006.

Validation of retrieved DSR relied upon the measurements from the Baseline Surface Radiation Network (BSRN). A 30-minute temporal averaging was applied to the BSRN observations to match point measurements with grid retrievals. Altogether, there were 10,630 pairs of collocated retrievals and measurements found from nine stations shown in Table 4-1.

Validation of retrieved RSR is achieved by comparing it to the measurements from the Geostationary Earth Radiation Budget (GERB) instrument. GERB measurements are made every 17 minutes with a nadir footprint size of 45 x 40 km (Harries et al., 2005). Derived reflected solar flux is estimated to be ~7% higher than the CERES products (Russell, 2006). Validation is performed with the temporally closest GERB measurement without interpolation in time.

Table 4-1. BSRN stations used for validating retrieved DSR from SEVIRI proxy data

Station Label	Station Name	Latitude	Longitude	Elevation [m]
BER	Bermuda	32.267	-64.667	8
CAB	Cabauw, Netherlands	51.971	4.9267	0
CAR	Carpentras, France	44.083	5.059	100
LER	Lerwick, UK	60.1333	-1.1833	84
PAL	Palaiseau Cedex, France	48.713	2.208	156
PAY	Payerne, Switzerland	46.820	6.93	491
SBO	Sede Boqer, Isreal	30.905	34.782	500
TAM	Tamanrasset, Algeria	22.780	5.51	1385
TOR	Toravere, Estonia	58.254	26.462	70

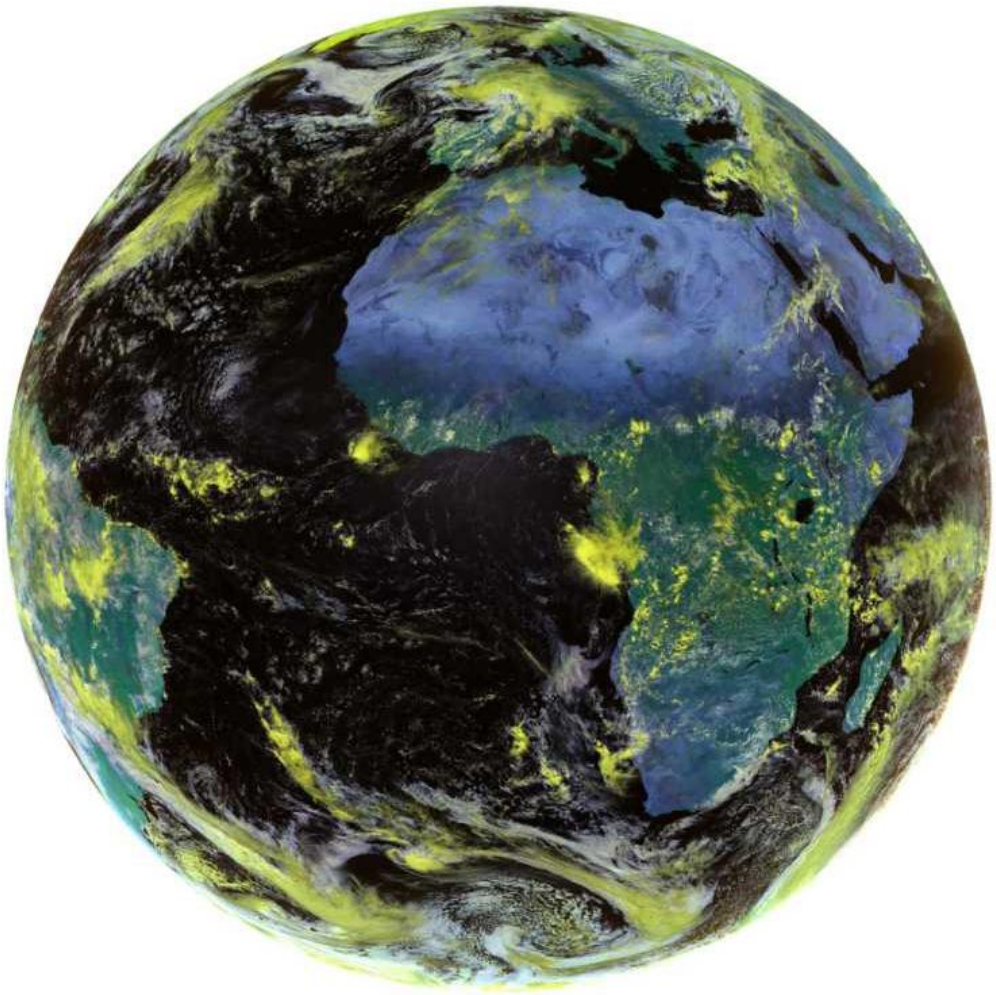

Figure 4-1. Fulldisk 0.63, 0.86 and 1.67 μm false color image from SEVIRI for 12 UTC on April 15, 2006.

4.1.2 MODIS Data

MODIS proxy data used for testing the ABI SRB algorithm include L1B SW narrowband reflectances at 1km resolution; Level 2 products of aerosol optical depth; cloud optical depth, size, phase, height; total precipitable water, ozone; cloud and snow mask and surface albedo. Data within 50, 25 and 5 km square regions centered on 12 ground stations (Table 4-2) are averaged. Retrieved DSR is compared with ground flux measurements, while validation of RSR is performed by comparing with CERES TOA upward SW flux. Table 4-3 lists the mapping between the ABI and MODIS channels.

Table 4-2. Ground stations used for validating retrieved DSR from MODIS proxy data

Station Label	Station Name	Network	Latitude	Longitude	Elevation [m]
BON	Bondville, IL	SURFRAD	40.05	-88.37	213

DRA	Desert Rock, NV	SURFRAD	36.63	-116.02	1007
FPK	Fort Peck, MT	SURFRAD	48.31	-105.10	634
GWN	Goodwin Creek, MS	SURFRAD	34.25	-89.87	98
PSU	Penn State, PA	SURFRAD	40.72	-77.93	376
SXF	Sioux Falls, SD	SURFRAD	43.73	-96.62	473
TBL	Table Mountain, CO	SURFRAD	40.13	-105.24	1689
COV	Chesapeake Bay Light Tower, MD	COVE	36.90	-75.71	30
E13	Lamont, OK	ARM	36.61	-97.48	318
BER	Bermuda	CMDL	32.30	-64.77	60
BOU	Boulder Tower, CO	CMDL	40.05	-105.01	1584
KWA	Kwajalein, RMI	CMDL	8.76	167.72	10

Table 4-3. MODIS Visible and NIR channels and the corresponding channels of ABI.

ABI Channel number	*Spectral band (*μm*)*	
	ABI	*MODIS*
1	0.590-0.690	0.620-0.670
2	0.846-0.885	0.841-0.876
3	0.450-0.490	0.459-0.479
4	1.371-1.386	1.360-1.390
5	1.580-1.640	1.628-1.652
6	2.225-2.275	2.105-2.155

4.2 Output from Simulated/Proxy Inputs Data Sets

Full disk DSR and RSR are retrieved from ABI SRB algorithm for the entire 4 months of evaluation with SEVIRI data. Figure 4-2 shows the retrieved DSR and RSR for 12:00 UTC on April 15, 2006, corresponding to the false color image shown in Figure 4-1. Ground and TOA measurements from BSRN and GERB are then applied to the retrieval results and used to generate the performance estimates provided below. DSR and RSR retrieved from MODIS proxy data over 13 stations are also available for the evaluation with ground observations and TOA CERES measurements.

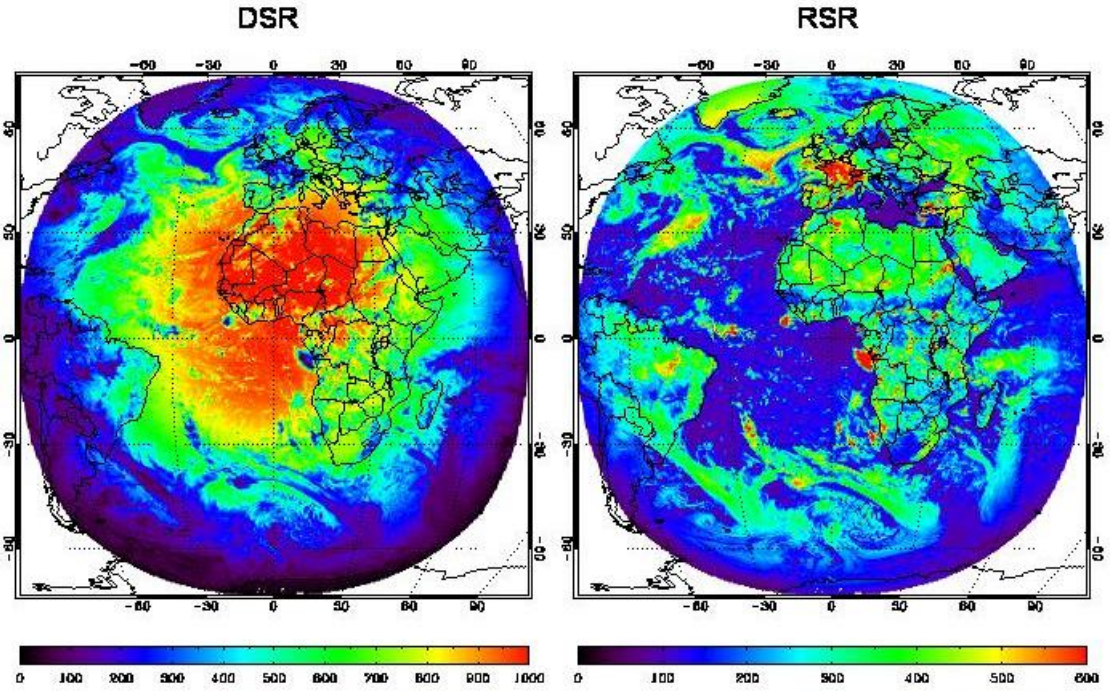

Figure 4-2. Retrieved full-disk DSR and RSR (W/m^2) from SEVIRI for 12 UTC on April 15, 2006.

4.2.1 Precision and Accuracy Estimates

This section describes the predicted algorithm performance and quality of the products at a level of detail appropriate for the current algorithm maturity given instrument performance is as required.

Evaluation of the DSR and RSR products retrieved from the ABI SRB algorithm is performed by comparison with various ground and TOA measurements. Following the F&PS definition, bias and one-sigma standard deviation are calculated for all retrievals to assess the retrieval accuracy and precision.

The performance of the direct path retrieval is predominantly determined by the uncertainty of the input ABI products. Thus it is anticipated that low quality of DSR and RSR would be associated with conditions unfavorable for the cloud, aerosol and surface albedo retrievals, such as over cold bright surface, oblique viewing geometry, and coastal regions, etc. For the indirect path, retrieval performance is influenced by the uncertainties associated with the NTB conversion and angular correction, as well as ancillary inputs of cloud fraction, clear-sky composite reflectance, aerosol climatology and reference surface albedo, etc. It is noted that differences in observing geometry and spatial scales of satellite retrievals and ground/TOA observations can make the validation difficult.

The evaluation of retrievals from SEVIRI data for four months (Figure 4-3) shows the overall accuracy of retrieved DSR and RSR is within 2% and 4%, and overall precision is estimated to be 24% and 22%. Large errors appear at extreme (low and high) value ends.

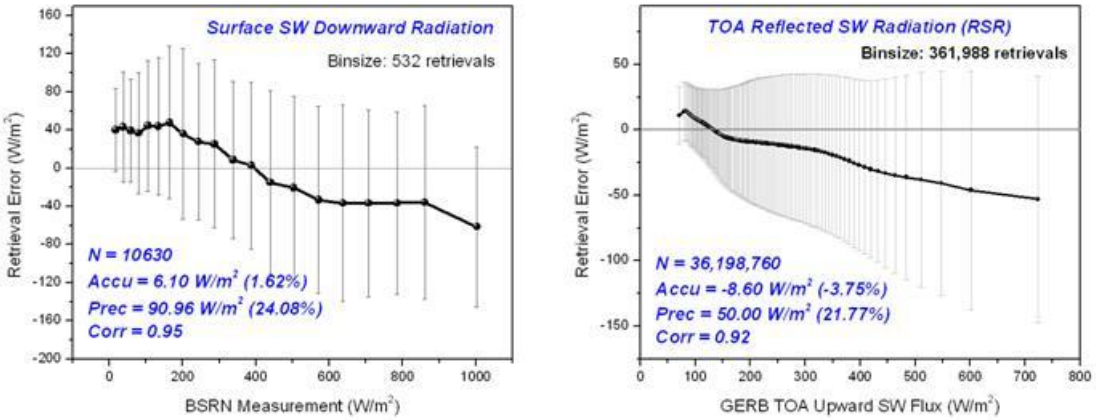

Figure 4-3. Error of DSR (left) and RSR (right) retrieved from SEVIRI proxy data as a function of ground and GERB measurements. Vertical bar represents the standard deviation of retrieval errors within each bin.

More extensive validation is performed with 10-year worth of MODIS proxy data. Figure 4-4 shows the retrieved DSR and RSR errors as a function of measurement. The overall DSR accuracy is about 2% and precision is about 20% for three spatial resolutions (50, 25 and 5 km) without significant spatial scale dependence. Accuracy and precision of retrieved RSR is about 7% and 20% for the 25-km retrievals. Among all retrievals, the indirect path is used in ~65% of clear-sky cases and in ~50% of cloudy scenes.

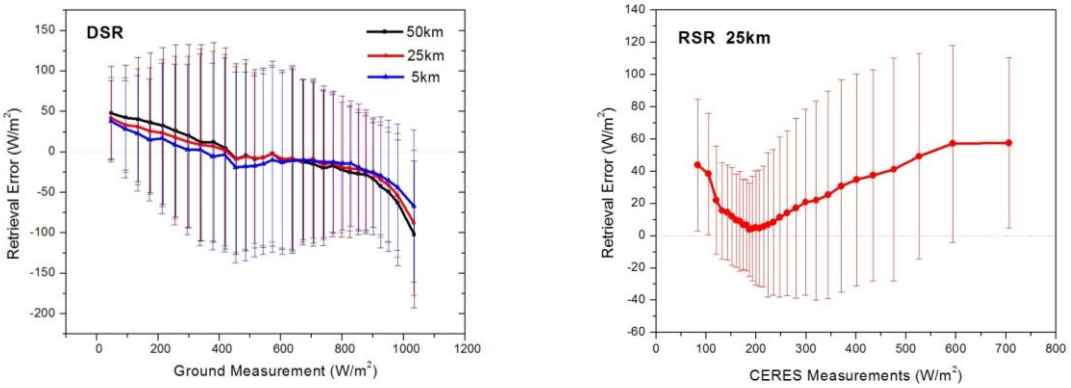

Figure 4-4. Error of DSR (left) and RSR (right) retrieved from MODIS proxy data as a function of ground and CERES measurements. Vertical bar represents the standard deviation of retrieval errors within each bin. DSR retrievals are evaluated at 50/25/5-km resolutions, RSR retrievals are validated at the 25-km resolution.

A separate evaluation of direct and indirect path retrievals with 25-km MODIS proxy data is presented in Figure 4-5. The larger error at the extreme value ends is a common feature of both paths. Compared with the direct path retrievals, the indirect path has a lower overall bias for RSR, while exhibits lower precision for both DSR and RSR retrievals.

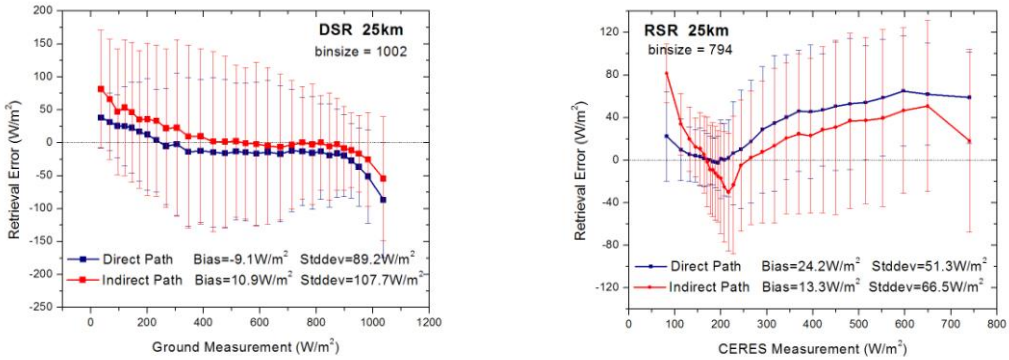

Figure 4-5. Error of DSR (left) and RSR (right) retrieved from the direct and indirect paths as a function of ground and CERES measurements. 25-km MODIS proxy data are used as input.

The dependence of DSR and RSR retrievals on cloud fraction is displayed in Figure 4-6. Clear and overcast cases account for the majority of retrievals. For the DSR retrievals, there is no obvious cloud fraction dependence for either path, while positive/negative biases are associated with indirect/direct path retrievals under overcast conditions. For RSR retrievals, both paths exhibit an increase of error as the cloud fraction increases and positive biases are associated with overcast cases.

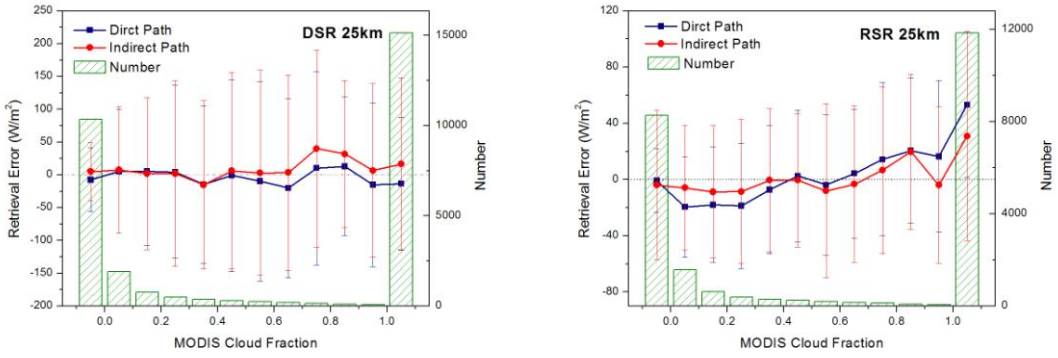

Figure 4-6. Error of DSR (left) and RSR (right) retrieved from the direct and indirect paths as a function of cloud fraction. 25-km MODIS proxy data are used as input.

The dependence of DSR and RSR retrievals on solar zenith angle is shown in Figure 4-7. For DSR, relatively large error appears at the low and high solar zenith angle ends. There is no significant angular dependence of the RSR retrieval.

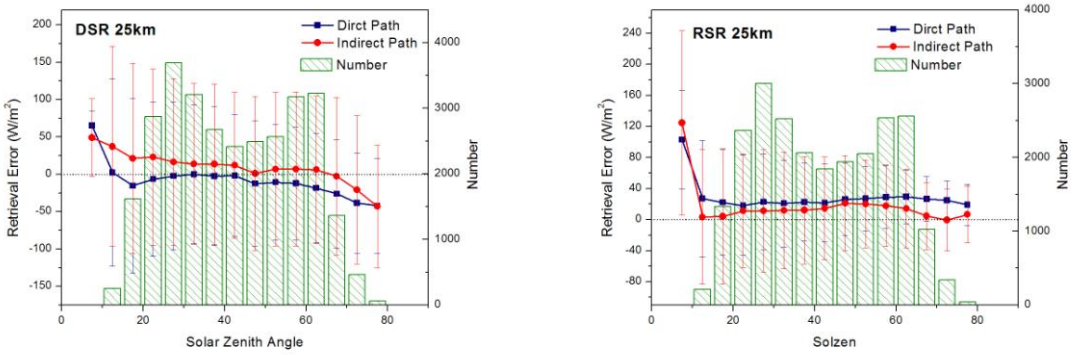

Figure 4-7. Error of DSR (left) and RSR (right) retrieved from direct and indirect paths as a function of cloud fraction. 25-km MODIS proxy data are used as input.

4.2.2 Error Budget

Accuracy and precision of DSR and RSR are estimated for retrievals with MODIS proxy data for three ranges according to the F&PS specification. Tables 4-3 to 4-6 list the validation results as well as the F&PS requirements.

Current validation with MODIS data demonstrates that the performance of ABI SRB algorithm satisfies the 100% requirements. It should be noted that, given the wide range of DSR and RSR values, assessment of performance depends on the validation samples from which the statistics are derived. Validation performed at different locations, distinct diurnal phase or using retrieval inputs from different sources could generate different accuracy and precision values for the same algorithm.

Table 4-4 Accuracy of DSR retrieved from MODIS proxy data.

DSR Measurement (W/m^2)	F&PS Requirement (W/m^2)	Validation with MODIS		
		50km	25km	5km
Low (<200)	±110	42	33	26
Middle (200-500)	±65	11	7	-2
High (>500)	±85	-27	-23	-21

Table 4-5 Precision of DSR retrieved from MODIS proxy data.

DSR	F&PS	Validation with MODIS

Measurement (W/m^2)	Requirement (W/m^2)	50km	25km	5km
Low (<200)	100	73	67	67
Middle (200-500)	130	116	111	112
High (>500)	100	96	93	94

Table 4-6 Accuracy of RSR retrieved from MODIS proxy data.

RSR Measurement (W/m^2)	F&PS Requirement	Validation with MODIS (25km)
Low (<200)	±110	15
Middle (200-500)	±65	20
High (>500)	±85	55

Table 4-7 Precision of RSR retrieved from MODIS proxy data.

RSR Measurement (W/m^2)	F&PS Requirement	Validation with MODIS (25km)
Low (<200)	100	34
Middle (200-500)	130	57
High (>500)	100	60

To evaluate the sensitivity of the hybrid algorithm to input uncertainties, sensitivity tests are designed to perturb the inputs with anticipated errors. In order to perform such tests under realistic scenarios, 10-year worth of 25-km MODIS proxy data are purposely modified. Specifically, total precipitable water is changed by ±10%; column ozone by ±10%; aerosol optical depth by ±30%; cloud optical depth by ±20%; cloud height by ±0.5km; water/ice cloud radius by ±4/10μm; cloud fraction by 10%; and channel reflectance by ±3%. Table 4-8 presents the difference between retrievals with/without each input perturbation. It shows that the all-sky hybrid retrievals are less sensitive to the uncertainties associated with cloud height, total precipitable water and ozone amount. 30% uncertainty in the aerosol optical depth does not exert significant influence on the all-sky DSR/RSR retrievals (<1%) although its impact could be large for clear scenes. 20% variation of cloud optical depth leads to less than 5% change in the retrieval. Uncertainty in cloud particle size has more impact on RSR than the DSR retrieval. 3% calibration uncertainties will affect the indirect path retrieval by the similar fraction due to the linear transformation of reflectance to albedo. The largest impact comes from the cloud fraction uncertainty owing to the significant effects of clouds on DSR/RSR.

Table 4-8. Sensitivity test results. - Difference between retrievals with and without perturbation of the input 25-km MODIS proxy data.

Sensitivity Test	DSR		RSR	
	Bias (W/m^2)	StdDev (W/m^2)	Bias (W/m^2)	StdDev (W/m^2)
TPW +10%	-2.78 (-0.5%)	1.71 (0.3%)	-0.62 (-0.2%)	0.54 (0.2%)
TPW -10%	2.98 (0.5%)	2.21 (0.4%)	0.67 (0.2%)	0.98 (0.3%)
Ozone +10%	-0.96 (-0.2%)	0.47 (0.1%)	-0.77 (-0.3%)	0.63 (0.2%)
Ozone -10%	0.97 (0.2%)	1.47 (0.3%)	0.79 (0.3%)	0.91 (0.3%)
Aerosol Optical Depth +30%	-4.89 (-0.7%)	6.18 (0.9%)	1.05 (0.5%)	2.71 (1.2%)
Aerosol Optical Depth -30%	5.01 (0.7%)	6.65 (1.0%)	-1.05 (-0.5%)	2.83 (1.3%)
Cloud Optical Depth +20%	-16.19 (-3.4%)	13.09 (2.8%)	12.65 (3.6%)	10.72 (3.0%)
Cloud Optical Depth -20%	19.77 (4.2%)	16.07 (3.4%)	-15.44 (-4.4%)	13.20 (3.7%)
Cloud Height +0.5km	0.00 (0.0%)	0.001 (0.0%)	0.002 (0.0%)	0.002 (0.0%)
Cloud Height -0.5km	-0.00 (-0.0%)	0.001 (0.0%)	-0.002 (-0.0%)	0.002 (0.0%)
Water/Ice Cloud Radius +4/10 μm	2.30 (0.5%)	3.33 (0.7%)	-6.54 (-1.9%)	6.62 (1.9%)
Water/Ice Cloud Radius -4/10 μm	-2.00 (0.5%)	3.10 (0.6%)	5.69 (1.7%)	6.35 (1.8%)
Cloud Fraction +10%	-42.20 (-5.9%)	36.95 (5.1%)	-1.89 (-1.0%)	15.28 (7.8%)
Channel Reflectance +3%	-11.93 (-2.2%)	8.36 (1.5%)	7.84 (2.6%)	6.06 (2.0%)
Channel Reflectance -3%	12.09 (2.3%)	8.50 (1.6%)	-8.07 (-2.6%)	6.09 (2.0%)

In addition to the performance estimates shown above, analysis of diurnal and seasonal dependences of errors is also important to fully characterize the product. However, the MODIS and CERES proxy data used do not allow a good characterization of diurnal errors (although they do represent a fairly large range of solar elevations). A more extensive evaluation has been outlined in the Algorithm Validation and Test Plan. The

results of this analysis (including diurnal and seasonal dependence of errors) will go in the Validation Document.

The analysis of results obtained using the MODIS and CERES proxy data indicates that large precision values (standard deviation) are the results of the spatial-temporal incompatibility of satellite-derived and ground observed fluxes. The former corresponds to and represents conditions in an atmospheric column with finite, horizontal-resolution dependent base, while the latter responds to conditions from the entire hemisphere as seen from a single point. This is an age-old problem. The usual technique to deal with this is to invoke a form of the ergodic hypothesis and to spatially average the satellite estimates and temporally average the ground measurements (e.g., Pinker and Laszlo, 1992). The appropriate temporal and spatial scales for this vary from location to location; but more importantly, they are not known a priori.

Analysis of the spatial-scale dependence of the errors is also desirable. However, it should be noted that performing the analysis on various spatial scales introduces differences between satellite-derived and ground-derived fluxes that have nothing to do with the performance of the algorithm; rather, the issue is that a single ground station may not provide a true representation of the flux at that spatial scale. This is especially true for very small (<~10 km) and large (>~100 km) scales.

5 Practical Considerations

5.1 Numerical Computation Considerations

Solution of the radiative transfer is represented in LUT. The LUT approach uses pre-calculated values of spectral atmospheric transmittances, reflectances, spherical transmittance and albedo. This makes calculations relatively fast.

5.2 Programming and Procedural Considerations

The retrieval is carried out on a grid scale, and all inputs should be consistent with the same spatial resolution. The algorithm requires calibrated and geo-located ABI reflectances, ABI cloud mask and snow/ice mask, water vapor and ozone amount; aerosol and cloud products and SW surface albedo as ABI inputs. Arithmetic averaging of pixel-level ABI products is performed within the predefined spatial grids. For the aerosol and cloud optical depth, averaging is carried out in the log scale to preserve the albedo. Mapping processes for static ancillary (e.g. surface elevation, surface type) can be processed offline. The programming design uses modules, providing the flexibility for ease upgrades.

To facilitate the determination of clear-sky composite albedo, instantaneous clear-sky snow/ice-free albedo from the previous 29 days is saved in a local file for each grid and individual observation time. Such time series of clear-sky albedo is implemented as a

queue, i.e., the oldest data is removed when the most recent albedo is added. In the instantaneous indirect path retrieval, the previous 29 days clear-sky albedo corresponding to the current processing grid/time is read into memory, clear-sky composite albedo is determined as the median value of this time series along with the current clear-sky albedo (if it is available). Update of the historical clear-sky albedo is not performed when the clear-sky snow/ice-free scene is absent in the current retrieval (due to overcast condition or snow/ice coverage).

For efficient processing, lookup tables and coefficients need to be constrained to a manageable size. Therefore, atmospheric reflectivity and transmissivity and TOA conversion coefficients are calculated only for discrete values of atmospheric parameters, geometry angles, and surface elevation, and interpolation is applied to derive the atmospheric optical functions and coefficients corresponding to the instantaneous condition. In the SRB algorithm, quantities in the LUT and coefficients are linearly interpolated as follows:

A straight line is assumed between two points given by the coordinates (x_0,y_0) and (x_1,y_1). These two points can represent any two parameters in the LUT, for example. For a value x in the interval (x_0,x_1), the corresponding value y is calculated as:

$$y = y_0 + (x - x_0)\frac{y_1 - y_0}{x_1 - x_0}$$

Here, the point (x, y) represents a specific value of the dependent variable and the associated atmospheric optical function.

For more than one dependent variables, i.e., $y=f(x_1,x_2,\ldots,x_n)$, the linear interpolation is repeated for n variables that have been tabulated at the nodes of an n-dimensional rectangular grid. For example, for a 2-dimensional case with two dependent variables x_1 and x_2, the interpolation procedure is equivalent to the following:

Let $a_1,a_2,\ldots$ be the tabulated values of dependent variable a and let $b_1,b_2,\ldots$ be the tabulated values of dependent variable b. Let i, j be the subscripts for which $a_i \le a \le a_{i+1}$, $b_j \le b \le b_{j+1}$. Then compute:

$t = (a - a_i) / (a_{i+1} - a_i)$
$g_j = (1 - t)*f(a_i,b_j) + t*f(a_{i+1}, b_j)$
$g_{j+1} = (1 - t)*f(a_i,b_{j+1}) + t*f(a_{i+1}, b_{j+1})$
$u = (b - b_j) / (b_{j+1} - b_j)$
$y = (1 - t) *g_j + t*g_{j+1}$

5.3 Quality Assessment and Diagnostics

The following procedures are used for diagnosing the performance:

- Monitor the percentage of daytime pixels with valid retrievals. This number is compared to the "astronomically" possible value.
- Flag retrievals done with direct and indirect path.

- Flag any situation which might degrade the retrieval quality (retrieval over unfavorable environmental condition; using climatology due to missing input; internal retrieval falls out of LUT range; etc)
- Evaluate individual quality flag and assess the overall quality.

.

5.4 Exception Handling

The SW RB algorithm checks the validity of each input and situations causing the unintentional abort of the retrieval. List of exceptions is shown in Table 5-1.

Table 5-1 Exceptions handled in algorithm

Exception	Detection	Handling
Invalid Input	Inputs out of valid range	No retrieval
Low solar position	SZA > 70^o	Degrade the quality flag
Snow/ice present	Snow fraction > 0	Degrade the quality flag
Coastal region	Checking coast mask	Degrade the quality flag
Missing water vapor input	Input set as missing	Replaced with climatology
Missing column ozone input	Input set as missing	Replaced with climatology
Missing water cloud optical depth input	Input set as missing	Replaced with climatology, retrieval with indirect path
Missing water cloud radius input	Input set as missing	Replaced with climatology, retrieval with indirect path
Missing water cloud height input	Input set as missing	Replaced with climatology, retrieval with indirect path
Missing ice cloud optical depth input	Input set as missing	Replaced with climatology, retrieval with indirect path
Missing ice cloud radius input	Input set as missing	Replaced with climatology, retrieval with indirect path
Missing ice cloud height input	Input set as missing	Replaced with climatology, retrieval with indirect path
Direct path retrieval failed	Illegal numerical computation	Quit retrieval
Indirect path retrieval failed	Illegal numerical computation	Quit retrieval
Polar night	Checking time and location	Quit retrieval
Unable to derive clear-sky composite albedo	Indirect path	Quit retrieval
Unable to scale reference spectral surface albedo	Indirect path	Replaced with reference surface albedo, Degrade the quality flag
Unable to convert reflectances to TOA albedo	Indirect path	Quit retrieval
Unable to match TOA	Indirect path	Using the Min/Max aerosol

albedo for clear scene		optical depth in LUT, Degrade the quality flag
Unable to match TOA albedo for water cloud scene	Indirect path	Using the Min/Max water cloud optical depth in LUT, Degrade the quality flag
Unable to match TOA albedo for water cloud scene	Indirect path	Using the Min/Max water ice optical depth in LUT, Degrade the quality flag
Unable to calculate flux	Illegal numerical computation	Quit retrieval

5.5 Algorithm Validation

5.5.1 Pre-Launch Phase Activities

During the pre-launch phase of the GOES-R program, validation of ABI SRB algorithm has three stages. First, the two components of the ABI SW RB algorithm (the direct and the indirect paths) are evaluated independently (as separate algorithms) with independent data. The data sets used in this stage represent different time periods and come from different sources. Next, the evaluation of the two –still independent- paths is performed with common data that supply the input needed for both the direct and indirect paths. In the third stage the combined algorithm is tested with the data set used in the second stage. This stage tests the implementation of the combined algorithm with the expectation that the statistics will be similar to those obtained in the second stage. All three stages have been executed during the algorithm development and results from these are presented in the previous sections. Continued, more detailed evaluation of the algorithm is important and it is done in the coming years. The data sets used in this stage are described below.

5.5.1.1 Proxy and Simulated Instrument Data

Ideally, the following proxy data should be used for algorithm development and testing during the pre-launch phase:

- A minimum of 29 full daytime sets of hourly SEVIRI images and GERB TOA fluxes per month for four seasonal months collected for the month before the month being analyzed for the creation of clear composite field for the indirect path.
- Four seasonal months of CERES ARM Validation Experiment (CAVE) data with satellite-derived TOA CERES fluxes. The CAVE data also include the reference data in the form of ground-measurements of surface broadband downward flux from ARM, BSRN, SURFRAD, and CMDL.
- Four seasonal months of MODIS radiances for at least 10 MODIS granules and corresponding CERES TOA fluxes. The selected MODIS granules include at least one surface (CAVE) site.

- Four sets of model simulated ABI proxy data for 29 full daytime hours representing the four seasons. The 29-day requirement is imposed upon by the indirect path that uses the consecutive images from 29 days to establish a clear-composite field corresponding to the clearest scenes for each pixel.

5.5.1.2 Algorithm Evaluation and Characterization

The SW surface downward and TOA upward fluxes derived by the ABI algorithm are subject to systematic and random errors arising from two fundamental sources: the algorithm itself and the data input into the algorithm. Errors associated with the algorithm come from simplified treatments of the radiative transfer process, inherent deficiency of any parameterization schemes and imperfect TOA narrow-band radiance to broad-band flux conversion. Errors associated with input data include the inaccurate atmosphere and surface properties derived from upstream ABI retrievals, as well as the quality of calibration and ancillary data. The diversity of error sources necessitates the determination of not only the magnitude of the error but also its origin. Identifying the error sources allows for continual improvement in the accuracy of the algorithm. In this regard, the reference data that should be collected include not only those parameters requested by the GOES-R Specification Documents (MRD, F&PS) but also those internal correlative parameters that have potential impact on the retrieval. Since the full range of evaluation cannot be carried out until the GOSE-R ABI instrument becomes operational, the pre-launch validation phase will emphasize the characterization and documentation of the uncertainties under diverse conditions as well as the validation tool development to diagnose algorithmic implementation artifacts.

Characterization of the performance of ABI SW RB products can be made by the direct comparison between retrieved and reference SW fluxes. In the case of the synthetic proxy data, the reference data of SW surface downward and TOA reflected fluxes can be readily achieved from a detailed radiative transfer calculation with the modeled meteorological data. In the case of real satellite data, the validation effort depends upon the acquisition of ground data from field campaigns such as the ARM (Atmospheric Radiation Measurement) and from operational surface networks such as the NOAA Surface Radiation (SURFRAD) program and the World Climate Research Program (WCRP) Baseline Surface Radiation Network (BSRN), as well as the TOA SW reflected flux (derived from measured SW radiance using suitably validated angular distribution models) from satellite instruments such as Cloud and the Earth's Radiant Energy System (CERES).

Throughout the algorithm development phase ground-based data from the NOAA SURFRAD in the CONUS and other ESRL/GMD sites outside CONUS but within the full-disk view have been available for testing and evaluation of algorithms.

The ABI SW RB products will be considered validated if the overall accuracy and precision satisfy the requirements specified by F&PS. Stratification based on the scene type, surface type, solar zenith angle, and the properties of cloud and aerosol is also needed to characterize the retrieval uncertainties and identify the potential cause of any systematic errors. Cross-validation with other independent satellite products such as

CERES Surface and Atmospheric Radiation Budget (SARB) and retrievals from GOES Surface and Insolation Project (GSIP) algorithm is necessary for consistency assessment.

Unambiguous detection of algorithm deficiencies relies upon the detailed information derived from the validation of internal parameters. For example, component surface flux values (direct and diffuse) can be used to examine the accuracy of parameterization of cloud and aerosol spectral radiative properties since, given a correct optical depth, unrealistic scattering and absorption properties usually result in more significant error in the diffuse than direct flux. For the indirect path, evaluation of internally retrieved surface albedo will reveal the quality of derived composite TOA clear-sky albedo and aerosol climatology; measurements of cloud and aerosol optical depth can be utilized to assess the performance of the process of relating the TOA reflection to the transmission at surface.

For routine and deep-dive assessments of product quality all inputs and outputs and selected internal products must be saved. In addition to total SW flux, internally produced components of radiation (direct, diffuse, UV and VIS) will be evaluated.

5.5.1.3 Product Validation Tool Development

A software tool written in Fortran90 will be developed to perform the ABI SW RB product validation with well established (fixed number of) in-situ ground and TOA measurements. The tool has two main functions: diagnosis and validation. The functionality of diagnosis includes screening for anomalous values, automatic alerting of problems to operator and flagging data to indicate quality. The validation functionality involves automatic collection of reference data, matching up (co-locate) satellite and reference data at various spatial and temporal scales, calculation and display of basic statistics and reporting validation results at various time and spatial scales. Figure 5-1 displays the flowchart of this software tool.

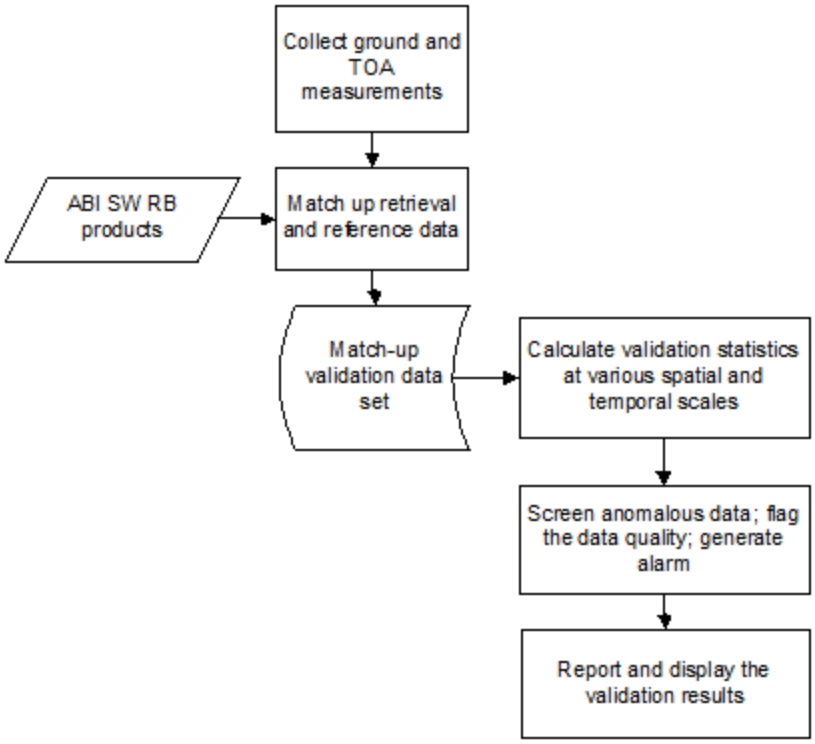

Figure 5-1 Flowchart of validation software package

The tool reports product performance metrics as domain average on instantaneous, hourly, daily and monthly time scales. The metrics include Bias, Standard Deviation, Root-Mean-Square error, Minimum/Maximum, Probability Density Function etc. Stratification according to scene type (clear/cloudy), surface type, angles, diurnal cycles will also be reported. The tool will report output diagnostics including percent completeness; surface site difference time series; number, location and magnitude of failed match between lookup table and observation; and quality flags etc. All inputs and outputs and selected internal products in "match" files will be saved for routine and in-depth assessments of product quality. For long-term validation (at least) monthly means of satellite products and reference data will also be saved.

The design of the validation tool will depend on the available reference data, but in general software written for this validation need to be flexible to incorporate any new additional sources of measurement and make the match-up at any arbitrary temporal and spatial scales. Regarding the current available reference data and retrieval algorithm, certain limitations are associated with the product validation:

- Validation is expected to be difficult over ocean due to lack of extensive, permanent good-quality surface observations.
- Spatial and temporal averaging need to be applied to reduce differences due to spatial and temporal scales represented by satellite and ground, thus a strict validation of instantaneous product is not possible.

- Using climatology for "quick" QC might confuse extreme events with bad data.
- Ground data are often not available in real time. Thus, the validation might not be in real time, and all relevant satellite retrievals must be saved until the validation can be performed.
- Retrievals under certain environmental conditions needs extra attention due to the algorithm limitations, e.g., over snow (cloud identification, AOD estimate); high loading of absorbing aerosol (aerosol AOD will be off); coastal region (highly inhomogeneous surface); and twilight.

Validation (reference) data availability varies with source. Most are likely to be accessible only after an extended time following the observations. The NOAA ESRL/GMD data, however, can be, or are, available within a few days, usually two or less.

The validation tool described above is the tool that will be made available for operational use. For deep-dive, detailed investigation at STAR the same tool will be applied with additional capability for expanded validation with short-term extensive measurements (field campaigns) and with other periodically available data (ships of opportunity), for inter-comparison with other satellite products and model simulations, for evaluation of internal products (direct, diffuse, etc.) and correlative data, for added quality control of in-situ data if needed, for detailed regional and seasonal evaluation to identify causes of any systematic errors, for establishment of stable references (in-situ measurements, RT modeling) and analysis of time series to detect 'drift' (from instrument, calibration, etc.), and for planning and execution of corrective actions to eliminate uncovered problems.

Additional tools include tools for visualization of fields, time series of data and statistics, scatter plots via IDL and/or GrADS, and software for interactive validation data/plot access/generation, and for extraction of satellite time series over ground truth and for matching-up ground observations to overpass times at various time scales.

The CERES FLASHFlux products (Stackhouse et al. 2009) could also be used to help flag RSR and possibly DSR changes in product quality. The FLASHFlux data sets are produced within a week of observation providing a quick-look at changes and variability of fluxes. FLASHFlux currently runs using both Aqua and Terra and is planned for NPP and possibly JPSS (P. Stackhouse, personal communication).

5.5.2 Post-Launch Phase Activities

5.5.2.1 Product Assessment

During the post-launch period validation methodologies and tools developed and tested during the pre-launch period will be applied to actual ABI SW RB retrievals. During the post-launch period, the validation process will be set up for automatically implementation. Validation results will be prepared for distribution in graphical and numerical/descriptive format.

Concurrent VIIRS and CERES on NPOESS platforms and ABI data will be collected. The ABI algorithm will be run with all three data types, and the results will be compared with each other and with ground data. Running the algorithm with VIIRS (similar to MODIS) and CERES data will help in relating the pre-launch validation to that in the post-launch phase relatively quickly without the need for waiting for the collection of long-term data.

5.5.2.1.1 Early Orbit Period

During the period immediately following Early Orbit Checkout intensive QA of the ABI SW RB products will be carried out. Initial validation is expected to result in incremental improvement of product quality through the refinement of algorithm. We will aim at all major product quality issued within 6 months of Early Orbit Checkout and carry out 12 months of comprehensive validation activities to achieve statistically representative validation results by the end of Early Orbit Period.

5.5.2.1.2 Long term operations

During the long-term operations period continuous, automatic validation will provide the near real-time monitoring of retrieval performance. Time series of validation results will be analyzed to detect any trend in the product due to algorithm or instrument issues.

All NOAA ESRL/GMD observations are ongoing and are expected to continue indefinitely into the post launch period. This depends, of course, on the continued funding of those activities by current (GMD base and CPO) or other sources until the anticipated eventual transition into the SEBN funding. The personnel connected with these observations stand ready and willing to participating in the pre and post launch applications of the surface based data to insure continued comprehensive support to the GOES-R program.

5.5.2.1.3 Algorithm Refinements

The validation results will be used to identify algorithm shortfalls. Refined algorithm will be developed and test using accumulated reference and ABI data. Refinements will be sent to the GOES-R System Prime Contractor for integration.

5.5.3 Correlative Data Sources

5.5.3.1 Ground-based Measurements

The ground-based data provide completely independent observational data to which the comparable satellite-derived values can be validated and otherwise evaluated. These observations are available from multiple NOAA operated sites (up to 13 within the full-disk view, 9 CONUS) throughout the algorithm development, prelaunch, and post launch periods.

Throughout the algorithm development phase ground-based data from the NOAA SURFRAD in the CONUS and other ESRL/GMD sites outside CONUS but within the full-disk view have been available for testing and evaluation of algorithms. These data include continuous, one- to three-minute (now all one-minute), surface broadband irradiances, upward and downward solar and thermal IR, as well as spectral aerosol optical depth. These data have been used previously to validate some of the proxy data from other satellite programs that are being used in the GOES-R algorithm development.

The GMD data can be, or are, available within a few days, usually two or less. The GMD radiation project managers should be contacted to ensure the smooth and timely continued access to all available data. Special arrangements can be made to expedite data availability for near real time activities.

The primary source of NOAA ground-based surface radiation budget data over the CONUS is the SURFRAD project. This program has been in operation since 1995 and currently consists of 7 sites that are located in different climatic regions of the CONUS, see http://www.srrb.noaa.gov/surfrad/index.html. SURFRAD constitutes the only national network dedicated to that purpose and is operated for both research and routine applications. Reviewed and edited data are currently available within couple of days of acquisition through direct access on the Internet. Pilot projects have been carried out to demonstrate the feasibility of near-real-time data access, and will be considered for all future enhancements and upgrades to network capabilities. An additional source of surface radiation data is from the GMD Global Baseline and BSRN sites, most of which are located on the outer boundaries of the full-disk view but consequently provide opportunity for algorithm testing and evaluation for those limiting cases. For a map of those sites see http://www.esrl.noaa.gov/gmd/grad/field.html. Preliminary data are currently available from these additional GMD sites within 24 hours through special arrangement, with reviewed and edited data typically available within about two weeks. Like SURFRAD, these data are potentially available near real time (except South Pole which would not be utilized by GOES-R) and expectations are that future evolution of the network will include enhanced temporal access.

All observations from the above GMD programs are calibrated relative to the current international calibration reference standards, the World Radiation Reference (WWR) scale for solar wavelengths (0.28 to ~3.0 μm), and the interim WMO Pyrgeometer Infrared Reference (iWPIR) for the thermal infrared band (3.0 to 50 μm). These references are traceable to SI units through the temperature, voltage, and amperage standards utilized in the most fundamental calibration modes. Transfer standards between the World Radiation Center in Davos, which provides both the WRR and iWPIR, are maintained at the GMD laboratories and participate in routine intercomparisons required for the propagation to the highest possible accuracy research applications. These calibration standards have traceable connections to the current satellite measurements of the extraterrestrial solar irradiance. Surface and satellite infrared observations are connected through fundamental black-body emission physics utilized in the core calibrations of each.

Additional ancillary observations available from the GMD sites include spectral aerosol optical depth, which is of particular importance to matching satellite clear sky and direct solar beam irradiance estimates to ground-based data.

There are plans to combine and expand the SURFRAD and the other GMD radiation network sites. This is currently expected to begin in 2011 and be carried to completion, retaining the current sites and adding 10 more (7-8 in CONUS), by 2017. There would not be breaks or disruption in the current data flow or availability, although a parallel processing and dissemination will be developed that would eventually become the primary access to all data from the new network. The new network is tentatively slated to be called the NOAA Surface Energy Budget Network (SEBN) and would include numerous other measured parameters of the complete surface energy budget parameters.

5.5.3.2 Satellite Derived Products

The full-disk GOES Surface and Insolation Product (GSIP-fd) is currently produces surface and TOA SW fluxes operationally. Although, due to the lack of calibration and the availability of only a single SW channel from the current GOES, the quality of this product is expected to be inferior to the future ABI product the GSIP-fd fluxes can be used for gross quality checks of ABI retrievals performed from the MODIS proxy data.

The NASA/CERES project generates state-of-the art estimates of TOA and surface fluxes. The CERES product includes a suite of retrievals from algorithms of varying complexity. These data are used for both development and validation of the ABI SW RB algorithm, both at the surface and at TOA. During algorithm development TOA broadband albedos are used as input to the indirect path. This way uncertainties resulting from the narrow-to-broadband conversion are eliminated. When the ABI algorithm is driven by MODIS proxy data the CERES TOA albedos are used in the validation of RSR estimated by the ABI algorithm.

Geostationary Earth Radiation Budget (GERB) data can also be used to validate RSR retrieved by the ABI algorithm.

In post-launch phase, measurements of and products generated from the CERES instrument on the NPOESS satellites will be utilized for validation of TOA and surface fluxes.

6 ASSUMPTIONS AND LIMITATIONS

6.1 Performance

The following assumptions have been made in developing and estimating the performance of the algorithm.

1. Surface is Lambertian and its reflectance varies slowly in time.
2. Calibrated reflectances in ABI SW channel are ready.

3. High quality static ancillary data are available at the grid level.
4. The processing systems allows for ingest of previous clear reflectance for creation of the composite clear field, and clear composite reflectance is consistent with aerosol climatology.
5. NWP data of comparable or superior quality to the current 6 hourly GFS forecasts are available. (Use longer range GFS forecasts or switch to another NWP source – ECMWF)

Limitations that could affect the retrieval performance are:

1. Quality of the SW fluxes will critically depend on the quality of ABI cloud, aerosol and surface albedo products.
2. Unknown spectral shifts in some channels will cause biases in the clear-sky RTM calculations that may impact the performance of the NTB.
3. Errors in navigation from image to image will affect the quality of the composite clear reflectance.
4. RT model is 2-D; 3-D effects are not considered.
5. Retrievals over snow and ice (cloud identification, aerosol retrieval); high loading of absorbing aerosol (aerosol optical depth will be off); coastal region (highly inhomogeneous surface); and twilight are inherently more difficult.
6. No retrievals are attempted when the required sensor and ancillary inputs are missing.

Timely availability of ABI level 2 products used as inputs to the direct path is critical. In case one of the required inputs is not available the algorithm switches to the indirect path. The indirect path needs ABI narrowband reflectances in a number of narrowband channels to derive a broadband TOA albedo. When some of the channels are missing, the currently implemented NTB conversion will not be appropriate since that is based on all (five for the MODIS proxy data) channels. The NTB conversion could be performed from a reduced set of channels; however, the broadband albedo (and DSR and RSR) will likely be degraded. NTB with reduced set of channels is not yet implemented in the algorithm, but work has begun to derive such transformation.

6.2 Assumed Sensor Performance

It is assumed that the ABI sensor will meet its current specifications. However, the SRB will be dependent on the following instrumental characteristics.

- Unknown spectral shifts in some channels will cause biases in the TOA albedo estimation and then impact the RSR and DSR retrievals.
- Errors in navigation from image to image will affect the performance of derived clear-sky composite reflectance.

6.3 Pre-Planned Product Improvements

6.3.1.1 Update NTB conversion

The currently implemented NTB conversion does not account for the local zenith angle and azimuth angle dependence. Work is in progress to refine the NTB conversion scheme. In addition, possible elevation dependence of NTB should be investigated and incorporated in the update.

6.3.1.2 Improve the retrieval over snow/ice surface

The current implementation of the indirect path performs poorly over snow/ice surface, especially at the onset of snow. The dominant reason is that at the onset of snow the scene is cloudy and the clear-sky composite reflectance cannot be updated due to the lack of a clear scene (it is cloudy when snows). In addition, optical depth retrieval over a bright surface as snow is proven to be difficult and subject to large errors. Also blending snow-free pixels with snow pixels to a single clear-sky scene type might be an error source for the partially snow covered grids.

Given high quality snow mask generated from ABI, snow surface albedo retrieval might be improved. For example, a dedicated reflectance input for the clear snow pixelscan be generated. This way, clear snow is separated from clear-sky to be a new scene type. (The original clear-sky composite method is still applied to the snow-free clear scene.)

6.3.1.3 Update LUT

The current LUT uses cloud models that are different from the ones used by the ABI Cloud Team. There is a possibility to update the LUT to be consistent with the ABI cloud retrievals. In addition, a common RTM is proposed to be used by all ABI algorithm development groups to increase the consistency among various ABI products. If such common RTM has the capability to calculate broadband SW fluxes, the LUT in the ABI SRB algorithm must be re-calculated.

7 REFERENCES

Barkstrom, B. R. (1984), The Earth Radiation Budget Experiment (ERBE), *Bull. Am. Meteorol. Soc.*, *65*(11), 1170-1185.

Berk, A., L. S. Bernstein, and C. D. Robertson, 1983: A moderate resolution model for LOWTRAN 7, Philips Laboratory, Report AFGL-TR-83-0187, Hanscom Air Force Base, Massachusetts.

Bourlès, B., Lumpkin, R., Mcphaden, M.J., Hernandez., F., Nobre, P., Campos, E., Yu, L., Planton, S., Busalacchi, A., Moura, A.D., Servain, J., And Trotte, J., 2008, The Pirata Program: History, accomplishments, and future directions. *Bulletin of the American Meteorological Society*, 89, pp. 1111-1124.

Briegleb, B. P., P. Minnis, V. Ramanathan and E. Harrison, 1986: Comparison of regional clear-sky albedos inferred from satellite observations and model calculations. *J. Climate Appl. Meteor.*, **25**, 214-226.

Ceballos, J. C., M. J. Bottino, and J. M. de Souza (2004), A simplified physical model for assessing solar radiation over Brazil using GOES 8 visible imagery, *J. Geophys. Res.*, *109*(D2), -, Artn D02211 Doi 10.1029/2003jd003531.

Chandrasekhar, S., 1960: *Radiative Transfer,* New York, Dover, 393 p.

Charlock, T. P., and T. L. Alberta, 1996: The CERES/ARM/GEWEX Experiment (CAGEX) for the retrieval of radiative fluxes with satellite data. *Bull. Amer. Meteor. Soc*., 77, 2673-2683.

Chedin, A., N. A. Scott, C. Wahiche, and P. Moulinier, 1985: The improved initialization inversion method: a high resolution physical method for temperature retrievals from satellites of the TIROS-N series. *J .Clim. Appl. Meteorol.* **24,** 128–143.

Chin, M., P. Ginoux, S. Kinne, B. N. Holben, B. N. Duncan, R. V. Martin, J. A. Logan, A. Higurashi, and T. Nakajima, 2002: Tropospheric aerosol optical thickness fromt he GOCART model and comparisons with satellite and sunphotometer measurements, *J. Atmos. Sci.* 59, 461-483.

Cox, S. J., P. W. Stackhouse Jr., S. K. Gupta, J. C. Mikovitz, T. Zhang, L. M. Hinkelman, M. Wild, and A. Ohmura, (2006), The NASA/GEWEX surface radiation budget project: Overview and analysis. Preprints, 12th Conf. on Atmospheric Radiation, Madison, WI, Amer. Meteor. Soc., 10.1. [Available online at http://ams.confex.com/ams/pdfpapers/112990.pdf.]

Darnell, W. L., Staylor, W. F., Gupta, S. K., and Denn, F. M.: Estimation of surface insolation using Sun-synchronous satellite data, J. Climate, 1, 820–835, 1988.

Dedieu, G., P. Y. Deschamps, and Y. H. Kerr (1987), Satellite Estimation of Solar Irradiance at the Surface of the Earth and of Surface Albedo Using a Physical Model Applied to Meteosat Data, *Journal of Climate and Applied Meteorology*, *26*(1), 79-87.

Diak, G. R., and C. Gautier, Improvements to a simple physical model for estimating insolation from GOES data (1983), *J. Clim. Appl. Meteorol.*, 22, 505-508.

Dubayah, R., and S. Loechel (1997), Modeling topographic solar radiation using GOES data, *Journal of Applied Meteorology*, *36*(2), 141-154.

Dubovik, O., B. N. Holben, T. F. Eck, A. Smirnov, Y. J. Kaufman, M. D. King, D. Tanre, and I. Slutsker (2002), Variability of absorption and optical properties of key aerosol types observed in worldwide locations, *J.Atm.Sci*., 59, 590-608.

Frouin, R., and B. Chertock (1992), A Technique for Global Monitoring of Net Solar Irradiance at the Ocean Surface .1. Model, *Journal of Applied Meteorology*, *31*(9), 1056-1066.

Fu, Q., and K.-N. Liou, (1993), Parameterization of the radiative properties of cirrus clouds. *J. Atmos. Sci.*, 50, 2008-2025.

Fu, Q. (1996), An accurate parameterization of the solar radiative properties of cirrus clouds for climate models, *J. Clim*. Vol 9, 2058-2082.

Gautier, C., Diak, G.R., Masse, S. A simple physical model to estimate incident solar radiation at the surface from GOES satellite data. *J. Appl. Meteor.* 19, 1007-1012, 1980.

Gillespie, A., S. Rokugawa, T. Matsunaga, J. S. Cothern, S. Hook and A. B. Kahle, 1998: A temperature and emissivity separation algorithm for Advanced Spaceborne Thermal Emission and Reflection Radiometer (ASTER) images, *IEEE Trans. Geosci. Remote Sens.*, 36, 1113-1126.

Gupta, S. K., P. W. Stackhouse Jr., S. J. Cox, J. C. Mikovitz, and T. Zhang (2006), Surface radiation budget project completes 22-year data set, *GEWEX News*, 16, 12 – 13.

Gu, J. J., and E. A. Smith (1997), High-resolution estimates of total solar and PAR surface fluxes over large-scale BOREAS study area from GOES measurements, *J. Geophys. Res.*, *102*(D24), 29685-29705.

Gutman, G. and A. Ignatov (1998), The derivation of the green vegetation fraction from NOAA/AVHRR data for use in numerical weather prediction models. *International J. Rem. Sens.*, **19(8)**, 1533-1543.

Harries, J.E., J.E. Russell, J.A. Hanafin, H. Brindley, J. Futyan, J. Rufus, S. Kellock, G. Matthews, R. Wrigley, A. Last, J. Mueller, R. Mossavati, J. Ashmall, E. Sawyer, D. Parker, M. Caldwell, P.M. Allan, A. Smith, M.J. Bates, B. Coan, B.C. Stewart, D.R. Lepine, L.A. Cornwall, D.R. Corney, M.J. Ricketts, D. Drummond, D. Smart, R. Cutler, S. Dewitte, N. Clerbaux, L. Gonzalez, A. Ipe, C. Bertrand, A. Joukoff, D. Crommelynck, N. Nelms, D.T. Llewellyn-Jones, G. Butcher, G.L. Smith, Z.P. Szewczyk, P.E. Mlynczak, A. Slingo, R.P. Allan, and M.A. Ringer, 2005: The Geostationary Earth Radiation Budget Project. *Bull. Amer. Meteor. Soc.*, **86**, 945–960.

Hinkelman, L. M., P. W. Stackhouse, B. A. Wielicki, T. P. Zhang, and S. R. Wilson (2009), Surface insolation trends from satellite and ground measurements: Comparisons and challenges, *J. Geophys. Res.*, *114*, D00d20 10.1029/2008jd011004.

Hu, Y. X, and K. Stamnes, 1993: An Accurate Parameterization of the Radiative Properties of Water Clouds Suitable for Use in Climate Models, *J. Clim*: Vol. 6, No. 4, pp. 728-742.

Kandel, R. S., J. L. Monge, M. Viollier, L. A. Pakhomov, V. I. Adasko, R. G. Reitenbach, E. Raschke, and R. Stuhlmann (1993), The Scarab Project - Earth Radiation

Budget Observations from the Meteor Satellites, *Global Change and Space Observations*, *14*(1), 47-54.

Kato, S., and N. G. Loeb, 2005: Top-of-atmosphere shortwave broadband observed radiance and estimated irradiance over polar regions from Clouds and the Earth's Radiant Energy System (CERES) instruments on Terra, *J. Geophys. Res*., 110, D7, D07202, doi:10.1029/2004JD005308.

Kato, S., G.L. Smith, and H.W. Barker, 2001: Gamma-Weighted Discrete Ordinate Two-Stream Approximation for Computation of Domain-Averaged Solar Irradiance. *J. Atmos. Sci*., 58, 3797–3803

Laszlo, I., H. Jacobowitz, and A. Gruber, 1988: The relative merits of narrowband channels for estimating broadband albedos. *J. Atmos. Oceanic. Technol*., 5, 757 – 773.

Laszlo, I, Pinker, R.T., 2002: Shortwave radiation budget of the Earth: Absorption and cloud radiative effects, *Időjárás*, (Quarterly Journal of the Hungarian Meteorological Service), 106, 189-205.

Liu, H., R. T. Pinker, and B. N. Holben, 2005: A global view of aerosols from merged transport models, satellite, and ground observations, *J. Geophys. Res*., 110, D10S15, doi:10.1029/2004JD004695.

Loeb, N. G., N. M. Smith, S. Kato, W. F. Miller, S. K. Gupta, P. Minnid, and B. A.Wielicki, 2003: Angular distribution models for top-of-atmosphere radiative flux estimation from the Clouds and the Earth's Radiant Energy System instrument on the Tropical Rainfall Measuring Mission Satellite. Part I: Methodology. *J. Appl. Meteor*. 42: 240-265.

Minnis, P., D. P. Garber, D. F. Young, R. F. Arduini and Y. Takano, 1998: Parameterizations of reflectance and effective emittance for satellite remote sensing of cloud properties. *J. Atmos. Sci.*,**55**, 3313–3339.

Minnis, P., P. W. Heck, D. F. Young, C. W. Fairall, and J. B. Snider, 1992: Stratocumulus cloud properties derived from simultaneous satellite and island-based instrumentation during FIRE, *J. Appl. Meteor.*, vol. 31, pp. 317–339.

Morel, M., R. Jegou, C. Readings, and N. Tabarie (1993), Envisats Earth Radiation-Budget Instrument - Scarab, *Esa Bulletin-European Space Agency*(76), 53-57.

Moser, W., and E. Raschke (1984), Incident Solar-Radiation over Europe Estimated from Meteosat Data, *Journal of Climate and Applied Meteorology*, *23*(1), 166-170.

Nunez, M., (1993), The development of a satellite-based insolation model for the tropical western Pacific Ocean, International Journal of Climatology 13, 607–627.

Pinker, R. T., R. Frouin, and Z. Li (1995), A Review of Satellite Methods to Derive Surface Shortwave Irradiance, *Remote Sensing of Environment*, *51*(1), 108-124.

Pinker, R.T. and I. Laszlo, 1992: Modeling surface solar irradiance for satellite applications on a global scale. *J. Appl. Meteor.* 31, 194– 211.

Pinker, R.T., Laszlo, I., Tarpley, J.D. Mitchell, K. Geostationary satellite products for surface energy balance models, 2002: *Adv. Space Res*. 30, 2427-2432.

Pinker, R.T., Tarpley, J.D., Laszlo, I., et al., 2003: Surface radiation budgets in support of the GEWEX Continental-Scale International Project (GCIP) and the GEWEX Americas Prediction Project (GAPP), including the North American Land Data Assimilation System (NLDAS) project, *J. Geophys. Res.* 108(D22), 8844, doi:10.1029/2002JD003301.

Rossow, W. B., and Y. C. Zhang (1995), Calculation of Surface and Top of Atmosphere Radiative Fluxes from Physical Quantities Based on Isccp Data Sets .2. Validation and First Results, *J. Geophys. Res., 100*(D1), 1167-1197.

Rossow, W. B., and R. A. Schiffer (1999), Advances in understanding clouds from ISCCP, Bull. Am. Meteorol. Soc., 80, 2261– 2287.

Russell J. E., 2006: Quality summary for GERB Edition-1 L2 ARG, *Reference document*, Imperial College.

Rutan, D., F. Rose, M. Roman, N. Manalo-Smith, C. Schaaf, and T. Charlock (2009), Development and assessment of broadband surface albedo from Clouds and the Earth's Radiant Energy System Clouds and Radiation Swath data product, *J. Geophys. Res., 114*, Artn D08125 Doi 10.1029/2008jd010669.

Schiffer, R.A., Rossow, W.B. The International Satellite Cloud Climatology Project (ISCCP): The first project of the World Climate Research Programme. *Bull. Amer. Meteor. Soc.* 64, 779-984, 1983.

Schmetz, J. (1989) Towards a surface radiation climatology. Retrieval of downward irradiance from satellites. *Atmos. Res.*, **23,** 287–321.

Stackhouse, P. W., S. K. Gupta, S. J. Cox, J. C. Mikovitz, T. Zhang, and M. Chiacchio (2004), 12-year surface radiation budget data set, *GEWEX News*, 14, 10– 12.

Stackhouse, P. W., S. Kato, D. P. Kratz, S. K. Gupta, A. C. Edwards, A. C. Wilber, J. C. Mikovitz, J. Hoell, "New results from FLASHFlux: A case study of the observed radiative anomalies in the Arctic for 2007 and 2008 summer seasons." 16th Conference on Satellite Meteorology and Oceanography, Phoenix, Arizona, January, 2009.

Stamnes, K., S.-C. Tsay, W. Wiscombe and K. Jayaweera, (1988), Numerically stable algorithm for discrete-ordinate-method radiative transfer in multiple scattering and emitting layered media. *Appl. Opt.* 27, 2502-2509.

Stuhlmann, R., M. Rieland, and E. Raschke (1990), An Improvement of the Igmk Model to Derive Total and Diffuse Solar-Radiation at the Surface from Satellite Data, *Journal of Applied Meteorology, 29*(7), 586-603.

Tarpley, J. D. Estimating incident solar radiation at the surface from geostationary satellite data. *J. Appl. Meteor.* 18, 1172-1181, 1979.

Weymouth, G., and J. Le Marshall (1999), An operational system to estimate global solar exposure over the Australian region from satellite observations - I. Method and the initial climatology, *Australian Meteorological Magazine*, *48*(3), 181-195.

Whitlock, C. H., T. P. Charlock, W. F. Staylor, R. T. Pinker, I. Laszlo, A. Ohmura, H. Gilgen, T. Konzelman, R. C. Dipasquale, C. D. Moats, S. R. Lecroy, and N. A. Ritchey (1995), First Global Wcrp Shortwave Surface Radiation Budget Dataset, *Bull. Am. Meteorol. Soc.*, *76*(6), 905-922.

Wielicki, B. A., B. R. Barkstrom, E. F. Harrison, R. B. Lee, G. L. Smith, and J. E. Cooper (1996), Clouds and the earth's radiant energy system (CERES): An earth observing system experiment, *Bull. Am. Meteorol. Soc.*, *77*(5), 853-868.

Zhang, Y. C., W. B. Rossow, A. A. Lacis, V. Oinas, and M. I. Mishchenko (2004), Calculation of radiative fluxes from the surface to top of atmosphere based on ISCCP and other global data sets: Refinements of the radiative transfer model and the input data, *J. Geophys. Res.*, *109*(D19), -, Artn D19105 Doi 10.1029/2003jd004457.

APPENDIX

A. Narrow-to-broadband conversion

The conversion of narrowband reflectance to broadband reflectance (NTB) requires the selection of "best" narrowband ABI channels. The method is illustrated here for MODIS. Table A-1 lists the MODIS channel combinations considered.

Table A-1. Combinations of MODIS visible and NIR channels for NTB

Combination	1	2	3	4	5	6
Bands used	Band 1+2	Band 1+2+3	Band 1+2+4	Band 1+2+5	Band 1+2+6	Band 1+2+3+4
Combination	7	8	9	10	11	12
Bands used	Band 1+2+3+5	Band 1+2+3+6	Band 1+2+3+4+5	Band 1+2+3+4+6	Band 1+2+3+5+6	Band 1+2+3+4+5+6

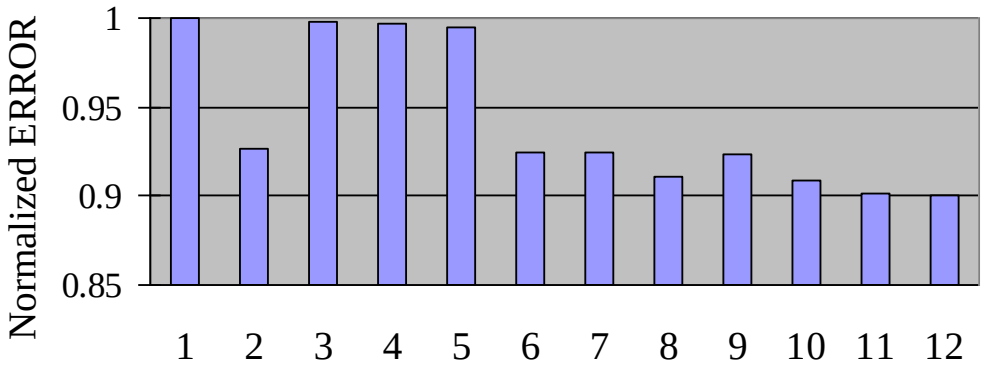

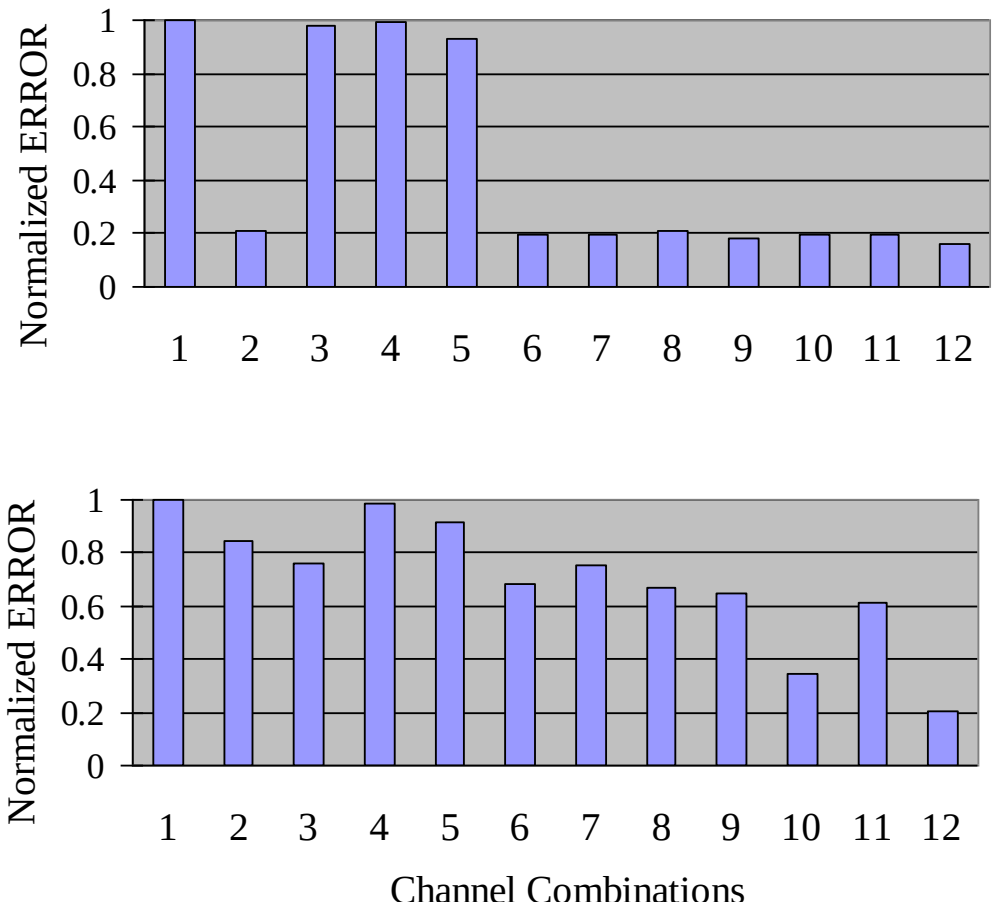

Figure A-1. The Error (Residual Standard Deviation) of the linear regressions between TOA narrowband and broadband reflectance for the channels and the combinations of channels for MODIS over Broadleaf Forest for clear-sky (top), ice cloud (middle), and water cloud (bottom). The values of Error are normalized to those for the basic combination (1).

Figure A-1 shows the histograms of the Error (Eq. 18 in Section 3.4.2.3) for the twelve MODIS-channel combinations for the Broadleaf Forest surface over clear-sky, ice cloud (COD: 1.2-1.8), and water cloud (COD: 5.8-8.2) (COD=cloud optical depth). The Errors are normalized to that of the basic combination of bands 1 + band 2. The other CODs for Broadleaf Forest and other surface classifications (Water; Desert; Snow/Ice) at different CODs have similar performance. For clear-sky and ice, combination (11) has the smallest error but combination (12) has the smallest error for water cloud. Based on this analysis, bands 1, 2, 3, 5, and 6 were initially selected for the NTB transformations for clear-sky and ice clouds, and all 6 bands were selected for water clouds. After testing the above MODIS channel selections, channel 4 (NIR 1.3 μm) was found to be noisy, and therefore was dropped from the regression. Also, it was found that better results were achieved using only the 3 visible channels (bands 1+2+3) instead of channel combinations (11) and

(12). This seems to indicate that there is a need to increase the size of the sample used in simulations to increase the regression stability.

The regression bias analysis shows that the dependence on solar zenith angle is stronger than on other factors. For instance, over a water surface, Figure A-2 gives the distribution of bias for regressed broadband reflectance according to various terms such as relative humidity (left panel) and solar zenith angle (right panel). The bias increases with solar zenith angle due to the relative atmospheric contribution from scattering.

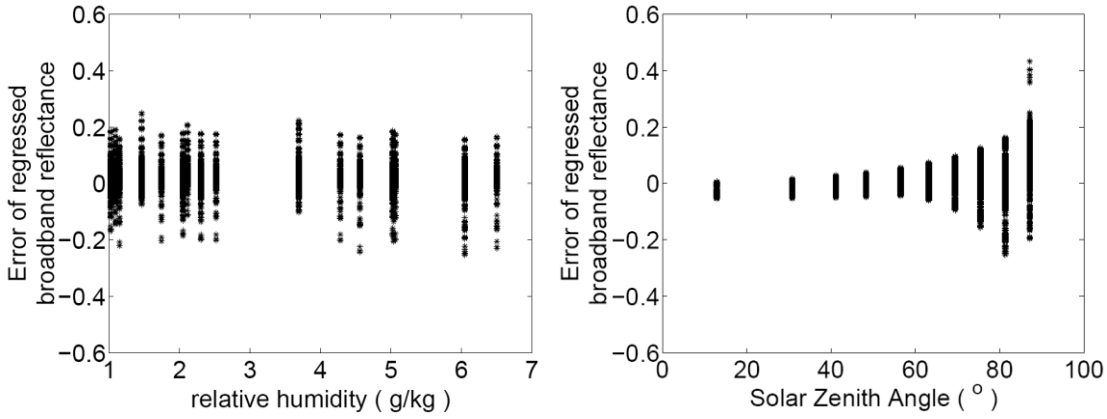

Figure A-2. Distribution of error for regressed broadband albedo according to different predictors. Left panel: relative humidity; Right panel: Solar Zenith Angle (SZA).

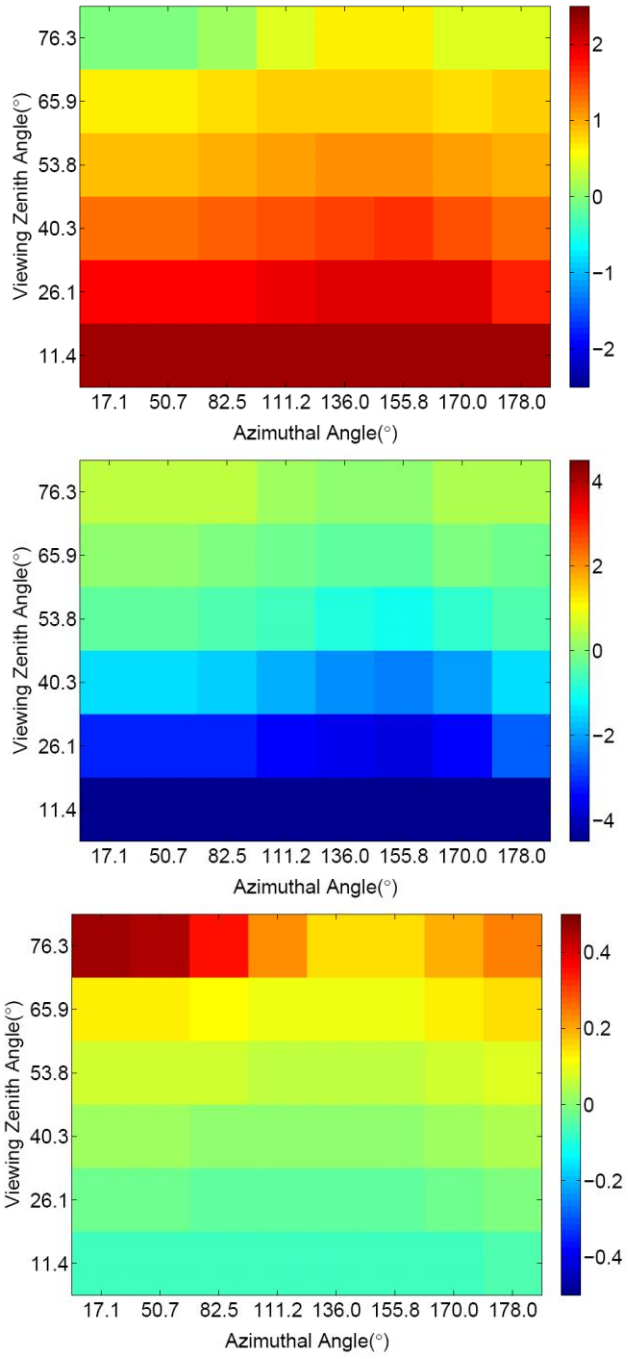

Figure A-3. Distribution patterns of the coefficients of the NTB transformation for Crop/Mosaic surface coverage under clear-sky at SZA of 63.2^{o}. Top: coefficient c_1; Middle: coefficient c_2; Bottom: offset c_0.

Figure A-3 shows the impact of VZA (view zenith) and AZA (azimuth) on the NTB transformation coefficients for GOES-8 for Crop/Mosaic surface under clear sky at SZA of 63.2°. The variability with VZA is apparent. The dependence on AZA is relatively small at low VZA but increases as VZA increases.

In order to select an optimal approach to the development of new angular corrections, both theoretical and empirical options were investigated independently. Until recently, the most commonly used empirical bi-directional correction factors were based on ERBE data. New ADMs based on multi-angle radiance measurements performed by the rotating azimuth plane scanning mode of CERES instruments onboard the Tropical Rainfall Measuring Mission (TRMM) and Terra and Aqua satellites are now available (Loeb et al., 2003). The scene types in the ERBE ADMs are defined by four surface types (ocean, land, desert and snow) and four cloud classes (clear, partly cloudy, mostly cloudy, and overcast). The CERES ADMs have higher scene and angular resolutions than ERBE. The CERES ADMs have around 200 scene types while ERBE ADMs have only twelve. The CERES ADMs have higher angular resolution than ERBE. Figure A-4 shows an example of the difference between CERES and ERBE ADMs for different surface scenes under clear (left panel) and cloudy conditions (right panel). ADMs can also be developed using theoretical simulations with radiative transfer code, but the two approaches are not identical as illustrated in Figure A-5 for the patterns of bi- directional correction factor for desert under clear-sky from MODTRAN 3.7 simulations and CERES observations. The largest difference occurs for higher VZAs. While inaccuracies in the specific surface spectral reflectance used in the simulations may contribute to the differences, they are most likely due to under-sampling of CERES observations at high VZAs. A hybrid approach is applied here to compensate for the under-sampling by combining the CERES ADMs with simulated ones. This requires a method to reconcile the different scene types and angular binning of the CERES and simulated ADMs and a weighting function to combine the two data sources. These processes are described in the following sections.

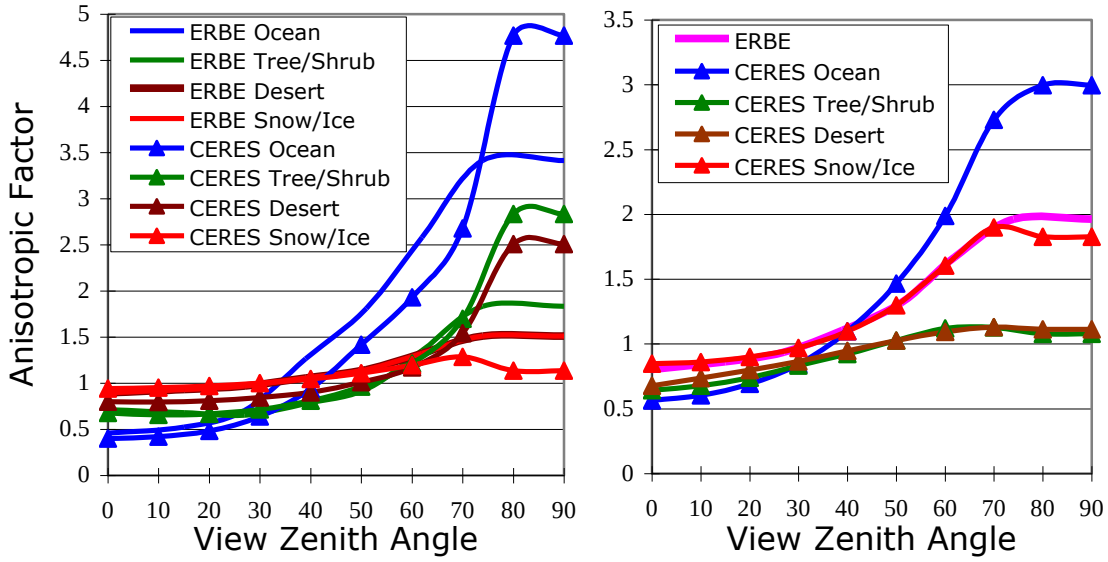

Figure A-4. ERBE and CERES ADMs for different surface types for SZA of 60°-70° and azimuth angle of 150°-170° for clear-sky (left panel) and for cloudy-sky (right panel).

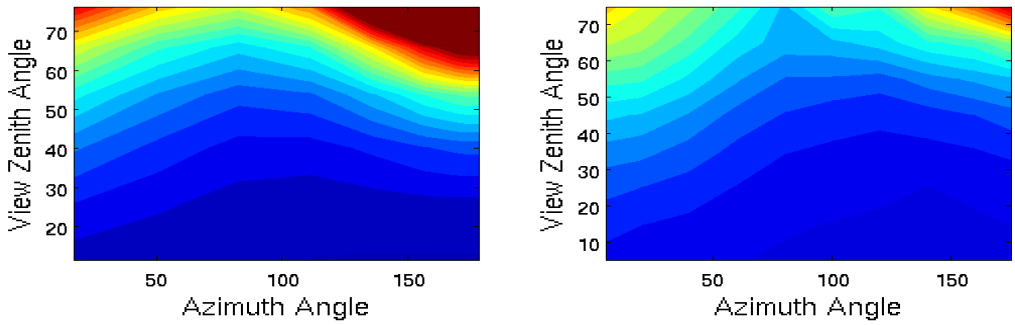

Figure A-5. Anisotropic Factors at SZA 63.2° over desert for Clear Sky. Left: Simulations; Right: CERES observations (Bright Desert)

The distribution of SZAs, VZAs, and AZAs in the MODTRAN 3.7 simulations is different than those in the CERES ADMs. Linear interpolation is used to transfer the CERES angular space into the angular space used in the simulations.

In addition, the CERES-TRMM clear-sky ADM classification by surface types does not fully match the IGBP surface classification. In the simulations, the 12 IGBP surface classifications are used and these include: (1) Water; (2) Needleleaf Forest; (3) Broadleaf Forest; (4) Mixed Forest; (5) Woody Savannas; (6) Savannas; (7) Closed Shrub; (8) Open shrub; (9) Grasslands; (10) Croplands; (11) Bare Ground; (12) Snow and Ice. For clear sky, there are 8 surface types in CERES ADMs, which include Ocean, Desert (bright,

dark), Low-Mod Tree/Shrub, Mod-Hi Tree/Shrub, Permanent Snow (bright, dark), Fresh Snow, and Sea Ice. The classification of Fresh Snow and Sea Ice is somewhat complicated because the scene is divided into different snow or ice coverage. Table A-2 exhibits the comparison of surface types in the simulations and in the CERES ADMs for clear-sky. An effort was made to combine the corresponding CERES ADMs and simulated ADMs based on IGBP scene classifications to generate new synthesized ADMs for 12 IGBP surface types.

Table A-2. Scene classification in CERES ADMs and simulations for clear sky.

CERES surface scenes	IGBP surface scenes in simulations
Ocean	Water
Low-Mod Tree/Shrub	Savannas Grasslands Crops/ Mosaic
Mod-High Tree/Shrub	Needleleaf Forest Broadleaf Forest Mixed Forest Closed Shrubs Woody Savannas
Dark Desert	Open Shrubs
Bright Desert	Barren/Desert
Snow/Ice	Snow/Ice

The cloud classification in CERES ADMs is more complex. The classification is based on Cloud Optical Depth (COD) levels and cloud phase (water cloud, ice cloud) over ocean, low-mod tree/shrub, mod-high tree/shrub, desert, and snow/ice, as shown in Table A-3. Totally, there are 88 datasets in CERES ADMs for cloudy sky which will be utilized with corresponding cloud information. The CERES water cloud ADMs over ocean are illustrated in Figure A-6 as a function of cloud optical depth, local zenith angle, and relative azimuth angle for Solar Zenith Angle (SZA) bin of 53.1-60°.

Table A-3. Cloud classification in CERES ADMs.

Scene	Cloud Optical Depth (COD)	Cloud Phase

Ocean		14 types: 0.01-1.0; 1.0-2.5; 2.5-5.0; 5.0-7.5; 7.5-10.0; 10.0-12.5; 12.5-15.0; 15.0-17.5; 17.5-20.0; 20.0-25.0; 25.0-30.0; 30.0-40.0; 40.0-50.0; COD>50.0	Water Cloud Ice Cloud
Low-Mod Tree/Shrub		6 types 0.01-2.5; 2.5-6.0; 6.0-10.0; 10.0-18.0; 18.0-40.0; COD>40.0	Water Cloud Ice Cloud
Mod-High Tree/Shrub			
Desert	Bright Dark		
Permanent Snow	Bright Dark	2 types: COD>10.0 COD<10.0	None
Fresh Snow	Bright Dark		
Sea Ice	Bright Dark		

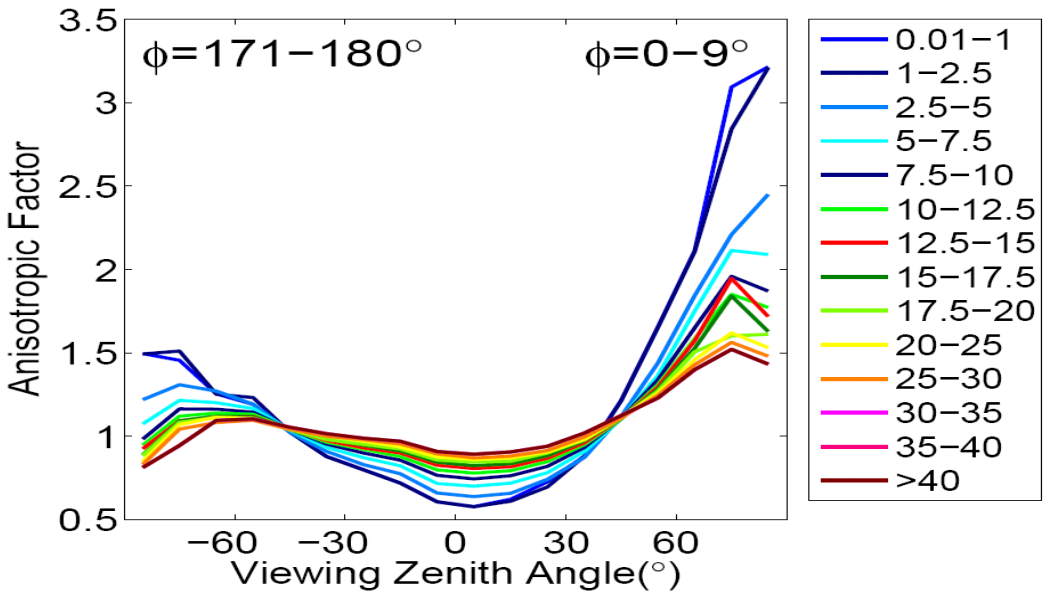

Figure A-6. The CERES bi-directional correction factors for overcast water clouds over ocean as a function of cloud optical depth, local zenith angle, and relative azimuth angle for SZA of 53.1-60.0°.

For clear sky, the synthesized ADMs are generated from a combination of simulated and CERES bi-directional correction factors based on IGBP surface classifications (Table A-2) for each angular bin by weighting as follows:

$$\bar{R}(\theta_0,\theta,\varphi)=\frac{1}{N_{CERES}+N_{SIM}}\left(N_{CERES}\times R_{CERES}(\theta_0,\theta,\varphi)+N_{SIM}\times R_S(\theta_0,\theta,\varphi)\right)$$

Where, $\bar{R}(\theta_0,\theta,\phi)$ are the synthesized ADMs at each angular bin; R_{CERES} are CERES ADMs; R_S are simulated ADMs; N_{CERES} is the sample numbers for each angular bin in the CERES ADMs; N_{SIM} is the case numbers for each angular bin in the simulated ADMs. For example, CERES Low-Mod Tree/Shrub ADMs are grouped from observations of the following three IGBP surface scenes: Savannas, Grassland, and Crops/Mosaic (Loeb et al., 2003), as shown in Table A-2. The difference in the bi-directional correction factors between the combined and CERES ADMs for Savannas is shown in Figure A-7**.** At lower local zenith angles the percentage of differences is mostly within +/- 10% but the differences are much larger at higher local zenith angles.

For cloudy sky, CERES ADMs are used based on CODs and cloud phase (water; ice) for several surface classifications such as ocean, low-mod shrub/tree, mod-high shrub/tree, desert (bright, dark), and snow/ice.

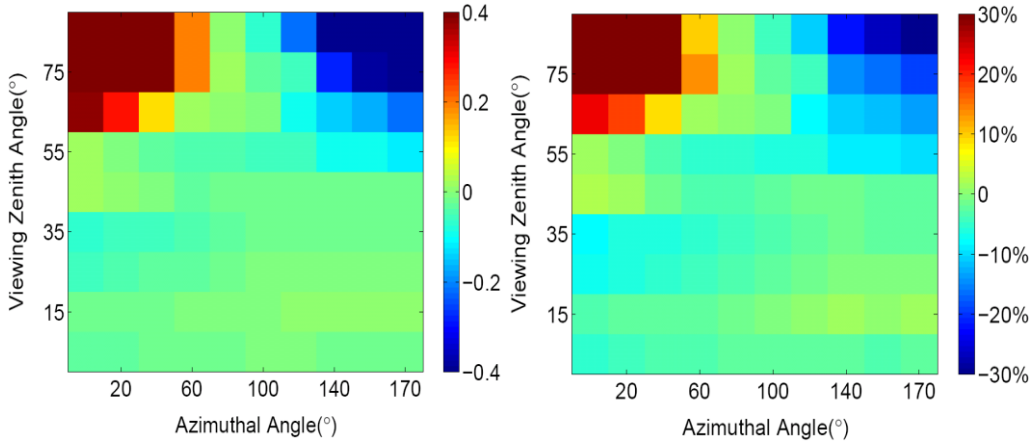

Figure A-7. Distribution patterns of the difference of the bi-directional correction factor between combined ADMs and CERES ADMs for Savannas over clear sky at Solar Zenith Angle of 70-80^o. Left: Difference (Combined ADMs – CERES ADMs). Right: Percentage of Difference (Difference/CERES ADMs)

The NTB coefficients and ADMs have been tested by applying them to SEVIRI and MODIS data and comparing the results to CERES observations. Figure A-8 shows the monthly mean TOA upward SW fluxes from CERES observations (SRBAVG product, 1° resolution) and from SEVIRI fluxes (1/8° resolution) for July 2004, both of which have

consistent distribution patterns. The scatter plots (Figure A-9) compare monthly mean SEVIRI fluxes against CERES observations for both clear sky and all sky. The SEVIRI fluxes slightly overestimate by about 4 Wm^{-2} for clear sky and slightly underestimate by about 3 Wm^{-2} for all sky compared to CERES observations. The standard deviation (SD) of SEVIRI fluxes is about 6 Wm^{-2} and the correlation is 0.98 for both clear and all sky.
Further independent evaluations at daily time scale have been done against surface measurements including 4 BSRN surface observations (DAA, SBO, TAM, and ILO sites, Table A-4) and 10 PIRATA mooring measurements (http://www.pmel.noaa.gov/pirata/) in the tropical Atlantic (Bourlès *et al.* 2008). A comparison of daily averaged all-sky surface downward SW fluxes from UMD/SRB model as driven with SEVIRI observations for July 2004 and observations from the BSRN and PIRATA sites is shown in Figure A-10. Results show a bias of 3.6 Wm^{-2} and SD of 27.4 Wm^{-2} against surface observed SW fluxes for both land and ocean measurements. A small fraction of data (2%) is eliminated from the comparison, where the differences between estimated SEVIRI fluxes and observed flux were larger than three times the standard deviation of the differences.

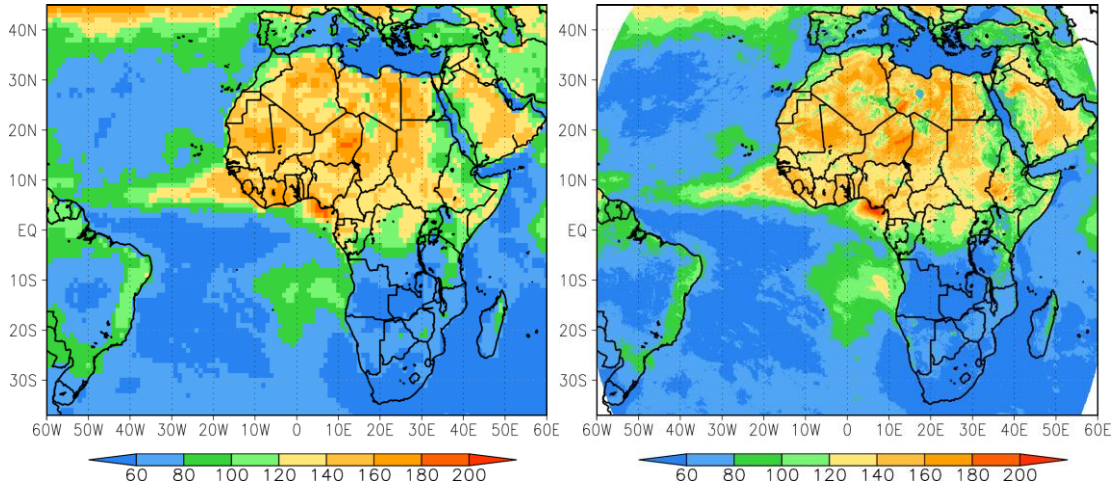

Figure A-8. July 2004 monthly mean TOA SW upward fluxes (W/m2) from CERES (left) and METEOSAT-8/SEVIRI (right).

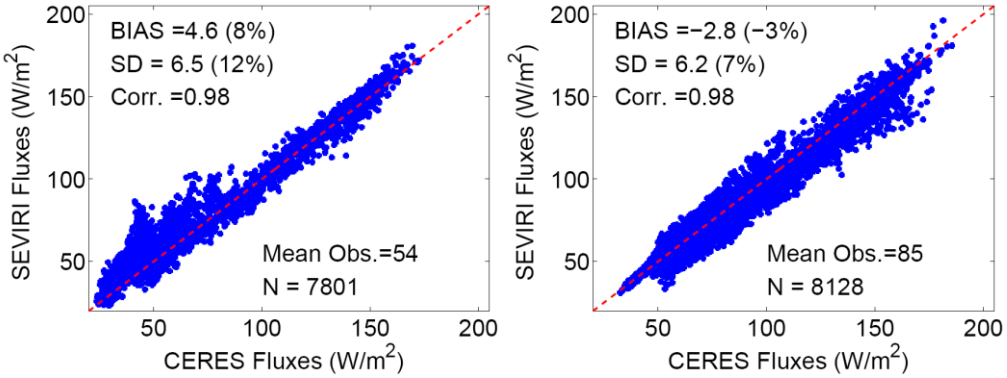

Figure A-9. Evaluation of July 2004 all sky monthly mean TOA upward SW SEVIRI fluxes against CERES observations for clear sky (Left) and all sky (Right).

Table A-4. Locations of four BSRN surface observation stations.

Name	Location	Latitude	Longitude
DAA	De Aar, South Africa	30.67° S	23.99° E
SBO	Sede Boqer, Israel	30.91° N	34.78° E
TAM	Tamanrasset, Algeria	22.78°N	5.51°E
ILO	Ilorin, Nigeria	8.53°N	4.57°E

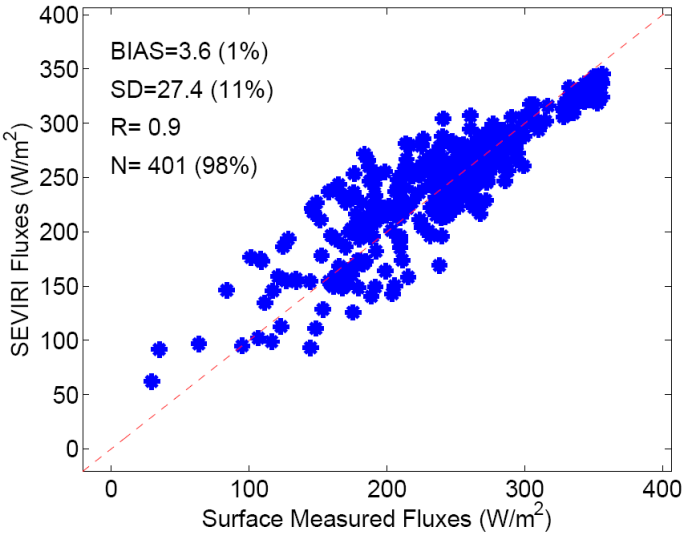

Figure A-10. Evaluation of July 2004 daily mean surface downward SW fluxes estimated from UMD/SRB_SEVIRI against surface observations from 4 BSRN sites and 10 PIRATA moorings (cases eliminated 2%).

To evaluate the NTB coefficients derived for MODIS input data, TOA shortwave fluxes were computed by applying the NTB coefficients and ADMs to 1-km MODIS radiance data for July 2005. The fluxes have been computed for 100 km x 100 km squares centered on the 7 SURFRAD sites in the United States using the UMD/SRB model. These regions were chosen for comparison to CERES data from the CAVE database which contains TOA SW upward fluxes from the CERES footprints whose centroids are within 25 km of the SURFRAD sites.

The evaluation was completed with several different sets of NTB coefficients to determine the optimum number of channels to use, which angular stratification is optimal, and how to treat pixels identified as ice clouds in MODIS but having large cloud

optical depths unrealistic for cirrus clouds. Possibly, the MODIS cloud phase algorithm identifies multi-layer clouds as ice clouds. Test cases included:

1. Using 5 MODIS channels for clear-sky and ice cloud cases and 6 MODIS channels for water cloud cases; stratifying NTB coefficients by SZA and local zenith angles. This resulted in a large overestimation of CERES fluxes.
2. Using 5 MODIS channels for clear-sky and ice cloud cases and 6 MODIS channels for water cloud cases; stratifying NTB coefficients by SZA only. This resulted in underestimation of CERES fluxes by about 15 Wm^{-2}.
3. Using 3 MODIS channels for clear-sky and both ice and water cloud cases and stratifying NTB coefficients by SZA only. This also resulted in underestimation of CERES fluxes by about 15 Wm^{-2}.
4. Using 3 MODIS channels for clear-sky and both ice and water cloud cases; stratifying NTB coefficients by SZA only; using NTB coefficients for altostratus clouds when COD reported by MODIS was >5. This resulted in an overestimation of CERES fluxes by about 11 Wm^{-2}.
5. Using 3 MODIS channels for clear-sky and both ice and water cloud cases; stratifying NTB coefficients by SZA only; using NTB coefficients for water clouds when COD reported by MODIS was > 5. This yielded the best results, with a slight overestimation of CERES fluxes by about 2.6 Wm^{-2}. Results for this case are given in Figure A-11**.**

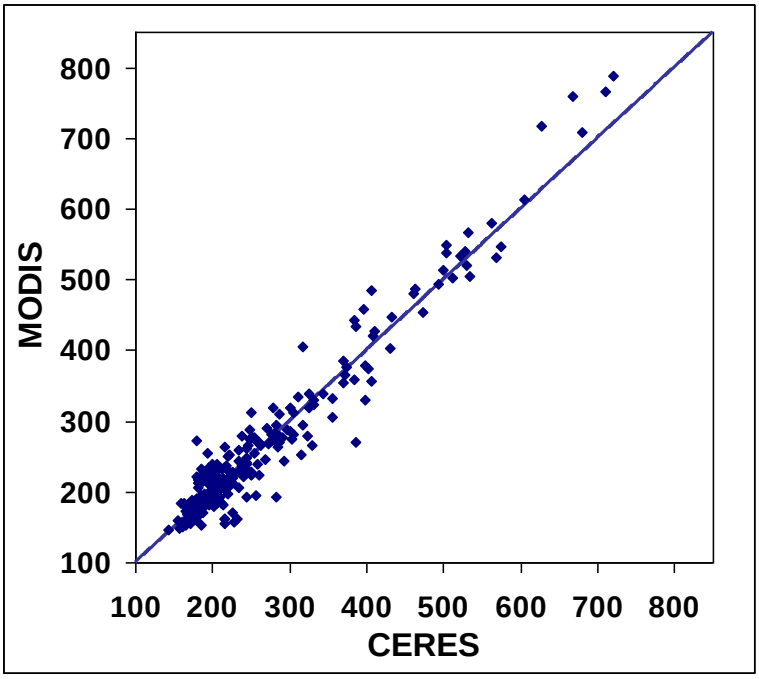

Figure A-11. Evaluation of July 2005 instantaneous TOA upward SW fluxes estimated from MODIS proxy data against CERES data at 7 SURFRAD sites in the US.

The monthly mean SW upward fluxes estimated from SEVIRI observed radiances have been evaluated against CERES TOA products (SRBAVG) for July 2004. Since the maximum value of observations is less than 200 Wm^{-2}, the statistical results (Table A-5) have shown the bias and SD for clear sky and all sky conditions, for land, ocean, and all surface cases.

Compared to ground observations at 4 BSRN sites and 10 PIRATA buoys for July 2004, the daily mean surface SW fluxes derived from SEVIRI data have a bias of 10.4 Wm^{-2} and SD of 28.8 Wm^{-2} when observed fluxes are less than 200 Wm^{-2}, and have a bias of -1.8 Wm^{-2} and SD of 21.3 Wm^{-2} when observed fluxes are larger than 200 Wm^{-2} and less than 500 Wm^{-2}. There are no observations larger than 500 Wm^{-2}.

Table A-5. Evaluations of monthly mean SEVIRI SW upward fluxes against CERES products (SRBAVG) for July 2004.

Statistical Results		BIAS (W/m^2)			SD (W/m^2)		
		F<200	200<F<500	F>500	F<200	200<F<500	F>500
Clear	Land	1.7	Nan	Nan	7.1	Nan	Nan

Sky	Ocean	6.1	Nan	Nan	5.6	Nan	Nan
	All	4.6	Nan	Nan	6.5	Nan	Nan
All Sky	Land	-5.2	Nan	Nan	6.2	Nan	Nan
	Ocean	-1.5	Nan	Nan	5.9	Nan	Nan
	All	-2.8	Nan	Nan	6.2	Nan	Nan

The evaluation of TOA SW upward flux using MODIS proxy data in test case #5 is given in Table A-6.

Table A-6. Evaluation of July 2005 instantaneous TOA upward SW fluxes estimated from MODIS proxy data against CERES data at 7 SURFRAD sites in the US.

BIAS (W/m^2)			SD (W/m^2)		
F<200	200<F<500	F>500	F<200	200<F<500	F>500
9.56	-4.11	22.36	21.70	31.08	38.27

B: Common Ancillary Data Sets

1. LAND_MASK_NASA_1KM

a. Data description

Description: Global 1km land/water used for MODIS collection 5
Filename: lw_geo_2001001_v03m.nc
Origin: Created by SSEC/CIMSS based on NASA MODIS collection 5
Size: 890 MB.
Static/Dynamic: Static

b. Interpolation description

The closest point is used for each satellite pixel:

1) Given ancillary grid of large size than satellite grid
2) In Latitude / Longitude space, use the ancillary data closest to the satellite pixel.

2. MDS_L2_CLD_HGT_5KM_FILE

a. Data description

Description: MODIS L2 cloud height 5km
Filename: MOD06_L2.AYYYYDDD.HHMM.005.yyyydddhhmmss.nc /
MYD06_L2.AYYYYDDD.HHMM.005.yyyydddhhmmss.nc.
Where,
MOD06_L2 / MYD06_L2 – Level 2 Cloud Product from TERRA (MOD) /
AQUA (MYD)
A – Nothing to do here
YYYYDDD – 4 digit year plus 3 digit of Julian day
HHMM – 2 digit of hour and 2 digit of minutes in GMT
005 – Processing system version
Yyyydddhhmmss – processing date/time
Origin: NASA DAAC
Size: 123 MB.
Static/Dynamic: Dynamic

b. Interpolation description

The closest point is used for each satellite pixel:

In Latitude / Longitude space, use the ancillary data closest to the satellite pixel.

3. MDS_L2_CLD_MASK_FILE

a. Data description

Description: MODIS L2 cloud mask 1km
Filename: MOD35_L2.AYYYYDDD.HHMM.005.yyyydddhhmmss.nc /
MYD35_L2.AYYYYDDD.HHMM.005.yyyydddhhmmss.nc.
Where,
MOD35_L2/ MYD35_L2 – Level 2 Cloud Mask from TERRA (MOD) /
AQUA (MYD)
A – Nothing to do here
YYYYDDD – 4 digit year plus 3 digit of Julian day
HHMM – 2 digit of hour and 2 digit of minutes in GMT
005 – Processing system version
yyyydddhhmmss – processing date/time
Origin: NASA DAAC
Size: 45 MB
Static/Dynamic: Dynamic

b. Interpolation description

The closest point is used for each satellite pixel:

In Latitude / Longitude space, use the ancillary data closest to the satellite pixel.

4. MDS_L2_CLD_MICRO_FILE

a. Data description

Description: MODIS L2 cloud micro
Filename: MOD06_L2.AYYYYDDD.HHMM.005.yyyydddhhmmss.nc /
MYD06_L2.AYYYYDDD.HHMM.005.yyyydddhhmmss.nc.
Where,

MOD06_L2/ MYD06_L2 – Level 2 Cloud Product from TERRA (MOD) /
AQUA (MYD)
A – Nothing to do here
YYYYDDD – 4 digit year plus 3 digit of Julian day
HHMM – 2 digit of hour and 2 digit of minutes in GMT
005 – Processing system version
yyyydddhhmmss – processing date/time

Origin: NASA DAAC
Size: 123 MB.
Static/Dynamic: Dynamic

b. Interpolation description

The closest point is used for each satellite pixel:

In Latitude / Longitude space, use the ancillary data closest to the satellite pixel.

5. MDS_L2_CLD_PHASE_5KM

a. Data description

Description: MODIS L2 cloud phase 5km
Filename: MOD06_L2.AYYYYDDD.HHMM.005.yyyydddhhmmss.nc /
MYD06_L2.AYYYYDDD.HHMM.005.yyyydddhhmmss.nc.
Where,
MOD06_L2/ MYD06_L2 – Level 2 Cloud Mask from TERRA (MOD) /
AQUA (MYD)
A – Nothing to do here
YYYYDDD – 4 digit year plus 3 digit of Julian day
HHMM – 2 digit of hour and 2 digit of minutes in GMT
005 – Processing system version
yyyydddhhmmss – processing date/time
Origin: NASA DAAC
Size: 123 MB.
Static/Dynamic: Dynamic

b. *Interpolation description*

The closest point is used for each satellite pixel:

In Latitude / Longitude space, use the ancillary data closest to the satellite pixel.

6. NWP_GFS

a. *Data description*

Description: NCEP GFS model data in grib format – 1 x 1 degree (360x181), 26 levels
Filename: gfs.tHHz.pgrbfhh
Where,
HH – Forecast time in hour: 00, 06, 12, 18
hh – Previous hours used to make forecast: 00, 03, 06, 09
Origin: NCEP
Size: 26MB
Static/Dynamic: Dynamic

b. Interpolation description

There are three interpolations are installed:

NWP forecast interpolation from different forecast time:

Load two NWP grib files which are for two different forecast time and interpolate to the satellite time using linear interpolation with time difference.

Suppose:

T1, T2 are NWP forecast time, T is satellite observation time, and T1 < T < T2. Y is any NWP field. Then field Y at satellite observation time T is:

$$Y(T) = Y(T1) * W(T1) + Y(T2) * W(T2)$$

Where W is weight and

$$W(T1) = 1 – (T-T1) / (T2-T1)$$
$$W(T2) = (T-T1) / (T2-T1)$$

NWP forecast spatial interpolation from NWP forecast grid points. This interpolation generates the NWP forecast for the satellite pixel from the NWP forecast grid dataset.

The closest point is used for each satellite pixel:

1) Given NWP forecast grid of large size than satellite grid
2) In Latitude / Longitude space, use the ancillary data closest to the satellite pixel.

NWP forecast profile vertical interpolation

Interpolate NWP GFS profile from 26 pressure levels to 101 pressure levels

For vertical profile interpolation, linear interpolation with Log pressure is used:

Suppose:

y is temperature or water vapor at 26 levels, and y101 is temperature or water vapor at 101 levels. p is any pressure level between p(i) and p(i-1), with p(i-1) < p <p(i). y(i) and y(i-1) are y at pressure level p(i) and p(i-1). Then y101 at pressure p level is:

$$y101(p) = y(i-1) + \log(p[i] / p[i-1]) * (y[i] - y[i-1]) / \log (p[i] / p[i-1])$$

7. SFC_ALBEDO

a. *Data description*

Description: MODIS White Sky Surface albedo
Filename: AlbMap.WS.c004.v2.0.YYYY.DDD.0.659_x4.nc
AlbMap.WS.c004.v2.0.YYYY.DDD.1.64_x4.nc
Where,
YYYY = 4 digit year
DDD = 3 digit Julian day
Origin:
Size: **2**8 MB x 2
Static/Dynamic: Static

b. ***Interpolation description***

The closest point is used for each satellite pixel:

3) Given ancillary grid of large size than satellite grid
4) In Latitude / Longitude space, use the ancillary data closest to the satellite pixel.

8. SFC_TYPE_AVHRR_1KM

a. ***Data description***

Description: Surface type mask based on AVHRR at 1km resolution
Filename: gl-latlong-1km-landcover.nc
Origin: University of Maryland
Size: 890 MB
Static/Dynamic: Static

b. ***Interpolation description***

The closest point is used for each satellite pixel:

1) Given ancillary grid of large size than satellite grid
2) In Latitude / Longitude space, use the ancillary data closest to the satellite pixel.

9. SFC_ELEV_GLOBE_1KM

a. ***Data description***

Description: Digital surface elevation at 1km resolution.
Filename: GLOBE_1km_digelev.nc
Origin: NGDC
Size: 1843.2 MB
Static/Dynamic: Static

b. ***Interpolation description***

The closest point is used for each satellite pixel:

1) Given ancillary grid of large size than satellite grid
2) In Latitude / Longitude space, use the ancillary data closest to the satellite pixel.

10.SNOW_MASK_IMS_SSMI

a. *Data description*

Description: Snow/Ice mask, IMS – Northern Hemisphere, SSM/I – Southern Hemisphere
4km resolution – the 25 km SSM/I has been oversampled to 4km
Filename: snow_map_4km_YYMMDD.nc
Origin: CIMSS/SSEC
Size: 39 MB.
Static/Dynamic: Dynamic

b. *Interpolation description*

The closest point is used for each satellite pixel:

1) Given ancillary grid of large size than satellite grid
2) In Latitude / Longitude space, use the ancillary data closest to the satellite pixel.